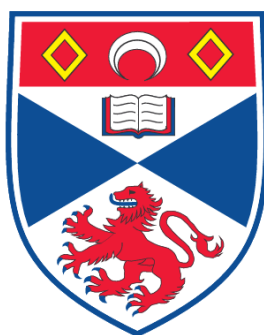


**STRUCTURAL STUDIES OF IONIC LIQUIDS AND
IONOTHERMALLY-PREPARED MATERIALS**

Peter Joseph Byrne

**A Thesis Submitted for the Degree of PhD
at the
University of St. Andrews**



2009

**Full metadata for this item is available in the St Andrews
Digital Research Repository**

at:

<https://research-repository.st-andrews.ac.uk/>

Please use this identifier to cite or link to this item:

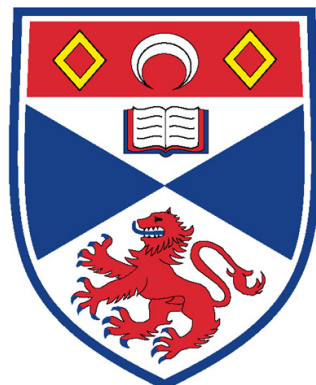
<http://hdl.handle.net/10023/780>

This item is protected by original copyright

Structural studies of ionic liquids and ionothermally-prepared materials.

A thesis submitted in application for the title of Ph.D. by

Peter Joseph Byrne B.Sc



University
of
St Andrews

February 2009

Declaration

I, Peter Joseph Byrne, hereby certify that this thesis, which is approximately 34,000 words in length, has been written by me, that it is the record of work carried out by me and that it has not been submitted in any previous application for a higher degree.

I was admitted as a research student in September 2005 and as a candidate for the degree of Ph.D. in September 2006; the higher study for which this is a record was carried out in the University of St Andrews between 2005 and 2009.

Date

Signature of candidate

I hereby certify that the candidate has fulfilled the conditions of the Resolution and Regulations appropriate for the degree of Ph.D. in the University of St Andrews and that the candidate is qualified to submit this thesis in application for that degree.

Date

Signature of supervisor

In submitting this thesis to the University of St Andrews we understand that we are giving permission for it to be made available for use in accordance with the regulations of the University Library for the time being in force, subject to any copyright vested in the work not being affected thereby. We also understand that the title and the abstract will be published, and that a copy of the work may be made and supplied to any bona fide library or research worker, that my thesis will be

electronically accessible for personal or research use unless exempt by award of an embargo as requested below, and that the library has the right to migrate my thesis into new electronic forms as required to ensure continued access to the thesis. We have obtained any third-party copyright permissions that may be required in order to allow such access and migration, or have requested the appropriate embargo below.

Date

Signature of candidate

Signature of supervisor

Courses Attended

The School of Chemistry at the University of St. Andrews requires that a postgraduate attend a number of taught courses. The courses attended were:

Fundamentals in solid state NMR: Dr. S. Ashbrook

Crystallography: Dr. P. Lightfoot

Hot Topic in Catalysis: Prof. D. Cole-Hamilton and Dr P. Wright

An introduction to Fortran: Dr. T. Van Mourik

Publications

Ionothermal synthesis of two novel metal organophosphonates.

Peter J. Byrne, David S. Wragg, John E. Warren and Russell E. Morris, *Dalton Trans.*, 2009, 795

Structure and NMR assignment in AlPO₄-15: a combined study by diffraction, MAS NMR and first-principles calculations

Peter J. Byrne, John E. Warren, Russell E. Morris and Sharon E. Ashbrook
Solid State Sciences, 2009, *accepted*

Charge density and *in-situ* studies of ionic and ionothermally prepared materials

Peter J. Byrne, David S. Wragg, Russell E. Morris and John E. Warren, *Acta Cryst A.*, **64**, 2008. C536

Acknowledgements

I would like to thank Professor Russell E. Morris and Dr John Warren for their guidance and supervision throughout this Ph.D. Dr Tim Prior, Dr Simon Teat and Dr David Taylor for all their help with my many questions whilst using the Synchrotrons. The Morris group especially Dr. David Wragg and Dr. Paul Wheatley for all their assistance.

Thanks also goes to Professor Alex Slawin for crystallography collected at St. Andrews, Dr Sharon Ashbrook for help with the solid state NMR, Gaétan Giriat for his assistance with the microwave work and to the technical staff at St. Andrews University, Mrs. S. Williamson (CHN analysis), Mrs. M. Smith (NMR) and Mr. R. Blackley (PXRD).

I would also like to thank my friends and family for helping me through the years of study especially my girlfriend Karriz and my parents Martin and Ann.

I would also like thank the EPSRC and the STFC for funding this work.

Abstract

The aim of this thesis was to examine materials using high resolution X-ray diffraction techniques. Initial work involved the synthesis of various metal phosphates to investigate their suitability for charge density work. Many of these were discovered to be of insufficient quality for further study. Much of the phosphate synthesis work performed at the moment utilises an ionic liquid both as a solvent and structure directing agent which dictates the topology of the structure due to its size and charge density. As such the ionic liquid 1-ethyl-3-methylimidazolium hexafluorophosphate used in the synthesis process was examined with high resolution X-ray diffraction as it was possible to produce large pure crystals which could be examined further. A high resolution data set was also collected from the metal organic framework SIMOF-1 which produced a preliminary multipole model however further data collections are required to improve the quality of the model.

A multi-technique investigation involving X-ray diffraction, solid state NMR and first principles calculations was carried out on the aluminophosphate material $\text{AlPO}_4\text{-15}$. A synchrotron X-ray single crystal diffraction study was carried out on the same sample as that used in solid state NMR studies. The model from the single crystal study, together with a model from a literature high resolution study of the same material, were used as starting points for the first-principles calculations of the NMR parameters. This enabled the ^{31}P and ^{27}Al NMR spectra to be unambiguously assigned and all the NMR parameters calculated agreed well with the experimental spectra even without relaxing the X-ray derived structural models. Highlighting that

as long as a good data set has been collected in the first place the atomic positions would not change too drastically.

Other aspects of this thesis involved investigations into other ionothermally prepared systems such as the use of different phosphonate sources to provide functionality to the materials. This work resulted in some interesting findings such as the ionic liquid breaking down and being incorporated into the framework via the metal. Many of the structures produced were of a layered nature however a molecular structure was also synthesised which is unlike the vast majority of hydrothermally prepared phosphonates, which are layered.

The negligible vapour pressure provided by the ionic liquid has enabled synthesis reactions to be investigated with glass vessels on an energy dispersive beam line. This work highlighted how it is possible to study the synthesis process *in-situ* and compare microwave assisted reactions against a conventional heating method, the results indicate that two different types of reactions are occurring resulting in different intermediates which is due to the way the reagents are heated. The microwave assisted reactions also result in larger purer crystals which highlights the importance of the method in materials synthesis.

The use of a specially designed environmental gas cell was used to investigate the adsorption properties of the metal organic framework CPO-27-Co *in-situ*. Using the cell it was possible to locate sulfur dioxide physisorbed and chemisorbed sites within the framework which could be removed by the application of a vacuum and heat.

It was also possible to locate the chemisorbed sites for nitric oxide within the metal organic framework however due to the low scattering factor and disorder from the gas it was not possible to locate the physisorbed sites.

Table of Contents

1 Zeolites and Zeotypes	1
1.1 Introduction	1
1.2 Zeolite synthesis	5
1.3 SDAs in zeolite synthesis	7
1.4 Ionic liquids	11
1.5 Applications	14
1.6 Ionic liquid preparation	15
1.7 Eutectic mixture	16
1.8 The Fluoride method	16
1.9 Applications of Zeolites	18
1.10 Inorganic organic hybrids	20
1.11 Metal Organic Frameworks	20
1.12 Synthesis	21
1.13 Applications	22
1.14 Metal Phosphonates	23
1.15 Synthesis	24
1.16 Applications	25
1.17 Reference	26
2 Aims	35
2.1 References	36
3 Experimental	37
3.1 X-ray Diffraction	37
3.2 Least Squares refinement	42
3.3 Quality of data	44
3.4 Crystallography	46
3.5 Single Crystal X-ray Diffraction	50
3.6 Selecting a Crystal	50
3.7 X-ray Tubes	51
3.8 Rotating Anode	52
3.9 Synchrotron Radiation	53

3.10 Crystal structure determination	57
3.11 Exposing the Crystal to X-rays	57
3.12 Processing data	59
3.13 Structure solution	61
3.14 Final model	62
3.15 Station 9.8	62
3.16 Powder diffraction	64
3.17 Experimental	66
3.18 Rietveld refinement	67
3.19 Nuclear Magnetic Resonance (NMR)	69
3.20 Solution NMR	69
3.21 Zeeman Interaction	71
3.22 Chemical Shift	72
3.23 Solid state NMR	73
3.24 Solid vs. solution state NMR	73
3.25 Chemical shift anisotropy	74
3.26 Dipolar interactions	75
3.27 Magic-angle spinning	76
3.28 Decoupling	77
3.29 Quadrupolar interactions	77
3.30 Multiple Quantum (MQ) MAS	77
3.31 CASTEP	78
3.32 Techniques used	79
3.33 Thermogravimetric Analysis (TGA)	79
3.34 Bibliography	80
4 Ionothermal Synthesis of Metal Phosphonates	82
4.1 Introduction	83
4.2 Aim	83
4.3 Aluminium Phosphonates	83
4.4 Gallium Phosphonates	85

4.5 Aluminium Phosphonates	86
4.6.1 $\text{Al}_2\text{F}((\text{C}_4\text{H}_9)\text{PO}_3)_6(\text{OH})_2(\text{C}_8\text{N}_4\text{H}_6)_2$	86
4.6.2 Experimental	86
4.6.3 Powder X-ray diffraction data	86
4.6.4 Single crystal X-ray diffraction data	87
4.6.5 Results and discussion	89
4.6.6 Thermogravimetric analysis	91
4.7 Gallium Phosphonates	92
4.7.1 $\text{GaF}(\text{HO}_3\text{PCH}_3)_2(\text{NH}_3\text{CH}_3)_2$	92
4.7.2 Experimental	92
4.7.3 Single Crystal data	92
4.7.4 Results and discussion	93
4.7.5 Powder X-ray diffraction data	96
4.7.6 Thermogravimetric analysis	96
4.8.1 $\text{Ga}_2(\text{O}_3\text{PCH}_3)_3$	97
4.8.2 Experimental	97
4.8.3 Single Crystal data	97
4.8.4 Results and discussion	99
4.8.5 Thermogravimetric analysis	102
4.9.1 $\text{Ga}_6(\text{C}_4\text{N}_2\text{H}_6)_4\text{F}_2(\text{O}_3\text{PCH}_3)_8(\text{H}_2\text{O})_{0.4}$	103
4.9.2 Experimental	103
4.9.3 Single Crystal data	104
4.9.4 Powder X-ray diffraction data	108
4.9.5 Thermogravimetric analysis	108
4.10.1 $\text{Ga}_2\text{F}(\text{C}_4\text{H}_9\text{PO}_3)_4\text{H}_{2.5}(\text{C}_7\text{N}_2\text{H}_{11})_{0.5}$	109
4.10.2 Experimental	109
4.10.3 Powder X-ray diffraction data	109
4.10.4 Single crystal X-ray diffraction data	109
4.10.5 Results and discussion	111

4.11 Conclusion	113
4.12 References	117
5 High resolution charge density X-ray diffraction	121
5.1 Introduction	121
5.1.1 Quality of data	126
5.1.2 Experimental electron density	127
5.1.3 Experimental Problems	129
5.1.4 Multipole model	131
5.1.5 Processing	131
5.1.6 Analysis	133
5.1.7 Atoms in molecules	134
5.1.8 Gradient vector	136
5.1.9 The Laplacian of Charge density	137
5.1.10 References	138
5.2 High Resolution X-ray Diffraction Studies of a Crystallised Ionic Liquid and a Metal Organic Framework	141
5.2.1 Introduction	141
5.3.1 High Resolution X-ray diffraction study of 1-Ethyl-3-methylimidazolium hexafluorophosphate, a crystallised ionic liquid	144
5.3.2 Experimental	145
5.3.3 The structure of 1-Ethyl-3-methylimidazolium Hexafluorophosphate	145
5.3.4 Data Collection and Processing Strategy	147
5.3.5 Residual electron density	149
5.3.6 Deformation Density	151
5.3.7 Topological features	152
5.3.8 Bonding nature	154

5.4.1 High resolution data of the Metal organic framework SIMOF-1	156
5.4.2 Experimental	156
5.4.3 Structure	156
5.4.4 Data collection	158
5.4.5 Results	158
5.4.6 Topological features	163
5.5 Conclusion	164
5.6 References	167
6 Structure and NMR assignment in AlPO4-15: a combined study by diffraction, MAS NMR and first-principles calculations	171
6.1 Introduction	171
6.2 Aim	173
6.3 Experimental	174
6.3.1 Synthesis	174
6.3.2 Single Crystal X-ray Diffraction	175
6.3.3 NMR spectroscopy	175
6.3.4 Calculations	176
6.4 Results and Discussion	177
6.5 Conclusion	187
6.6 References	188
7 Gas Storage in Porous Materials	191
7.1 Introduction	191
7.2 Applications	192
7.2.1 Hydrogen	192
7.2.2 Carbon Dioxide	194
7.2.3 Sulfur Dioxide	194
7.2.4 Nitric Oxide	195
7.2.5 Hydrogen Sulphide	196
7.3 Aim	197
7.4 Environmental gas cell	198
7.5 CPO-27-Co	200

7.6 In-situ study of Sulfur dioxide	200
7.6.1 Experimental	200
7.6.2 Results	202
7.7 In-situ study of Nitric Oxide	204
7.7.1 Experimental	204
7.7.2 Results	206
7.8 Conclusions	208
7.9 References	210
8 In-situ comparison of ionothermal prepared zeolite under microwave and conventional heating	214
8.1 Introduction	214
8.2 Aim	216
8.3 Experimental	216
8.4 Results and Discussion	220
8.4.1 Conventional Synthesis of SIZ-4	220
8.4.2 Microwave Synthesis of SIZ-4	222
8.5 Conclusions	224
8.6 References	225
9 Conclusions and Further Work	227
9.1 Conclusion	227
9.2 Further Work	231
9.3 References	233

1 Zeolites and Zeotypes

1.1 Introduction

It is now over 250 years since the first zeolite ‘Stilbite’ was discovered by the Swedish mineralogist Axel Fredrick Cronstedt.¹ Zeolites are named from the Greek zein (boil) and lithos (stone), meaning boiling stone, this name arose because the natural mineral appeared to boil when it was heated¹. We now know that this affect was due to water escaping from the characteristic pores of these fascinating materials.

Zeolites are microporous crystalline solids with well-defined structures. Traditional zeolites are composed of silicon, oxygen and aluminium in a crystalline framework, with cations/organic/water molecules contained within the uniform pores which range in size from 3 to 13.2Å,² with cloverite having the largest pores to date.³ Other similar structures which fall under the classification of zeolites are known based on elements other than silicon, such as gallium, aluminium, phosphorus, vanadium etc. but for traditional zeolites the silicon and aluminium atoms are tetrahedrally coordinated and connected to each other through shared oxygen atoms. The charge of the framework needs to be balanced; $\text{SiO}_{4/2}$ has no overall charge whilst $\text{AlO}_{4/2}$ has an overall negative charge which is balanced from extra framework cations to ensure electroneutrality.

Zeolites are just one form of porous material, there are a wide number of variations, known as zeotypes such as, metal phosphates, which are porous and highly crystalline however they differ in their “chemical makeup”. The most famous is probably that of aluminium phosphates (AlPO_4) which were first discovered by Flanigen *et al*⁴ as AlPO_4 -5. These zeotypes consist of Al^{3+} , PO_4^{3-} and are structurally very similar to zeolites.

However, they do not need to have charge balancing ions due to their molar ratios being in the order of 1:1. Gallium, vanadium and many other metals can now be incorporated into a crystalline form to synthesis many different zeotypes.^{5,6}

The main interest in zeolites is due to their crystalline form and well defined pore structure which lend themselves to many useful applications. Zeolites are used heavily in diverse areas from catalysts in the petrochemical industry to additives in washing powder and more recently have been shown to have an importance in medicine.⁷

Figure 1 shows a typical zeolite (ZSM-5) which was first developed by Mobil Oil, this framework is heavily used in the petrochemical industry as a catalyst in hydrocarbon conversion.⁸

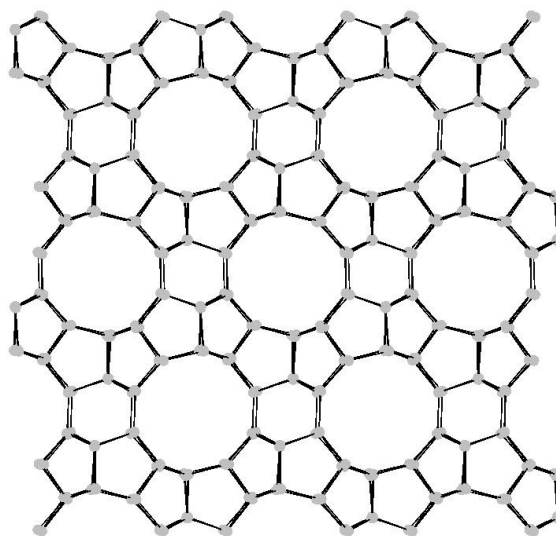


Figure 1.1: Structure of ZSM-5 with the porous nature of the material clearly visible. The grey atoms represent the tetrahedral sites (Si, Al) in the structure with each line representing a T-O-T bond, the oxygen atoms have been removed for clarity.

A zeolite structure can be described in terms of building units and is composed of tetrahedral TO_4 units ($\text{T} = \text{Al}, \text{Si}, \text{P}, \text{Ga}, \text{M}^{n+}$) known as primary building units which share vertices to form the overall architecture of the material. These tetrahedral units can join together in numerous conformations to form a wide variety of rings and cages known as secondary building units (SBUs) of which there are currently 20 SBUs (*Figure 1.2*) recognised in the various zeolites. The secondary building units in turn can then join to give tertiary units (*Figure 1.3*) which eventually make up the diverse array of zeolites known to date.

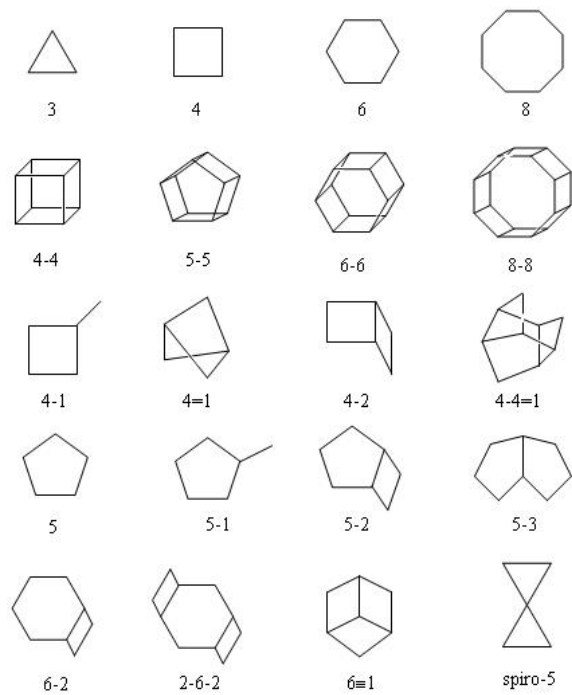


Figure 1.2: Example of the many secondary building units (SBUs) found to date in zeolites.⁹

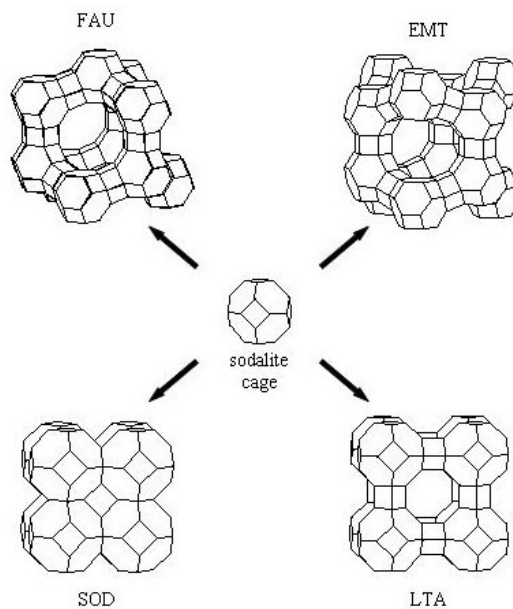


Figure 1.3: The sodalite cage¹⁰ can be arranged in various ways to form different frameworks and is an example of a tertiary building unit.

1.2 Zeolite synthesis

There are over 40 naturally occurring zeolites¹¹ and a growing list of currently over 167¹² synthesised zeolites. Conventional zeolite synthesis is achieved via a hydrothermal process similar to that first employed by Barrer¹³ in 1948 where he tried to mimic in the laboratory the geochemical environment in which natural zeolites form. This involved the use of high pressure and temperature, like those found within the earth's crust.

A typical synthesis involves reactants being mixed with a template and heated to varying temperatures in a Teflon-lined autoclave (*Figure 1.4*) for a given period of time. The autoclave is then removed from the oven and cooled to room temperature, the product is then filtered, washed with water and dried. The material is examined for its crystallinity using powder X-ray diffraction, a useful technique for identifying known structures quickly by comparing the results to a database of known materials (ICDD¹⁴).

In true hydrothermal synthesis water is used as a solvent. However, it is believed that the water may interfere with the templating effect of the SDA as substituting water with alcohol or glycol results in different compositions.¹⁵ This leads us to solvothermal synthesis where a non-aqueous solvent is used to synthesise various zeotypes. It has been reported¹⁶ that this synthesis can help produce bigger and purer crystals compared to hydrothermal synthesis. Bibby and Dale successfully synthesised aluminosilicate sodalite from ethylene glycol, fumed silica and sodium hydroxide.¹⁷ Ethylene glycol has also been reported as an important additive in the manufacture of other aluminium phosphates such as AlPO_4 -5, 11, 21¹⁸ and 17.¹⁹

During hydrothermal synthesis there tends to be a high vapour pressure due to the use of water resulting in safety issues. However, a new method for zeolite synthesis has recently been reported²⁰ whereby an ionic liquid is used as both the template and solvent in an ionothermal method. An ionic liquid is defined as a material which exhibits ionic character, and can be molten at or below 100°C.²¹ They have many potential uses in industry as they are non-volatile solvents and can be designed to be environmentally benign²¹ and are therefore known as green chemicals.

Their use in zeolite synthesis is extremely interesting thanks to their dual role of solvent and SDA leading to many novel frameworks. Morris *et al*²⁰ reported that four different zeolite syntheses were possible using the same ionic liquid whilst varying other conditions. SIZ -1,-3,-4,-5 were synthesised from the 1-methyl 3-ethyl imidazolium bromide as the template. Other novel materials such as SIZ-6²² and SIZ-7²³ can also be prepared. A major advantage over hydrothermal and traditional solvothermal reaction conditions is that ionothermal synthesis takes place at ambient pressures due to the ionic liquid's vanishingly low vapour pressure, thus avoiding the high autogenous pressures (up to 15 atm at 200°C) and associated safety concerns that accompany hydrothermal/solvothermal synthesis. Another key benefit for ionothermal synthesis is that the ionic liquid can be recycled thus reducing the cost of manufacture.

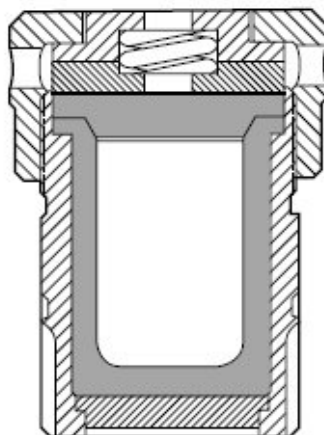


Figure 1.4: A schematic of a Teflon lined autoclave (Parr bomb²⁴), designed to release pressure build up safely.

1.3 SDAs in zeolite synthesis

The use of the template or structure directing agent/organic additive is thought to be a major factor in the crystallisation of a zeolite as it is believed that it dictates the size and shape of the pores in the material.

The mechanism for zeolite synthesis is still much debated but it is believed that there are three roles played by the organic additive; (a) space filling agents, where space filling refers to the organic occupying the voids to help stabilise the structure against solvent water which could prevent the growing of the framework, (b) structure directing agents which implies that the SDA is responsible for one unique structure and (c) true templates as defined by Davis *et al*¹¹ and occurs when the zeolite adopts the same geometric and electronic configuration as the organic guest.

The structure directing property of an organic has been demonstrated in the synthesis of sodalite. Tetramethylammonium cations were used in the synthesis of the framework

and were located within the pores after crystallization.^{25,26} The cations were too large to leave the pores after synthesis indicating that the framework was formed around the template. It has been shown that different zeolites can be synthesised with the same SDAs. For example tripropylamine can be used as a template in the synthesis of $\text{AlPO}_4\text{-5}$ and $\text{AlPO}_4\text{-15}$ ^{27,28} indicating that there are other influences affecting the production of these frameworks with the organic acting as a space filling agents in some cases. There is currently one known example of true templating²⁹ where a trispyrrolidinium cation is used in the synthesis of ZSM-18 (*Figure 1.5*). This was first reported by Davis *et al*¹¹ where they showed that the template was held in a cage within the zeolite. Calculations showed that no rotation of the template could occur and the template was a perfect match with the shape of the pore indicating true templating was taking place.

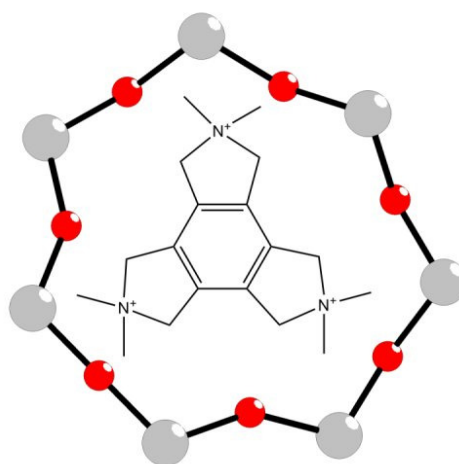


Figure 1.5: Example of true templating. ZSM-18 is templated by trispyrrolidinium cation

The ideal proposed mechanism for crystal growth starts with the reagents being dissolved in a solvent which form nucleation sites that grow to form the final product.

The problem with this mechanism is that there are so many variables which can affect the crystal growth (temperature, solvent, pH, pressure, molar ratios, time, template etc.) that it is an almost impossible task to really understand the reasons for crystal growth. *Figure 1.6* depicts the most popular mechanism for zeolite synthesis as proposed by Davis *et al*³⁰ whereby the hydration sphere around the organic template is replaced partially or fully by silicate species to form an organic–inorganic species which can go on to help in the formation of the final crystalline product.

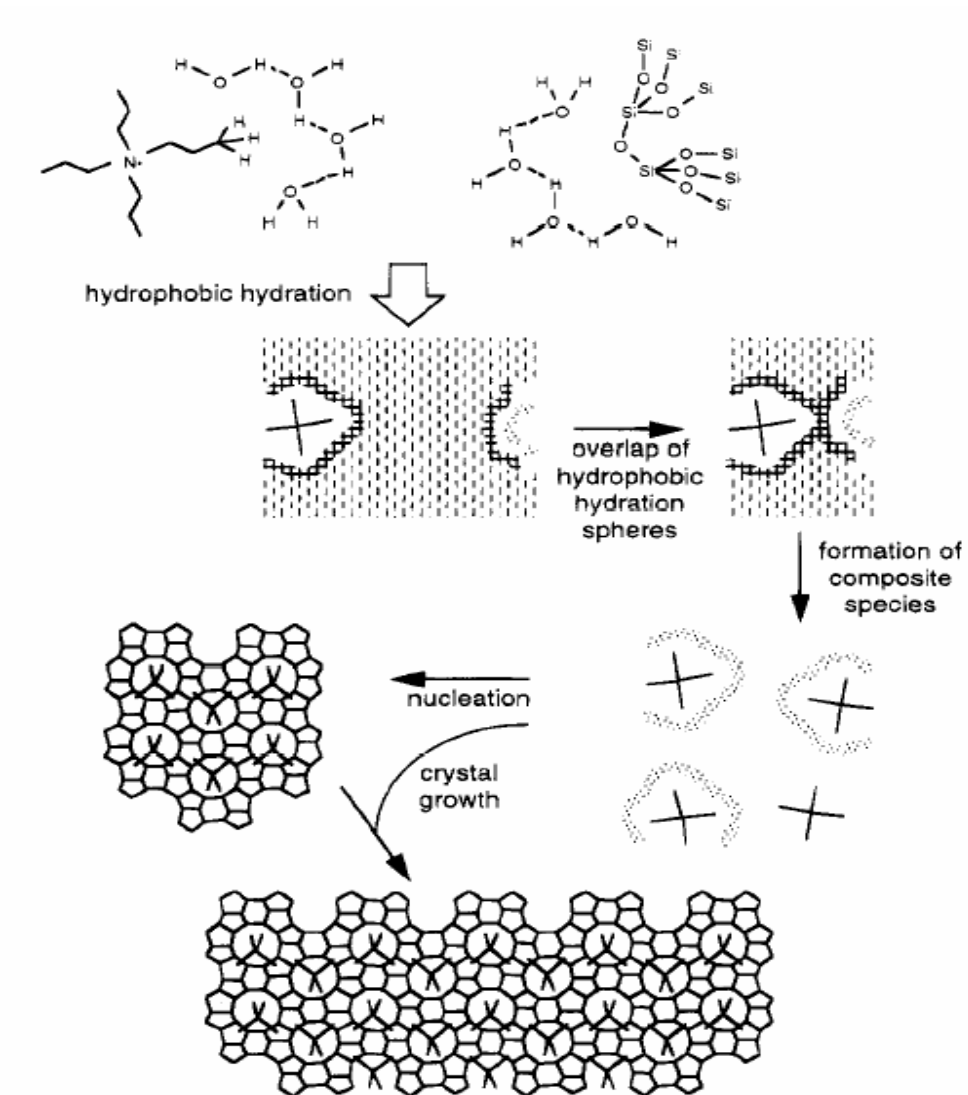


Figure 1.6: Proposed zeolite synthesis by Davis et al³⁰. The hydration sphere around the organic template is replaced partially or fully by silicate species to form an organic-inorganic species which can then go onto help in the formation of the final crystalline product.

To make these fascinating materials porous the template has to be removed. This can be done via calcination whereby the sample is heated to a high temperature whilst passing a gas over the sample, the template breaks down and is lost from within the framework.

This can however have a detrimental effect to the zeolite causing weakening of the structure and sometimes a loss of crystallinity. Recent research by Lee *et al*^{31,32} has demonstrated that it is possible to remove the template under milder conditions by using a ketal (8,8-dimethyl-1,4-dioxo-8-azoniaspiro[4,5]decane) containing species to synthesise the framework ZSM-5 and subsequently remove the template by altering the pH. This work shows that it is possible to remove templates under milder conditions but also highlights the possibilities of reusing the template and therefore lowering the cost of manufacture.

1.4 Ionic liquids

Ionic liquids (ILs) are a very popular solvent at the moment thanks to their “green and designer properties” making them suitable for many applications³³ in both organic and inorganic chemistry. An IL is defined as a liquid which exhibits ionic character, however there are other characteristics associated with these materials such as a low vapour pressure and melting points at or below 100°C. Many of these interesting properties are due to the size and shape of the anion and cation³⁴, an increase in size of anion leads to a decrease in melting point³⁵. Viscosity is another tailorable property which is determined by the strength of the van der Waals interactions or the solvent’s ability to form hydrogen bonds. With these materials being readily altered for specific tasks there is little wonder to their desirability and has led to the alias of “designer solvent”³⁶. *Figure 1.7* is a scheme of the important cations heavily used in ionic liquid synthesis.

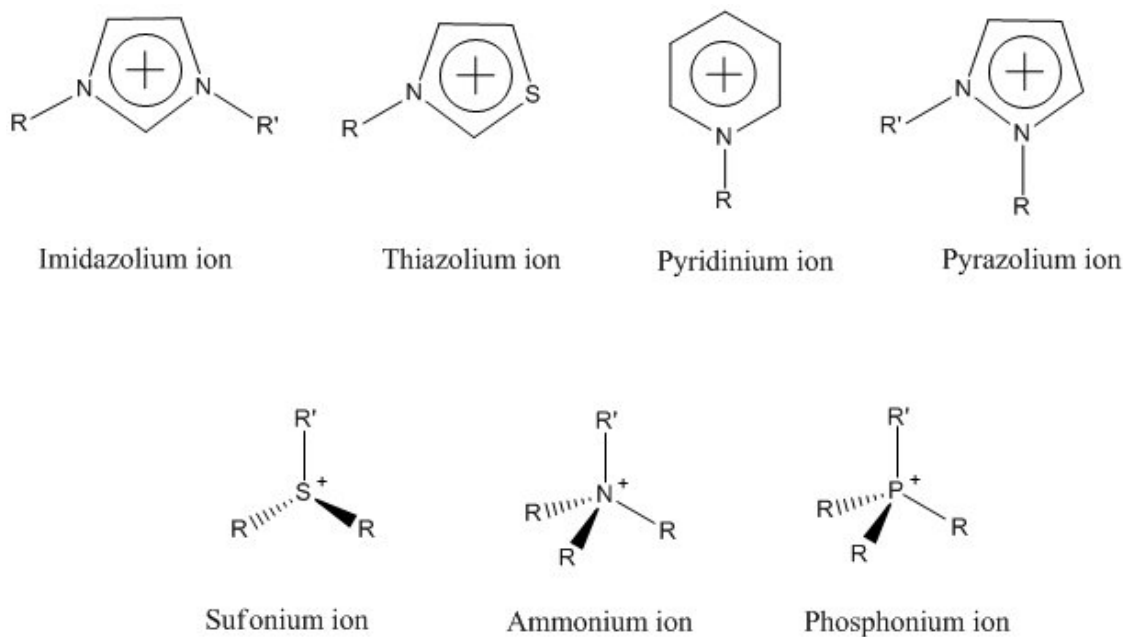


Figure 1.7: Important cations used in ionic liquid synthesis.

Selectivity of physical properties of ionic liquids can also be achieved by changing the length of the alkyl groups on the rings altering viscosity, hydrophobicity and melting points. In fact the number of possible combinations is unmeasurable and as such it would be an impossible task to experimentally calculate all the properties of various ionic liquids however with the improvement of computers and software it is possible to calculate theoretical properties using computer simulations and modelling techniques.³⁷ Such studies have involved examining some properties such as thermodynamics, structural, dynamic properties and more recently hydrogen bonding on single ion pairs with work by Dong *et al*³⁸ showing it is possible to investigate the hydrogen bonding on multiple ion pairs leading to a more realistic model. Work on these systems has shown

that monoatomic anions (halides) form one hydrogen bond with the cation whilst the molecular anions (hexafluorophosphate) form multiple hydrogen bonds.

ILs have become very desirable in materials chemistry especially in zeolite and framework synthesis whereby the ionic liquid has a dual role as structure directing agent (SDA) and solvent³⁹ in an ionothermal method. This property has helped reduce the number of reagents required and therefore reduced the number of variables previously present in materials synthesis. However, as in conventional hydrothermal synthesis it is possible to obtain different frameworks from the same template/ionic liquid³⁹ (*Figure 1.8*). There must be other interactions which can contribute to the synthesis of novel materials. Ionothermal synthesis by definition requires that no water be added to the reaction vessel, however ILs are extremely hygroscopic⁴⁰ and readily capture water from the atmosphere, the reagents themselves are also considered wet in nature, this water content has already been shown to have an effect on the synthesis of aluminophosphates as work by Morris *et al* showed that pre-baking a reaction mixture at 50°C for 2 hours resulted in the formation of SIZ-3³⁹ whilst not heat treating the mixture resulted in the formation of SIZ-4.³⁹ This finding has been attributed to the removal of reagent water.⁴¹ These findings have led to research investigating whether trace amounts of water have an effect on the synthesis process. Work by Ma *et al*⁴² investigated how water content can affect the crystallinity of various aluminophosphates, they concluded that the addition of water can greatly enhance the crystallisation, this study was only made possible thanks to the use of ionothermal synthesis as conventionally hydrothermal

methods contain excess amounts of water molecules making it very difficult to investigate their interaction.

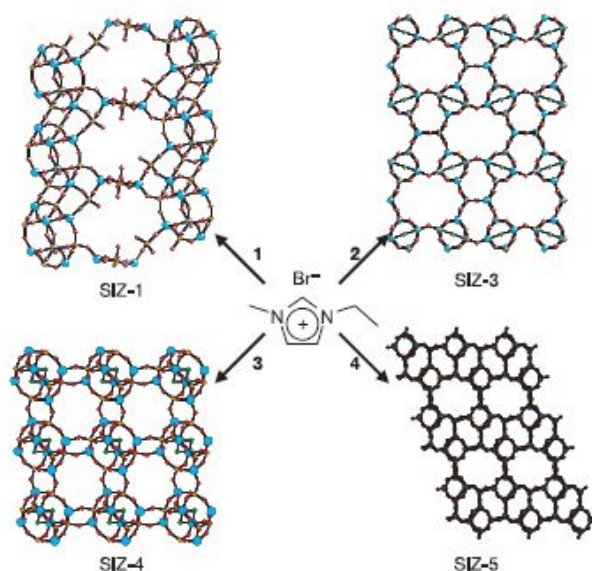


Figure 1.8: Four different aluminophosphates can be synthesised from 1-ethyl-3-methylimidazolium bromide.²⁰

1.5 Applications

There are currently only a few commercially used processes where ionic liquids are used such as the preparation of dihydrofurans⁴³ used by Eastman chemical company and the BASIL⁴⁴ (Biphasic Acid Scavenging utilising Ionic Liquids) process whereby the ionic liquid scavenges byproduct acids which may go on to produce side reactions. Even though only a few commercial applications exist ionic liquids are being used in research in many areas thanks to their unique properties such as in biological reaction media⁴⁵ whereby enzymes are found to be stable and can lead to improvements in selectivity and

reactivity in some cases.⁴⁶ They have also found a use in ultra thin batteries,⁴⁷ in heavy metal extraction⁴⁸ and even their role in hydrogen storage is being investigated.⁴⁹

1.6 Ionic liquid preparation

There are many different ionic liquids and many different ways to prepare them. However, here-in I will describe the synthesis of 1-ethyl-3-methylimidazolium bromide which was used mostly throughout this PhD.

Ionic liquids are reactive in air and have to be prepared in an inert atmosphere, achieved using a Schlenk line. The ionic liquid 1-ethyl-3-methylimidazolium bromide (EMImBr) was prepared as described.⁵⁰



Figure 1.9: Synthesis of 1-ethyl-3-methylimidazolium bromide.

Degassed ethylbromide (88.25g, 0.81mol) was added to ice cooled 1- methylimidazole (46.979g, 0.57mol) with constant stirring, the mixture was then heated under reflux for 3 hours at 40°C and allowed to cool to room temperature. Ethyl acetate was added to enable the product to crash out, which was then filtered quickly and washed with ethyl acetate and dried under vacuum to give a white solid (1-ethyl-3-methylimidazolium bromide). The EMImBr was kept under an inert atmosphere. The ionic liquid was

characterised using $^1\text{H-NMR}$ (CDCl_3): δ_{H} 10.33 (1H, s), 7.60 (2H, quin, $J=2$), 4.41 (2H, q, $J=7$), 4.11 (1H, s) and 1.59 (3H, t, $J=7$).

1.7 Eutectic mixture

Eutectic mixtures (EU) are similar to ionic liquids, they consist of two or more compounds which when mixed have a lower melting point than either of its constituents. They can exist in solid form by themselves but if they are mixed they can form a liquid and thus make them suitable for ionothermal type reaction. The eutectic mixture used within this thesis consist of a mixture of urea and choline chloride which have a melting point of 133 and 302°C respectively but when mixed thoroughly in a ratio of 2:1 as investigated by Abbott *et al*⁵¹ have a melting point of 12°C arising from the hydrogen bond interaction between the urea and the choline chloride.

The advantage of using a eutectic mixture over an ionic liquid is the time taken to prepare the sample and also eutectic mixtures constituents tend to be cheaper than those of ionic liquids

1.8 The Fluoride method

Zeolite synthesis has been greatly improved thanks to work by Flanigen and Patton⁵² who replaced the traditional hydroxide ions with F^- ions as the mineralising agent⁵² in the synthesis process which made it possible to obtain zeolites at lower than normal pHs. The use of fluoride in zeolite synthesis has led to many new architectures^{53,54} as it

imposes a negative charge on the framework which requires a positive charge from the structure directing agent to ensure electroneutrality.

The addition of a fluoride source (NH_4F , NH_4HF_2 and HF) has helped greatly in the quality of the crystalline material produced but has also found other roles in the synthetic process⁵⁵ such as a catalytic affect in the formation of $\text{AlPO}_4\text{-14A}$ ⁵⁶ and as a structure directing agent as it has been located in double four rings such as in cloverite³ (Figure 1.11). Fluoride anions have also been shown to have an affect in templating with the F^- being directly bound to the framework increasing the coordination such as in $\text{AlPO}_4\text{-5}$ ⁵⁷ (Figure 1.10) and AlPO-CJ20 .⁵⁸

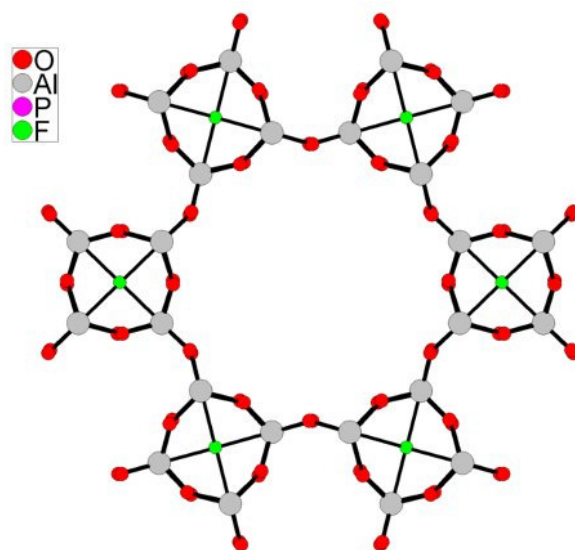


Figure 1.10: In $\text{AlPO}_4\text{-5}$ the Fluoride atoms are bound to the framework.

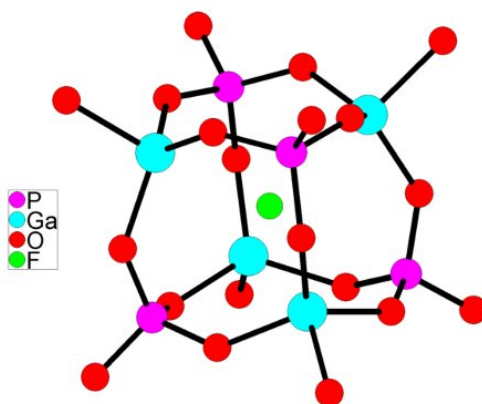


Figure 1.11: Cloverite double four ring with the F anion acting as a template in the centre of the cubic unit.

1.9 Applications of Zeolites.

Zeolites have found many uses since their discovery 250 years ago with their highly crystalline porous nature making them suitable for many applications such as molecular sieves and in the petrochemical industry, Zeolite Y is used for fluid catalytic cracking.⁵⁹ They also have environmental applications as they can remove volatile chemicals from air streams and are a cost effective method to remove heavy metals from industrial waste.⁶⁰

One heavily used application of zeolites is in washing powders as ion exchangers due to their balancing cations. If a cation is “soft” such as sodium the zeolite can be used as an ion exchanger by removing the hard magnesium and calcium from the water and

replacing it with sodium. If the balancing cations of the zeolite are H^+ atoms the framework becomes known as a hard acid and is useful as a solid acid catalyst. Such as in the methanol to gasoline conversion with ZSM-5 as the catalyst.

With their high porosity zeolites can be used as shape selective catalysts and are able to discriminate reactants and products due to their size and shape, thus preventing unwanted molecules passing through the structure (Figure 1.12).

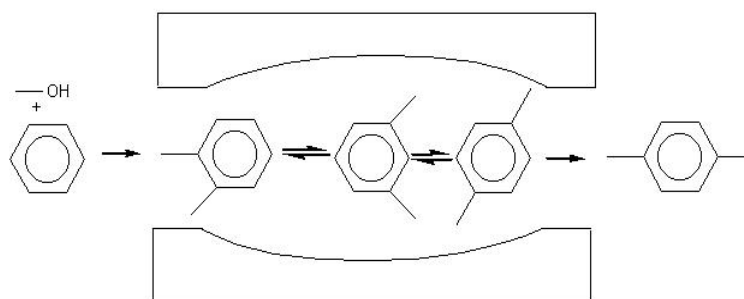


Figure 1.12: Shape selective properties of a zeolite. Only the para isomer can vacate the pore, whilst the ortho and meta isomers are trapped within the pore.

Most current applications utilize aluminosilicate zeolites. However, it has recently been reported by Wilson *et al*⁶¹ that there are now commercial applications for silico aluminium phosphates such as SAPO-34 which can be used as a catalyst in the conversion of methanol to olefins.

Zeolites also have medical uses such as in the prevention of traumatic bleeding⁶² and magnetic resonance imaging (MRI)⁶³ whereby a toxic contrast agent (Gd^{3+}), can be contained within the pores of the zeolite and administered without any serious side

effects. They are also being used by Morris *et al*⁷ to effectively store and deliver nitric oxide for use as a therapeutic agent.

1.10 Inorganic organic hybrids

Inorganic organic hybrids are a great way to provide functionality to frameworks as the organic part can be adapted for specific roles and can provide a wide range of structures and properties.⁶⁴ These hybrids encompass a wide variety of materials however the most popular being that of metal phosphonates and more recently metal organic frameworks.⁶⁵

1.11 Metal Organic Frameworks

Metal organic frameworks (MOFs) are a family of nanoporous material popularized by Yaghi *et al*⁶⁶ and consist of a transition metal co-ordinated and linked by poly-atomic organic molecules. They are akin to zeolites in that they are porous but with the added benefit of being able to increase their pore size by using larger organic linkers. MOFs have the potential to perform some of the current applications that zeolites do except they are more versatile as they can be engineered to various sizes by increasing the size of the linker⁶⁷ resulting in very large surface areas (exceeding $5000\text{m}^2\text{g}^{-1}$ ^{68,69}). Unlike zeolites they have been shown to ‘breathe’ resulting in either an expansion or contraction of the framework^{70,71} depending on the guest in the framework, Loiseau *et al*⁷¹ showed how hydrogen bonding between the water and the hydrophilic part of Al-

MIL-53 causes the framework to shrink from 16.675(3)x12.813(2) Å² for the calcined version to 19.513(2)x7.612(1) Å² for the hydrate. These are known as 3rd generation compounds⁷² and respond to external stimuli such as light, electric field and guest molecules which cause a reversible change in the pores. The 2nd generation systems can show stability without the need for a guest, whilst the 1st generation compounds require a guest molecule and collapse on removal of the guest. Unlike the thermally stable frameworks of zeolites, MOFs tend to be unstable⁷³ and are subject to decomposition from high temperatures⁷⁴ as a result they can rarely be heated above 500°C.⁷¹ Li *et al*⁷⁵ have shown that it is possible to increase stability by using dicarboxylates as linkers which could have great benefits to the industry as if stable MOFs can be produced it would lead to frameworks which can be designed for specific tasks.

1.12 Synthesis

Metal organic frameworks can be prepared in a similar way to zeolites, typically via a hydro/solvothermal method⁷⁶ where solvents such as water, alcohol, dialkyl formamides and pyridine are heated in a Teflon-lined autoclave alongside a metal and organic linker for varying times and temperatures and result in a crystalline material. More recently however the use of ionic liquids has been shown to produce novel metal organic frameworks^{77,78,79,80} with some interesting properties such as the use of a chiral ionic liquid leading to the production of chiral frameworks^{81,82} to provide high selectivity in asymmetric catalysts.⁸³ Ionothermal synthesis has the property of a low vapour pressure and as such microwave heating can be more readily used as there is less danger of the

sample tubes exploding. Work by Lin *et al*⁸⁴ has shown that the metal organic frameworks of (EMIm)₂[Ni₃(TMA)₂(OAc)₂] and (EMIm)₂[Ni₃(TMA)₂(OAc)₂] can be synthesised with the use of 1-ethyl 3-methyl imidazolium bromide and microwave heating in 50 minutes compared to 3 days for conventional heating to result in purer phase and higher crystallinity. Not only does microwave heating result in faster crystallisation times it also helps to produce samples not readily made via conventional methods. Jhung *et al*⁸⁵ showed that the structure [Ni₂₂(C₅H₆O₄)₂₀(OH)₄(H₂O)₁₀].38H₂O was produced instead of the expected MIL-77 ([Ni₂₀(C₅H₆O₄)₂₀(H₂O)₈].40H₂O) structure during microwave heating. This clearly shows how microwave assisted reactions can help to increase and develop the materials on offer.

1.13 Applications

MOFs have not found any commercial uses as yet probably due to their relatively low thermal stability. However, their varying pores sizes lend themselves to some very interesting potential applications. Examples are catalysts and in separation⁸⁶ but probably the most publicised application for these frameworks is in gas storage for potential energy^{87,88,89} storage, with hydrogen being a hot topic with the U.S. Department of Energy setting targets for hydrogen storage to 6wt% by 2010 and 9wt% by 2015.⁹⁰ Environmental applications are also a great concern at the moment with interest in the reduction of green house gases such as the removal of CO₂ from the flue exhaust of power plants,⁹¹ and other toxic gases given off in industrial processes such as the release of sulphur dioxide which can oxidize to produce sulfuric acid (acid rain). Research into

medical applications is also being applied to metal organic frameworks such as the storage of nitric oxide for drug delivery⁷ to prevent platelet aggregation and aid in wound repair.^{7,92}

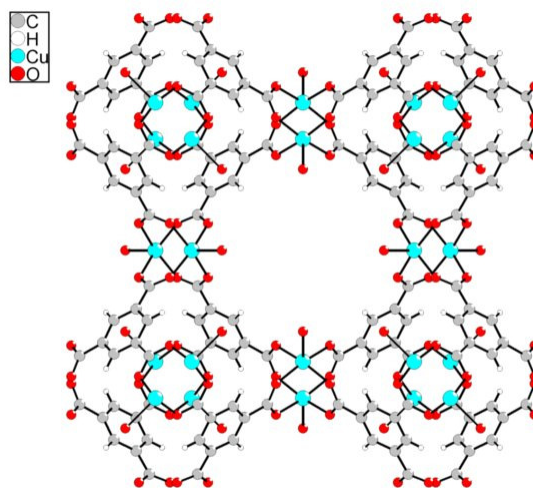


Figure 1.13: A typical metal organic framework (HKUST-1⁹³) showing the metal ions (Cu²⁺) connected via benzenetricarboxylate linking to form a highly porous structure.

1.14 Metal Phosphonates

Metal organic frameworks are just one form of inorganic-organic hybrid, metal phosphonates (M(RPO₃)_n) have been known since 1976⁹⁴ and are a great addition to hybrid chemistry as they are similar to the well documented stable inorganic metal phosphates whilst being able to provide functionality by varying the phosphonic acid precursor. Unfortunately it is often quite difficult to incorporate these functional groups in a way to make them porous, like in the phosphate family already described in this thesis. This is due to the organic groups being too bulky, resulting in layered,^{95,96} pillared^{97,98} or molecular^{99,100,101} structures.

There has been much research into the different forms of phosphonates available by varying the metal valence such as trivalent (Fe, Ga, Co, Cr, Mn, and Al)^{102,103,104} divalent (Zn, Mn, Cu)^{103,105,106} and tetravalent (Zr, Sn).¹⁰⁷ Tetravalent metals are interesting but tend to form only layered structures.¹⁰⁸ The divalent and trivalent phosphonates also tend to form layered materials. However, it has been possible to synthesise phosphonates which are microporous^{109,110} as shown by Drumel *et al* where a divalent zinc ion was used with 2-amino-ethyl phosphonic acid to prepare the porous framework $Zn(O_3PC_2H_4NH_2)$. Maeda *et al* also demonstrated that microporous aluminium methyl phosphonates such as AlMepO- α and AlMepO- β ^{111,112} have pore diameters of around 6.2Å, with the methyl groups from the phosphonate pointing into the pores, a feature not present in aluminium phosphates. Wright *et al*¹¹³ successfully synthesised two phosphonates with pores greater than 7Å $[Ni_2(H_2O)_2L].5.4H_2O$ (L=N,N'-piperazinebis(methylenephosphonic acid)) and $[Co_8L'_6(CH_3CO_2)_3(OH,H_2O)_6].(NH_4)(H_2O)_{11}$ (L'=2-methylated derivative). However even with such a large aperture only the $[Ni_2(H_2O)_2L].5.4H_2O$ framework could adsorb nitrogen as the Co phosphonate was prohibited by the charged molecules present in the pores. Other porous frameworks have been synthesised such as MIL-91¹¹⁴ which adsorbs nitrogen, however many of the frameworks do not produce pores of sufficient size for molecules larger than water to enter.¹¹⁵

1.15 Synthesis

Metal phosphonate synthesis consists of a metal (node), a phosphonate group (connector), mineralising agent (HF), a structure directing agent and a solvent such as

water/alcohol in a hydro/solvothermal type reaction, the reagents are heated at various times and temperatures to result in a crystalline product. The ionothermal synthesis method has been developed through this thesis to result in the synthesis of novel materials and will be discussed in chapter 4.

1.16 Applications

Highly selective microporous materials are very desirable in the chemical industry. Chiral frameworks are believed to have potential to select specific enantiomers. Fredoueil *et al*¹¹⁶ demonstrated that it was possible to produce an enantiomerically pure layered phosphonate (R)-Zn[O₃PCH₂P(O)(CH₃)(C₆H₅)]·H₂O. Although this did not produce a porous framework it does highlight the possibilities for chiral framework synthesis.

Even if the more desirable porous nature of a metal phosphonate cannot be achieved, applications are being found for these interesting materials in the form of cation exchangers,¹¹⁷ NLO^{118,119} materials and as solid supports. Clearfield *et al*¹²⁰ used crown ethers as the functional group as they have potential applications in the transportation of ionic species in living tissues, the use of the solid support ensures the expensive ethyl can be recovered.

1.17 References

- ¹ A.F. Cronstedt, *Adak. Handl. Stockholm*, 1756, **17**, 120
- ² <http://www.bza.org/>
- ³ M. Estermann, L.B. McCusker, C. Baerlocher, A. Merrouche and H. Kessler, *Nature*, **352** 1991, 320-323
- ⁴ S.T. Wilson, B.M. Lok, C.A. Messina, T.R. Cannan and E.M. Flannigen, *J. Am. Chem. Soc.*, **104**, 1982, 1146
- ⁵ T. Loiseau and G. Férey, *Solid State Sciences.*, 2005, **7**, 1556-1560
- ⁶ R. Shpanchenko, A. Mitiaev, V. Chernaya, E. Antipov, H. Sakurai and E. Takayama-Muromachi, *J. Solid. State. chem.*, 2005, **178**, 3014-3019
- ⁷ P.S. Wheatley, A.R. Butler, M.S. Crane, A.G. Rossi, I.L. Megson and R. E. Morris, *Molecular sieves: from basic research to industrial applications, pts a and b studies in surface science and catalysis*, 2005, **158**, 2033-2040
- ⁸ G. Mohr, T. Chen, K. Clem, P. Janssen M. Ruziska, J. Verduijn, US patent WO9616004 1996
- ⁹ R.E. Morris, *J. Mater. Chem.*, 2005, **15**, 931-938
- ¹⁰ P.S. Wheatley, 'Synthesis of Open Framework Materials Using Azamacrocycles as Structure Directing Agents', Thesis, St. Andrews, 2003
- ¹¹ M. Davis and R.F. Lobo, *Chem. Mater.*, 1992, **4**, 756-768
- ¹² <http://www.iza-structure.org/databases/>
- ¹³ R.M. Barrer, *J.Chem.Soc.*, 1948, 127
- ¹⁴ www.icdd.com

- ¹⁵ S.J.Wiegel, S.C. Weston, A.K.Cheetham G.D Stucky, *Chem. Mater.*, 1997, **9**, 1293
- ¹⁶ A. Kuperman, S. Nadimi, S. Oliver, G. Ozin, J. Garces and M. Olken, *Nature*, 1993, **365**, 239
- ¹⁷ D.M. Bibby and M.P. Dale, *Nature*, **317**, 157
- ¹⁸ H. Qisheng and X. Ruren, *J.Chem. Soc. Chem. Commun.*, 1990, 783
- ¹⁹ Q. Gao, S. Li, and R. Xu, *J. Chem. Soc. Chem. Commun.*, 1994, 1465
- ²⁰ E.R. Cooper, C.D. Andrews, P.S. Wheatly, P. B. Webb, P. Wormald and R. E. Morris, *Nature*, 2004, **430**, 1012
- ²¹ R.D. Rogers and K.R. Seddon, *Science*, 2003, **302**, 792-793
- ²² E. Parnham and R.E. Morris, *J.Am.Chem.Soc.*, 2006, **128**, 2204-2205
- ²³ E. Parnham and R.E. Morris, *Chem.Comm.*, 2006, 380-382
- ²⁴ http://www.parrinst.com/doc_library/members/4700-Sample_Prep_Bulletin.pdf
- ²⁵ C.Baerlocher and W.M. Meier, *Helv.Chim.Acta.*, 1969, **52**, 1853
- ²⁶ R.Francis and D O'Hare, *J.Chem.Soc.Dalton Trans*, 1998, **19**, 3133
- ²⁷ O. Weib, G.Ihelein, F.Schuth, *Micropor. Mesopor. Mat.*, 2000, **35-36**, 617-620
- ²⁸ E. Aubert, F. Porcher, M. Souchassou and C. Lecomte, *Acta Cryst B.*, 2003, **59**, 687-700
- ²⁹ M. Sabater and G. Sastre, *Chem.Mater.*, 2001, **13**, 4520- 4526
- ³⁰ S. L. Burkett and M.E.Davis, *Chem. Mater.*, 1995, **7**, 1453-1463
- ³¹ H. Lee, S. I. Zones and M.E. Davis, *Nature*, 2003, **425**, 385
- ³² H. Lee, S. I. Zones and M.E. Davis, *J. Phys.Chem. B.*, 2005, **109**, 2187-2191
- ³³ J.F. Brennecke and E.J. Maginn, *AIChE J.*, 2001, **47**, 2384-2389

- ³⁴ J.D. Martin, American Chemical Society Symposium Series, 2002, **818**, 413
- ³⁵ P. Wasserscheid and W. Keim, *Angew. Chem. Int. Ed.*, 2000, **39**, 3772-3789
- ³⁶ M.J. Earle and K.R. Seddon, *Pure Appl. Chem.*, 2000, **72**,1391-1398
- ³⁷ B.L. Bhargava, S. Balasubramanian and M. Klein, *Chem. Commun.*, 2008, 3339-3351
- ³⁸ K. Dong, S. Zhang, D. Wang and X. Yao, *J. Phys. Chem. A.*, 2006, **110**, 9775-9782
- ³⁹ E.R. Cooper, C.D. Andrews, P.S. Wheatly, P.B. Webb, P. Wormald and R.E. Morris, *Nature*, 2004, **430**, 1012
- ⁴⁰ L. Cammarata, S.G. Kazarian, P.A. Slater and T. Welton, *Phys. Chem. Chem. Phys.*, 2001,**3**,5192
- ⁴¹ E.R. Parnham and R.E. Morris, *Acc. Chem. Res.*, 2007,**40**,1005
- ⁴² H. Ma, Z. Tian, R. Xu, B. Wang, Y. Wei, L. Wang, Y. Xu, W. Zhang and L. Lin., *J. Am. Chem. Soc.*, 2008, **130**, 8120-8121
- ⁴³ G.W. Phillips, S.N. Falling, S.A. Godleski and J.R. Monnier, Continuous process for the manufacture of 2,5-dihydrofurans from c,d-epoxybutenes, US Pat., 5,315,019 (1994)
- ⁴⁴ http://www.basf.com/corporate/051004_ionic.htm
- ⁴⁵ E. García-Junceda J. García-García, A. Bastida and A. Fernández-Mayoralas, *Bioorg. Med. Chem.*, 2004, **12**, 1817–1834
- ⁴⁶ R. Madeira-Lau, F. V. Rantwijk, K.R. Seddon and R.A. Sheldon. *Org. Lett.*, 2000. **2**, 4189.
- ⁴⁷ V. Pushparaj, M. Shaijumon, A. Kumar, S. Murugesan, L.Ci, R. Vajtai, R. Linhardt, O. Nalamasu, and P. Ajayan, *Proceedings of the National Academy of Sciences*, 2007, **104**, 13574-13577

- ⁴⁸ A. E. Visser, R. P. Swatloski, W. M. Reichert, J. H. Davis Jr., R. D. Rogers, R. Mayton, S. Sheff and A. Wierzbicki, *Chem. Commun.*, 2001, 135
- ⁴⁹ M.E. Bluhm, M.G. Bradley, R. Butterick III, U. Kusari and L.G. Sneddon, *J.AM.Chem.Soc.*, 2006, **128**, 7748-7749
- ⁵⁰ Wasserscheid, P. & Welton, T. *Ionic Liquids in Synthesis* Ch. 2.1.2, 9–12 (Wiley-VCH, Weinheim, Germany, 2003)
- ⁵¹ A.P. Abbott, G. Capper, D.L. Davies R.K. Rasheed and V. Tambyrajah, *Chem. Commun.*, 2003, 70-71
- ⁵² E.M. Flanigen and R.L. Patton, U.S. 4 073 864, 1978
- ⁵³ G. Férey, *J. Fluorine Chem.*, 1995, **72**, 187
- ⁵⁴ L. A. Vilaescusa, P.A. Barrett and M. A. Cambor, *Angew. Chem. Int. Ed.*, 1999, **38**, 1997
- ⁵⁵ M.P. Attfield, C.R.A. Catlow, and A.A. Sokol, *Chem. Mater.*, 13 (12), 4708 -4713, 2001
- ⁵⁶ M. Goepper, and J.L. Guth, *Zeolites*, 1991, **11**, 477.
- ⁵⁷ S. Qui, J. Yu, G. Zhu, O. Terasaki, Y. Nozue, W. Pang, and R. Xu, *Micropor. Mesopor. Mat.*, 1998, **21**, 245-251.
- ⁵⁸ M. Zhang, D. Zhou, J. Li, J. Yu, J. Xu, F. Deng, G. Li and R. Xu, *Inorg.Chem.* 2007, **46**, 136-140
- ⁵⁹http://www.mpimuelheim.mpg.de/kofo/institut/arbeitsbereiche/schmidt/zeolites_ef.htm
- 1
- ⁶⁰ E. Erdem, N.Karapinar and R. Donat, *J. Colloid Interface Sci.*, 2004, **280**, 309

- ⁶¹ S.T. Wilson, and P. Barger, *Micropor. Mesopor. Mat.*, **29**, 1999, 117-126
- ⁶² A. Mahajna, M. Hirsh, and M. M. Krausz, *Eur. Surg. Res.*, 2007, **39**, 251
- ⁶³ M. Davis, *Nature*, 2002, **417**, 813
- ⁶⁴ A. K. Cheetham and C. N. R. Rao, *Science*, 2007, **318**, 58
- ⁶⁵ H. Li, M. Eddaoudi, M. O'Keeffe, and O. M. Yaghi, *Nature*, 1999, **402**, 276-279.
- ⁶⁶ O.M. Yaghi, G. Li, and H. Li, *Nature*, 1995, **378**, 703-706
- ⁶⁷ O.M. Yaghi, H. Li, C. Davis, D. Richardson, and T. L. Groy, *Acc. Chem. Res.*, 1998, **31**, 474-484
- ⁶⁸ G. Férey, C. Mellot-Draznieks, C. Serre, F. Millange, J. Dutour, S. Surble, and I. Margiolakie, *Science*, 2005, **309**, 2040-2042
- ⁶⁹ H.K. Chae, D.Y. Siberio-Prez, J. Kim, Y. Go, M. Eddaoudi, A.J. Matzger, M. O'Keeffe, O.M. Yaghi, *Nature.*, 2004, **427**, 523-527
- ⁷⁰ C. Serre, C. Mellot-Draznieks, S. Surblé, N. Audebrand, Y. Filinchuk and G. Férey, *Science*, 2007, **315**, 18281-1831
- ⁷¹ T. Loiseau, C. Serre, C. Huguenard, G. Fink, F. Taulelle, M. Henry, T. Bataille and G. Férey, *Chem. Eur. J.*, 2004, **10**, 1373-1382
- ⁷² S. Kitagawa and K. Uemura, *Chem. Soc. Rev.*, 2005, **34**, 109-119
- ⁷³ J. Rowsell and O.M. Yaghi, *Microporous and Mesoporous Materials.*, 2004, **73**, 3-14
- ⁷⁴ C. J. Kerpert and M.J. Rosseinsky, *Chem. Commun.*, 1999, 375-376
- ⁷⁵ H. Li, M. Eddaoudi, M. O'Keeffe and O.M. Yaghi, *Nature.*, 1999, **402**, 276-279
- ⁷⁶ K.C. Szeto, K.O. Kongshaug, S. Jakobsen, M. Tilset and K.P. Lillerud, *Dalton Trans.*, 2008, 2054-2060

- ⁷⁷ D.N. Dybtsev, H. Chun and K. Kim, *Chem. Commun.*, 2004, 1594-1595
- ⁷⁸ K. Jin, X. Huang, L. Pang, J. Li A. Appel and S. Wherland, *Chem. Commun.*, 2002, 2872-2873
- ⁷⁹ L. Xu, E. Choi and Y. Kwon, *Inorg. Chem. Commun.*, 2008, **11**, 150-154
- ⁸⁰ Z. Lin, Y. Li, A.M.Z. Slawin and R. E. Morris, *Dalton Trans.*, 2008, 3989-3994
- ⁸¹ Z. Lin, A.M.Z. Slawin and R.E. Morris, *J.Am.Chem.Soc.*, 2007, **129**, 4880-4881
- ⁸² S. Chen, J. Zhang and X. Bu, *Inorg. Chem.*, 2008, **47**, 5567-5569
- ⁸³ L. Shi, X. Wang, C.A. Sandoval, M. Li, Q. Qi, Z. Li and K. Ding, *Angew. Chem. Int. Ed.*, 2006, **45**, 4108-4112
- ⁸⁴ Z. Lin, D.S. Wragg and R.E. Morris, *Chem. Commun.*, 2006, 2021-2023
- ⁸⁵ S.H. Jhung, J. Lee, P. M. Forster, G. Férey, A.K. Cheetham, and J. Chang, *Chem.Eur.J.*, 2006, **12**, 7899-7905
- ⁸⁶ L. Alaerts, C.E. A. Kirschhock, M. Maes, M. A. van der Veen, V. Finsky, A. Delpa, J. A. Martens, G. V. Baron, P. A. Jacobs, J. F. M. Denayer and D. E. De Vos, *Angew. Chem. Int. Ed.*, 2007, **46**, 4293-4297
- ⁸⁷ M. Hirscher and B. Panella, *Journals of alloys and compounds*, 2005, **404-406**, 399-401
- ⁸⁸ B. Xiao, P.S. Wheatley, X. Zhao, A.J. Fleycher, S. Fox, A. G. Rossi, I.L. Megason, S. Bordiga, L. Regli, K. M. Thomas, and R.E. Morris, *J. Am. Chem. Soc.*, 2007, **129**, 1203-1209
- ⁸⁹ D. J. Collins and H. Zhou, *J. Mater.Chem.*, 2007, **17**, 3154-3160
- ⁹⁰ <http://www1.eere.energy.gov/hydrogenandfuelcells/mypp/pdfs/storage.pdf>

- ⁹¹ A. R. Millward and O.M. Yaghi, *J. Am. Chem. Soc.*, 2005, **127**, 17998-17999
- ⁹² M.R. Miller and I.L. Megson, *Br. J. Pharmacol.*, 2007, **31**, 624-631
- ⁹³ S.S. Y. Chui, S. M. F. Lo, J. P.H. Charmant, A.G. Orpen, and I.D. Williams, *Science.*, 1999, **283**, 1148-1150
- ⁹⁴ G. Alberti, U. Costantino, S. Allulli and N. Tomassini, *J. Inorg. Nucl. Chem.*, 1978, **40**, 1113.
- ⁹⁵ Y.F. Yang, Y.S. Ma, S.S. Bao, L.M. Zheng, *Dalton Transactions*, 2007, 4222-4226
- ⁹⁶ G. B. Hix, A. Turne, B. M. Kariuki, M. Tremayne and E. J. Maclean, *J. Mater. Chem.*, 2002, **12**, 3220-3227.
- ⁹⁷ M.M. Gómez-Alcantara, M.A.G. Aranda, P. Olivera-Pastor, P. Beran, J.L. García-Muñoz and A. Cabeza, *Dalton Trans.*, 2006, 577-585
- ⁹⁸ D. Cao, S. Gao and L. Zheng, *J. Solid State Chem.*, 2004, **177**, 2311-2315
- ⁹⁹ V. Chandrasekhar, S. Kingsley, B. Rhatigan, M.K. Lam and A.L. Rheingold, *Inorg. Chem.*, 2002, **41**, 1030-1032.
- ¹⁰⁰ M. Mehring and M. Schürmann, *Chem. Commun.*, 2001, 2354-2355
- ¹⁰¹ V. Chandrasekhar, L. Nagarajan, R. Clérac, S. Ghosh and S. Verma, *Inorg. Chem.*, 2008, **47**, 1067-1073.
- ¹⁰² C. R. Samanamu, M.M. Olmstead, J. Montchamp and A. F. Richards, *Inorg. Chem.*, 2008, 3879
- ¹⁰³ S. Konar and A. Clearfield, *Inorg. Chem.*, 2008, **47**, 3489-3491
- ¹⁰⁴ M. Gómez-Alcántara, A. Cabeza, K. Moreno-Real, M.A.G. Aranda, and A. Clearfield, *Microporous and Mesoporous Materials.*, 2006, **88**, 293-303

- ¹⁰⁵ B. Yang, A. V. Prosvirin, H. Zhao, and J. Mao, *J. Solid State Chem*, 2006, **179**, 175-185
- ¹⁰⁶ J. Yang, J. Ma, G. Zheng, L. Li, F. Li, Y. Zhang and J. Liu, *J. Solid State Chem.*, 2003, **174**, 116-124
- ¹⁰⁷ A. Cabeza, M. Gómez-Alcántara, P. Olivera-Pastor, I. Sobrados, J. Sanz, B. Xiao, R.E. Morris, A. Clearfield and M.A. G. Aranda, *Microporous and Mesoporous Materials.*, 2008, **114**, 322-336
- ¹⁰⁸ G. Alberti, M. Casciola, U. Costantino and R. Vivani, *Adv. Mater.*, 1996, **8**, 291-303
- ¹⁰⁹ S. Drumel, P. Janvier, D. Deniaud and B. Bujoli, *J.Chem.Soc., Chem. Commun.*, 1995, 1051
- ¹¹⁰ J.L. Bideau, C. Payen, P. Palvadeau, and B. Bujoli, *Inorg. Chem.*, 1994, **33**, 4885-4890.
- ¹¹¹ K. Maeda, Y. Kiyozumi, Mizukami F., *Angew.Chem. Int. Ed. Engl*, 1994, **33**, 2335
- ¹¹² K. Maeda., J. Akimoto, Y. Kiyozumi, F. Mizukami, *Angew.Chem. Int. Ed. Engl*, 1995, **34**, 1199
- ¹¹³ J. A. Groves, S. R. Miller, S. J. Warrender, C. Mellot-Draznieks, P. Lightfoot, P. A. Wright, *Chem Commun*, 2006, **31**, 3305
- ¹¹⁴ C. Serre, J.A.Groves, P. Lightfoot, A.M.Z. Slawin P.A. Wright, N. Stock, T. Bein, M. Haouas, F. Taulelle and G. Férey, *Chem. Mater.*, 2006, **18**, 1451-1457
- ¹¹⁵ K. Maeda, Y. Kiyozumi and F. Mizukami, *J. Phys. Chem. B.*, 1997, **101**, 4402
- ¹¹⁶ F. Fredoueil, M. Evian, M. Bujoli-Doeuff, and B. Bujoli, *Eur. J. Inorg. Chem.*, 1999, 1077

¹¹⁷ M. Jaber, O. Larlus and J. Míche-Brendlé, *Solid State Sci.*, 2007, **9**, 144-148

¹¹⁸ H.E. Katz, G. Scheller, T.M. Putvinski, M. L. Schilling, W.L. Wilson, C.E.D. Chidsey, *Science.*, 1991, **254**, 1485.

¹¹⁹ J. Wu, Y. Song, E. Zhang, H. Hou, Y. Fan, and Y. Zhu, *Chem. Eur.J.*, 2006, **12**, 5823-5831

¹²⁰ B. Zhang and A. Clearfield., *J.Am.Chem.Soc*, 1997, **119**, 2751-2752

2 Aims of this Project

The overall aim of this thesis was to obtain a greater understanding of ionothermally prepared materials using complementary techniques. Charge matching and mismatching has a great impact in zeotype synthesis and it is important to understand how subtle changes can influence framework crystallisation, as such a key objective of this thesis was to try and examine the materials using high resolution X-ray diffraction at the Synchrotron Radiation Source (SRS), in order to gain more information regarding the charge density of the ionic liquids and the resultant ionothermally prepared solids. High resolution NMR techniques will also be used to investigate the quality of different X-ray diffraction datasets one at “high” resolution and one at “normal” resolution.

The first objective was to examine porous materials using single crystal X-ray diffraction to determine which structures would be suitable for high resolution studies. Firstly this involved the synthesis of known materials as described by Cooper *et al*¹ and further utilising these techniques in the synthesis of novel materials.

A key feature of the ionothermal method is the reduction of reagents present in the synthesis, making it easier to examine the reaction process *in-situ*. A high energy dispersive beam-line (Station 16.4) will be used to investigate the difference of microwave over conventional heating methods as it has been shown that microwave heating provides larger purer crystals over conventional heating methods² in ionothermally prepared materials.

Much of this work is aimed at understanding the fundamental principles of highly porous materials to try and get a greater insight into how and why they crystallise the way they do but also to understand how they can be improved for applications. A gas cell will be used to investigate how various gases bind to framework materials.

2.1 References

¹ E.R. Cooper, C.D. Andrews, P.S. Wheatley, P.B. Webb, P. Wormald and R.E. Morris, *Nature.*, 2004, **430**, 1012

² Z. Lin, D. S. Wragg and R. E. Morris, *Chem. Commun.*, 2006, 2021-2023

3 Experimental

3.1 X-ray Diffraction

X-ray diffraction is perhaps the only technique which can provide 3D structural information, fingerprinting and both inter and intra molecular distances. Since its conception it has rapidly become a very useful technique employed by chemists in structure characterisation.

Objects are seen by the interference of light waves upon an object through the recombination of that light with our eyes. The information obtained through this process is mathematically known as a Fourier Transform (F.T.). Using this knowledge crystallographers have been able to devise a way to view images of molecules which do not use conventional light waves but other types of radiation like X-rays. X-rays are useful as they have very short wavelengths (10^{-8} to 10^{-12} metres) enabling them to penetrate deep inside materials and provide a more detailed image of the structure, this is because the wavelength is of similar length to that of the bonds.

Our eyes cannot detect X-rays. However a diffraction pattern can be collected on a detector or using photographic paper which is sensitive to X-rays. Unfortunately we cannot directly recombine the experimental data into a structural image, because an important piece of information, the phases cannot be measured experimentally. This is known as the phase problem. However this can be overcome in a number of ways and once it is solved a Fourier Transform can be used to recombine the X-rays obtained from the interactions with the electrons to provide an image of the electron density in a structure.

A perfect crystalline solid is made up of a large number of identical molecules which are arranged in a regular way to give a highly ordered structure. When X-rays hit a crystal lattice they are diffracted and there is interference between the diffracted beams. This is described by Bragg's law (3.1) which is probably the most important concept in diffraction as it gives the geometrical conditions whereby a diffracted beam can be observed. X-rays are scattered by electrons in the atoms of the crystal, the interference is used in determining the structure of the crystal. Bragg's law aids in determining the d spacings between the layers of atoms using X-ray diffraction and can easily be derived by considering the conditions necessary to make the phases of the beams coincide leading to constructive interference and ultimately diffraction peaks.

In practice the rays of the incident beam are in phase and parallel up to the point at which the top beam strikes the top layer at atom *z* (*Figure 3.1*). The second beam continues to the next layer where it is scattered by atom B. The second beam must travel the extra distance $AB + BC = 2d\sin\theta$ if the two beams are to continue travelling adjacent and parallel. This extra distance must be an integral (*n*) multiple of the wavelength (λ) for the phases of the two beams to be the same resulting in Bragg's law for constructive interference.

$$n\lambda = 2d \sin \theta \quad (3.1)$$

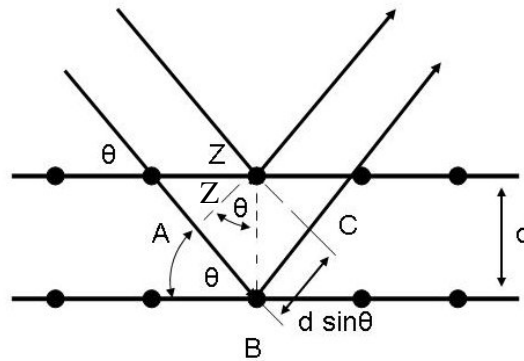


Figure 3.1: Deriving Bragg's Law

When the X-rays penetrate deep into the crystal the lattice planes diffract the X-rays producing constructive interference if Bragg's equation is satisfied and destructive interference if not. This occurs as long as the beams are separated by a whole number of wavelengths otherwise no diffraction will be observed.

The planes are described by Miller planes and are represented by three integers (hkl).

Figure 3.2 represents the (110) and (010) plane.

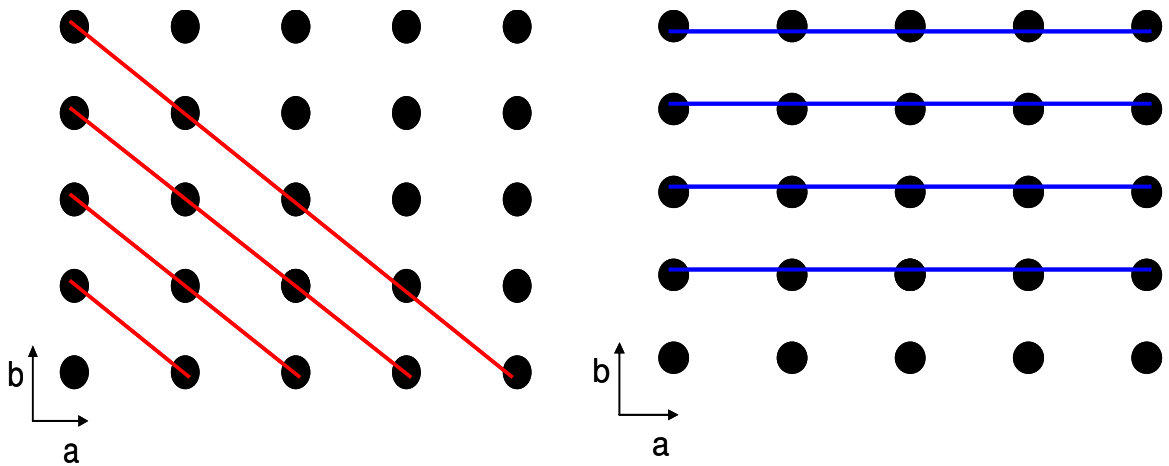


Figure 3.2: Miller plane (110) (red line) the plane intercepts the unit cell along the a and b axis once whilst never intercepting the c axis. Miller plane (010) (blue line) the b axis is intercepted once and neither the c nor a axis are ever intercepted represented by the (010) miller plane.

The diffraction pattern is the Fourier transform (equation 3.2) of the electron density and when applied can be thought of as the mathematical equivalent of a lens. The information obtained can be used to recombine the X-rays to provide an image of the structure.

$$F_{(hkl)} = \sum_{j=1}^N f_j \exp 2\pi i (hx_j + ky_j + lz_j) \quad (3.2)$$

Every reflection collected is a wave and as such has amplitude which is measurable and a phase which is not. The atomic scattering factor f_j for the j th atom has the atomic coordinates x_j, y_j, z_j . The integers h, k, l are the Miller indices for one particular reflection and thus the equation shows how the structure factor F for that reflection relates to the crystal structure with N atoms. The equation is applied to every reflection and produces a set of structure factors each with an amplitude $|F(hkl)|$ which is known and a phase $\Phi(hkl)$ which is unknown but can be determined.

Another important concept is the use of the reverse Fourier transform (equation 3.3) whereby the crystal structure can be expressed in terms of electron density.

$$\rho(xyz) = \frac{1}{V} \sum_{h,k,l} |F(hkl)| \cdot \exp[i\phi(hkl)] \cdot \exp[-2\pi i(hx + ky + lz)] \quad (3.3)$$

This equation is very similar to that of the forward Fourier transform with the main difference being the inclusion of a unit cell volume ($1/V$) which is necessary to produce the correct units for electron density (electrons per \AA^3 or $e \text{\AA}^{-3}$) and the presence of the negative sign (-2π). This equation shows that if the structure factor amplitudes $F(hkl)$

and the phases for all the hkl reflections can be measured it is possible to determine the electron density at every point (xyz) in the unit cell.

The reverse Fourier transform contains both amplitudes ($|F_{hkl}|$) and calculated phases (Φ), the amplitudes have been recorded from the diffraction data. However, the phases are not known and therefore it is not possible to obtain the correct Fourier transform, which leads us to the phase problem and the need for a solution. The Patterson synthesis and direct methods are the two most common and widely used ways to solve the phase problem.

The Patterson synthesis is most useful when there are a few or one heavy atom and works by replacing the amplitudes $|F_{hkl}|$ (from equation 3.3) with their squares $|F_0|^2$ with the phases all set to zero to produce equation 3.4.

$$\rho(uvw) = \frac{1}{V} \sum_{h,k,l} |F(hkl)|^2 \cos[2\pi(hu + kv + lw)] \quad (3.4)$$

With the omission of the phases the above (3.4) is no longer the desired electron density, but instead produces a Patterson map, similar to the electron density in that peaks are positive, however they are not the atomic positions but the vectors between pairs of atoms in the structure. For every pair of atoms in the structure with coordinates (x_1, y_1, z_1) and (x_2, y_2, z_2) there will be a peak in the Patterson map at the positions $(x_1 - x_2, y_1 - y_2, z_1 - z_2)$ and also one at the position $(x_2 - x_1, y_2 - y_1, z_2 - z_1)$ each atom giving a vector to the other with $(0,0,0)$ being the origin of the unit cell in the Patterson map indicating where the atoms lie relative to each other.

Direct methods is probably the most widely used technique by crystallographers for solving the phase problem. It relies on the fact that the amplitude and the phase of a structure factor are related through electron density. This technique is dependent on the fact that the correct set of phases must produce an electron density that is positive (as it is impossible to get a negative electron density). We know the amplitudes and by placing a series of constraints on the electron density the phases can be determined. Atoms occur at discrete points and as such should give peaks of electron density which help to reveal the position of atoms.

Once the phase problem has been solved it is possible to obtain an electron density from which a structure solution is now obtainable.

3.2 Least Squares refinement

Once a suitable starting model has been calculated a least squares refinement is required to refine the model. This is done to ensure as close a match as possible between the observed and the calculated diffraction patterns.

As it is not possible to directly obtain the phases from the diffraction pattern, the observed $|F_o|$ and calculated $|F_c|$ amplitudes are used to compare the predicted model with the actual model provided by the experiment. Least squares analysis is used to obtain the “best fit”.

If the equation of a straight line is

$$y = mx + c \quad (3.5)$$

The parameters are the slope, m , the intercept, c and the experimental values x_i, y_i

Then the observational equation is

$$mx_i + c = y_i \quad (3.6)$$

However there are no values for m and c and so we look for the “best fit” line

The residual of the observed equation is

$$\mathcal{E}_i = y_i - mx_i - c \quad (3.7)$$

Which we can represent in a matrix

$$\begin{pmatrix} x_1 & 1 \\ x_2 & 1 \\ \dots & \dots \\ x_n & 1 \end{pmatrix} \begin{pmatrix} m \\ c \end{pmatrix} = \begin{pmatrix} y_1 \\ y_2 \\ \dots \\ y_n \end{pmatrix} \quad (3.8)$$

Which can be represented as the design matrix

$$Ax = b \quad (3.9)$$

Where A is the left hand side matrix containing the x values, X is the vector of unknowns m and c whilst b is the right hand side vector containing the y values.

The least squares solution is found by multiplying both sides by the transpose of A and solving the resulting equations for x . These are known as the normal equations of least squares.

$$\left(A^T A \right) x = A^T b \quad (3.10)$$

This calculation is repeated many times until there is no significant change. The observational equations can also be given weights ω_i according to their reliability which is used to ensure the equation of the line fits more precisely. As there are often many variables in a crystal structure it is advisable that an approximate solution is known before least squares refinement is used.

Many different types of refinements can be performed on a structure to improve its fit between the observed and calculated data which include the atomic coordinates (x,y,z) for each atom, atomic displacement parameters (ADP's) i.e. anisotropic or isotropic models, the scale factor and the site occupancy

3.3 Quality of data

So how do we know that our structure is what we say it is?

This can be done by looking at the residual density (R factors), where a low R factor indicates a sensible X-ray model. Once a model has been solved and refined the calculated and observed diffraction patterns can be compared to confirm if there is agreement. There are two R factors of interest with one un-weighted (3.11) which compares the amplitudes of the observed and calculated reflections and a weighted factor (3.12).

The most widely used indicator is the residual factor R which is shown in equation 3.11. Where the discrepancies of the observed structure factor (F_o) against the calculated structure factor (F_c) are calculated.

$$R = \frac{\sum || F_o | - | F_c ||}{\sum | F_o |} \quad (3.11)$$

There are variations on this equation (3.12) such as a weighted R factor (wR^2), where F^2 is used instead of $|F|$ this is done to incorporate the reliability of the data.

$$wR^2 = \frac{\sum w(F_o^2 - F_c^2)^2}{\sum w(F_o^2)^2} \quad (3.12)$$

The goodness of fit (goof) is defined in equation 3.13 for N data and refined parameters (P) and is another measure used to check the quality of data. It is a very good measure of how good a fit the least squares refinement has been.

$$S = \sqrt{\frac{\sum w(F_o^2 - F_c^2)^2}{(N - P)}} \quad (3.13)$$

With the refined structural model (atomic positions, ADPs, bond lengths and angles etc.) there is a standard uncertainty or estimated standard deviation (ESD) and this is the best estimate of the variation we would expect for a refined parameter. They are measured

using equation 3.14 where A^{-1} represents the diagonal elements of the inverse least squares matrix where p_j is the j^{th} of the P parameters and Δ_i represents the difference in the observed and calculated structure factors. The standard uncertainties help to give us an indication of the quality of data, whereby a large ESD indicates a poor refinement.

$$\sigma(p_j) = \left((A^{-1})_{jj} \frac{\sum_{i=1}^N w_i \Delta_i^2}{N - P} \right)^{1/2} \quad (3.14)$$

3.4 Crystallography

A crystal is made up of an infinite number of identical molecules arranged in a regular array in all directions. This regular arrangement is the simplest form of symmetry (translational) and is possessed by all crystalline solids. A crystalline solid can be described using the contents of the repeat unit (unit cell, *Figure 3.3*) and by the translational symmetry defined by the lattice. The lattice is an array of imaginary points such that each point has an identical environment to the next one, we can choose an arbitrary position to be a lattice point however there are conventions used by crystallographers to ensure consistency and that the unit cells show the full symmetry of the lattice. A unit cell is composed of three unique axis (a, b, c) and three angles (α , β , γ) with α lying between the b and c axes, β lying between the a and c axis and γ lying

between a and b axis. The cell can have varying lengths of a, b and c and angles however it is only possible to divide them into 7 crystal systems (*Table 3.1*)

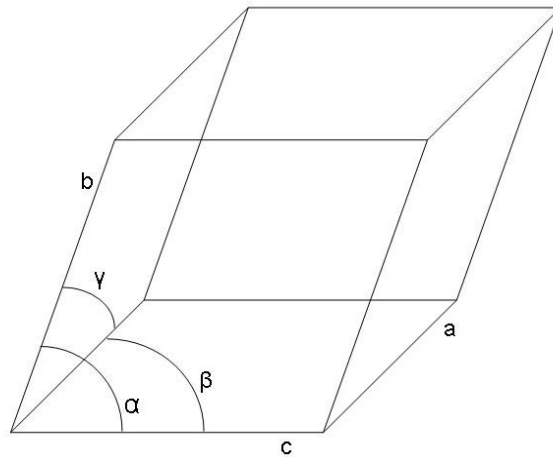
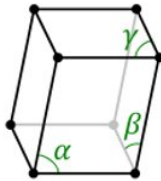
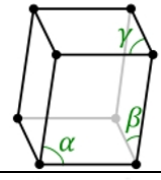
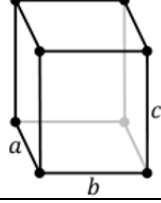
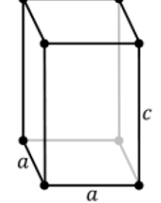
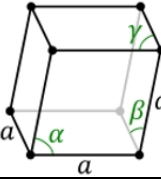
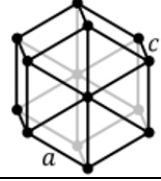
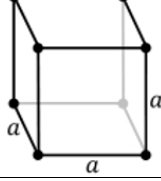


Figure 3.3: A unit cell has 3 unique axis (a,b,c) and 3 angles (α , β , γ) with α lying between the b and c axes, β lying between the a and c axis and γ lying between a and b axis.

Table 3.1: The 7 crystal systems

Triclinic	$\alpha \neq \beta \neq \gamma$	$a \neq b \neq c$	
Monoclinic	$\alpha, \beta \neq 90, \gamma = 90$	$a \neq b \neq c$	
Orthorhombic	$\alpha, \beta, \gamma = 90$	$a \neq b \neq c$	
Tetragonal	$\alpha, \beta = 90, \gamma$	$a = b \neq c$	
Rhombohedral	$\alpha, \beta, \gamma, \neq 90$	$a = b = c$	
Hexagonal	$\alpha, \beta = 90, \gamma = 120$	$a = b \neq c$	
Cubic	$\alpha, \beta, \gamma = 90$	$a = b = c$	

All crystal structures have translational symmetry. However if other symmetry is present it can be used to relate atoms and molecules relative to each other within a cell and as a result the independent part of the structure is only a fraction of the unit cell and is known as the asymmetric unit. The seven crystal systems can be expanded into fourteen Bravais lattices which include the seven crystal systems plus additional centring such as face (F) and body centring (I) upon which the unit cell can be considered to be arranged. From these Bravais lattices it is possible to create space groups with the use of point and translational symmetry, helping to identify the distinct ways of arranging identical objects.

Simple point group symmetry is familiar to chemists (mirror planes and rotation axes). However, crystal symmetry can also include a rotation or a reflection combined with translation to give screw axis and glide planes respectively. A screw axis is the combination of a rotation along with a translation in the direction of an axis, whilst a glide plane involves a reflection in a plane with a displacement of exactly half a repeat unit. The symmetry operators in these crystal systems can only be put together in a limited number of ways (230) and these combinations are known as space groups. They are described using a Hermann-Mauguin symbol¹ such as $P2_1/c$ which shows the centering and symmetry operators. Space groups are a mathematical description of the symmetry of the structure and define the orientations available within the crystal and are fully described in the International Tables for Crystallographers².

Applying the symmetry operators of the space group to the atomic coordinates from the asymmetric unit produces the atomic positions in the unit cell, which can be translated

by an integer number of unit cell distances to produce the overall structure of the material.

3.5 Single Crystal X-ray Diffraction

Single crystal X-ray diffraction is an extremely useful tool in structure characterisation, whereby the property of diffraction is used to examine single crystals with a view to understanding their chemical makeup. This process requires the growth of a single crystal of suitable size, which is especially difficult in zeolite syntheses which are notoriously difficult to grow, and tend to crystallise as very small crystallites or powders. However as technology improves it is becoming easier to obtain crystal structures from these fascinating materials. The crystals used for diffraction vary in size but are in the order of 0.05 x 0.05 x 0.05 mm.

Even with the technology available it is important to choose a suitable crystal, as a small sample will diffract too weakly and therefore will be too difficult to measure, however too large and the crystal absorbs the X-rays which can lead to systematic errors.

3.6 Selecting a Crystal

An optical microscope is extremely important in crystal selection as it can be used to identify unsuitable crystals and therefore save a lot of time on the diffractometer.

Firstly the crystals are examined by shape and any deformed crystals are discarded. A polarising filter can be inserted to examine the remainder, as most crystals with a few exceptions will transmit polarised light. If a suitable crystal has been located the microscope turntable is then rotated and the crystal should turn dark and then light again

every 90° depending on the crystal symmetry. This is called extinction and is a good indicator of the quality of the crystal. If the crystal extinguishes completely it is usually a single crystal; a crystal which does not extinguish completely is not single and should be rejected. *Figure 3.4* shows a crystal extinguishing when a polarising filter is rotated by 90° .



Figure 3.4: A crystal as viewed under a microscope fitted with a polarising filter. The crystal extinguishes when the filter is rotated by 90° . Small amounts of powdered sample are visible on the crystal surface which are removed before exposing to X-rays.

Once a single crystal has been selected from the sample it is then exposed to X-rays. These can be produced from different sources such as an X-ray tube, rotating anode or synchrotron.

3.7 X-ray Tubes

An X-ray tube consists of a cathode which emits electrons by passing an electrical current through a wire filament accelerated with an electrical potential over a short distance through a vacuum and then stopped by a water cooled metal block (anode). As

the electrons decelerate and enter the metal they produce radiation and a continuous range of wavelengths (*Figure 3.5*). There are a few high intensity sharp peaks which arise from the interaction of the incoming electrons with the electrons in the inner shells of the atoms. A collision expels an electron and an electron of higher energy drops into the vacancy emitting energy as an X-ray photon. The most widely used metal targets are molybdenum and copper which emit X-rays at wavelengths of 0.71073 and 1.54184 Å respectively.

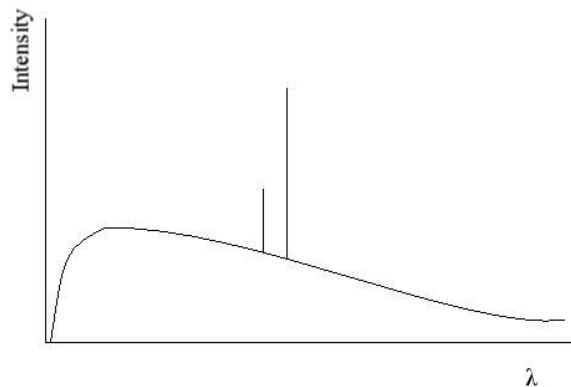


Figure 3.5: Spectrum of X-rays from an X-ray tube. The two peaks on the graph are $K\alpha_1$ and $K\alpha_2$

3.8 Rotating Anode

X-ray production in conventional X-ray tubes is not very efficient due to the need to dissipate heat from the focal spot. A solution to this has been to rotate the anode and so spread the heat load over a larger area thus increasing the power rating which can be as strong or stronger than some 2nd generation synchrotron sources.

Figure 3.6 is a schematic of a rotating anode X-ray tube. The rotating anode (A) is spun at high speed, the cathode (C) focuses a stream of electrons which are accelerated by a high potential difference between the target disc (T) and the cathode. When the electrons hit the disc X-rays are produced and passed through the X-ray window (W).

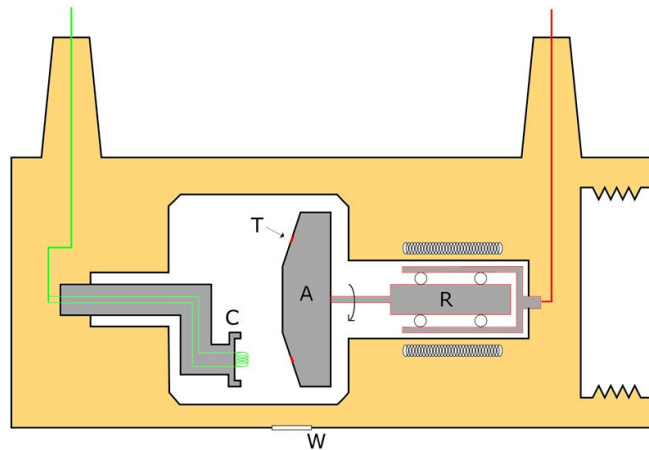


Figure 3.6: Schematic of a rotating anode X-ray³ source C is the cathode, A anode, R rotor, T Anode target W tube window

3.9 Synchrotron Radiation

Synchrotron radiation is highly intense polarized light and can be delivered as a series of short pulses of less than a nanosecond. An electron gun is used to produce a stream of electrons which are then fed into a linear accelerator (linac) and accelerated to extremely high speeds (relativistic). The electrons are passed into a booster ring where radio waves are used to maintain the high speeds, the booster ring then feeds to the storage ring which is kept under vacuum so that no air particles can deflect the electrons (beam).

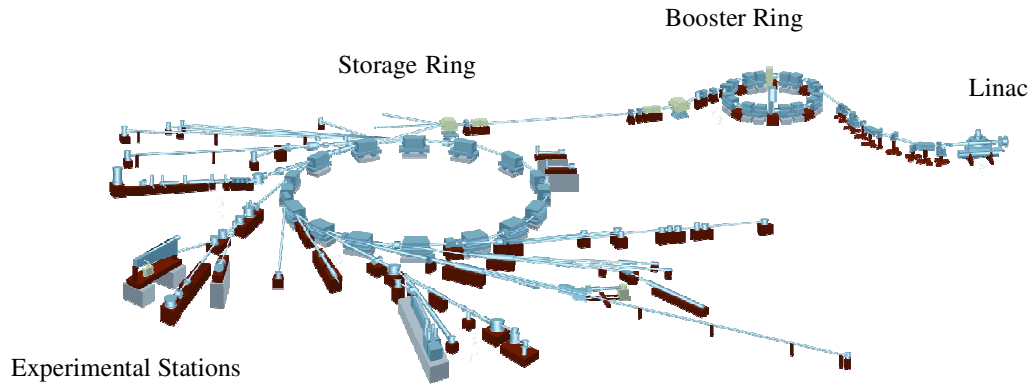


Figure 3.7: SRS, Daresbury second generation synchrotron source booster and linac lie outside the storage ring.

Once inside the storage ring the beam's brightness can be enhanced by the use of insertion devices such as undulators and wigglers. These devices consist of a number of magnets in various positions to cause deviation of the electrons whilst keeping the trajectory fixed and result in a shift in wavelength which leads to an increase in brightness.

When the path of the electrons is bent (usually at a bending magnet), synchrotron light is produced, the radiation is given off tangentially to the storage ring to the various beam lines circulating the ring. The radiation emitted has a continuous spectrum ranging from infra-red to X-rays which can be selected by using a monochromator for different types of experiment.

SRS Beamcurrent 17/09/07-18/09/07

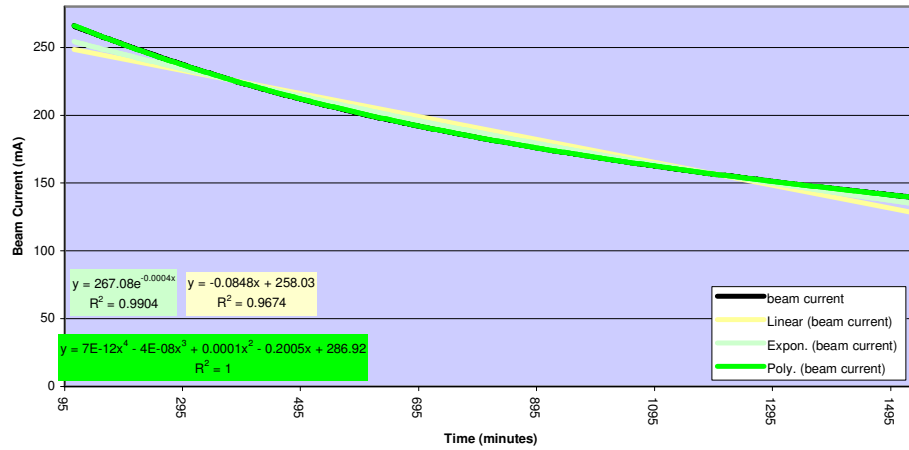


Figure 3.8: Graph showing how the beam current decays with time at the SRS.

The electron current in the storage ring decays exponentially (Figure 3.8) and needs to be refilled approximately every 24 hours. A third generation synchrotron such as Diamond is able to run in a continuous top-up mode, the booster and linac are stored within the confines of the storage ring making it easier to add more electrons when necessary so that a continuous steady ring current can be achieved.

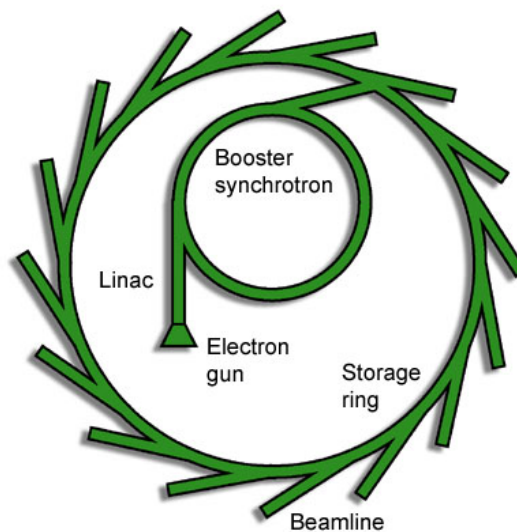


Figure 3.9: Schematic of the third generation Diamond Synchrotron⁴ Oxfordshire linac and booster lie inside the storage ring.

There are a few advantages to using synchrotron radiation compared to the X-rays produced on in-house facilities. They can provide more intense X-rays with low divergence making them suitable for examining small crystals typical in zeolite synthesis. The radiation is tuneable, different wavelengths can be chosen so that they can penetrate the crystal more deeply. Faster data collection times can be achieved due to the intense X-ray beam.

There are, however, some disadvantages to synchrotrons. Firstly they are expensive to maintain and tend to be run as a national facility. Not many countries can afford them due to the high costs involved and as such there can be long distances to reach a facility. They tend to be heavily over-subscribed and applications usually have to be submitted many weeks/months before an experiment.

3.10 Crystal structure determination

Once a suitable X-ray source has been selected it is time to try and determine the crystal structure. There are many stages to solving a crystal structure; *Figure 3.10* shows a schematic view of the process.

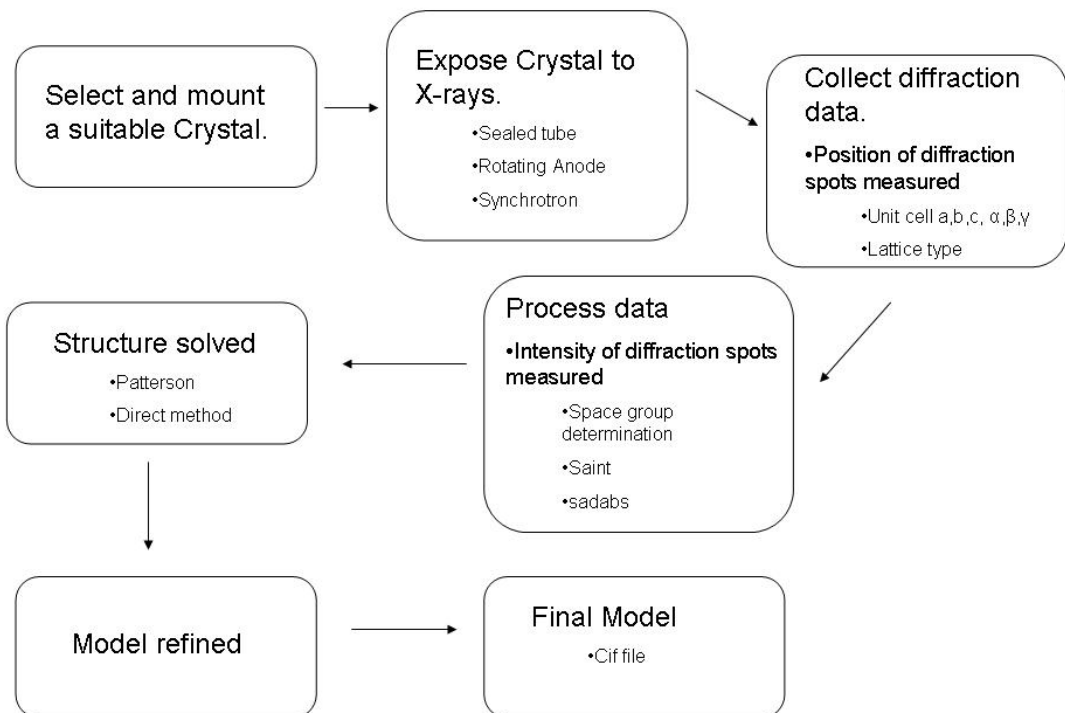


Figure 3.10: The process of structure determination

3.11 Exposing the Crystal to X-rays

Once a crystal has been selected it is mounted on a multistage fibre (comprising of a thin glass or carbon filament mounted to a 0.1mm borosilicate capillary) using an inert oil which vitrifies at low temperatures to encapsulate and therefore protect the crystal. The

fibre is used to reduce scatter. This is then mounted on a goniometer head (*Figure 3.11*) which allows the crystal to be translated in 3 dimensions (x, y and z) so that the crystal can be centred in the middle of the X-ray beam.

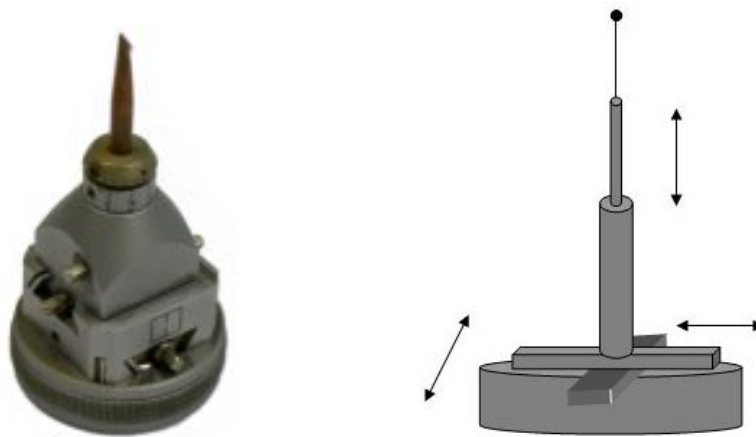


Figure 3.11: A goniometer which allows translational movement to ensure the crystal is centred in the X-ray beam at all times

The crystal is then aligned on the diffractometer and an initial exposure (*Figure 3.12*) taken to determine the crystal quality and scattering capabilities. This allows the crystallographer to gauge if the sample is worth continuing with.



Figure 3.12: A typical diffraction pattern showing intense and single spots indicative of a very crystalline material.

3.12 Processing data

If a suitable scattering crystal has been found an orientation matrix is collected which contains both the unit cell and the relation to the diffractometer. A preliminary indexing of the crystal is also carried out at this stage which provides information on the unit cell of the crystal and is used to compare it to the many hundreds of thousands of data sets on the chemical structural database⁵ (CSD).

If the crystal has been found to be of interest and of sufficient quality a full data set can be obtained. This is done by running a longer scan typically 45-90 minutes on a

synchrotron. However, this is dependent on the quality of the crystal, the space group and the resolution of data required.

A completed dataset is integrated using the unit cell parameters obtained from the matrix to obtain the intensities of diffraction spots. The intensity of the synchrotron radiation decays with time however the sample also can decay and this is corrected for using SADABS which also is used for adsorption corrections and scaling.

A typical full sphere experiment strategy from station 9.8 (SRS) is shown in the table 1 below, the run lasts 1 hour and 10 minutes.

Table 3.2: Full sphere data strategy, used for standard small molecule crystallography at the SRS. Operation is the type of scans that will be collected, distance is the distance between the crystal and the detector, 2theta, Omega, Phi and Chi are angles on the diffractometer, direction is the movement of the diffractometer.

Operation	Active	Distance dx(mm)	2Theta(deg)	Omega(deg)	Phi(deg)	Chi(deg)	Time(sec)	Width(deg)	Sweep(deg)	Direction
Omega Scan	Yes	55	-30	-30	0	54.74	1	0.36	180	negative
Omega Scan	Yes	55	-30	-30	120	54.74	1	0.36	180	negative
Omega Scan	Yes	55	-30	-30	240	54.74	1	0.36	180	negative

The diffractometer on station 9.8 utilises a 3-circle design (*Figure 3.13*) comprising of 4 motors in the form of 3 rotations and one linear drive. Theta, Omega and phi motors are rotation drives with theta and omega on the same plane centred around the centre of rotation of the diffractometer whilst phi is based on a different rotation plane. The linear drive distance also known as dx is the distance from the sample to the detector. On a 3-circle machine the chi position is locked at the magic angle of 54.74°.

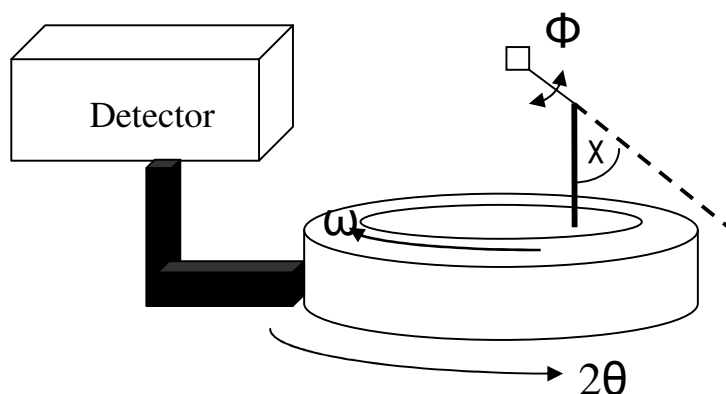


Figure 3.13: Schematic of a three circle diffractometer as used on station 9.8 at the SRS

Table 3.2 is a full sphere strategy and uses an omega scan which can be considered as a sample rotation circle. Omega starts at position X (-30°), drives by a sweep Y (180°) in increments of Z (0.36° width) with phi set at 0° this produces 500 frames of data per run $Y/X =$ number of frames.

Phi is then rotated to 120° and 240° where by the same run is performed so that a full sphere of data can be collected in reciprocal space. Time is measured in seconds and is the length of period the motors are driven and the shutter opened before moving to the next position however there is a dead time of approx 1.25 seconds where the detector resets for the next image and the motor corrections take place and this is why table 1 required 1 hour 10 minutes for a full data collection.

3.13 Structure solution

Once the structure has been correctly assigned its parameters and space group, the structure is then solved using the Patterson or direct methods typically using the

SHELXS⁶ program however other programs such as the SIR packages are available and can be useful in structure solution which utilise direct methods.

3.14 Final model

After a suitable structure solution the model is refined using the method of least squares where by residual peaks are assigned to appropriate atomic positions, hydrogen atoms can be added and a weighting scheme applied, this is done until a suitable residual factor and structure model is obtained.

Once a final model has been established a crystallographic information file (cif) is created. This provides a flexible way to archive the information from the structure, the experimental parameters and other useful information and can be stored on databases such as the inorganic crystal structure database (ICSD)⁷ for reference.

3.15 Station 9.8

Single crystal X-ray diffraction was performed on station 9.8, a high flux single crystal facility at the Synchrotron radiation source (SRS) Daresbury Laboratory, Cheshire. The station uses a Bruker-Nonius APEXII CCD area detector and D8 diffractometer. The X-ray wavelength in this station is tuneable between 1.5 Å and 0.2957 Å. The station is 10.7 m from the 5T wiggler, and can receive up to 3.8 mrad of beam which can be focused horizontally and vertically. The horizontal focusing is provided by a triangular bent Silicon (111) or (220) monochromators, which are cooled by a water cooled GaInSn eutectic alloy. The monochromator crystal has an asymmetric cut of 2.01°, which gives an optimum focus at the sample for a wavelength of ~0.7 Å. The second

optical component is a flat 1.2m palladium coated (300 nm) zerodur glass mirror. This is mounted to allow it to be cylindrically bent to provide vertical focussing of the monochromatic beam. Its second purpose is to act as a harmonic rejecter.

The monochromator is mounted on a Huber rotatory table and can be positioned to a precision of 0.001° . The X-ray wavelength is usually set to approximately 0.68 \AA however for high resolution charge density studies the wavelength is fixed to that near to the silver edge (0.4859 \AA).

The station is fitted with an Oxford Cryosystems Cobra⁺ usually operating in the temperature range of 80-500K however for high resolution charge density studies an Oxford Cryosystems nHelix fitted with helium can be used in order to reach temperatures of 23K-300K.

Figure 3.14 shows a typical set up of the diffractometer with the goniometer, cryostream (nHelix) and the charged coupled device (CCD) area detector. CCD detectors are now used routinely in most single crystal laboratories as they have a fast data collection rate and can provide a higher redundancy of symmetry equivalent reflections. They work by electrons hitting a fluorescent phosphor screen which produce photons of light the light photons interact with the CCD to produce electron-hole pairs, the electrons are then trapped in potential wells which can then be read out as a current. These relatively new detectors have brought many benefits to the world of crystallography such as faster data collections, simultaneous recording of many reflections and better data from poor scattering crystals.

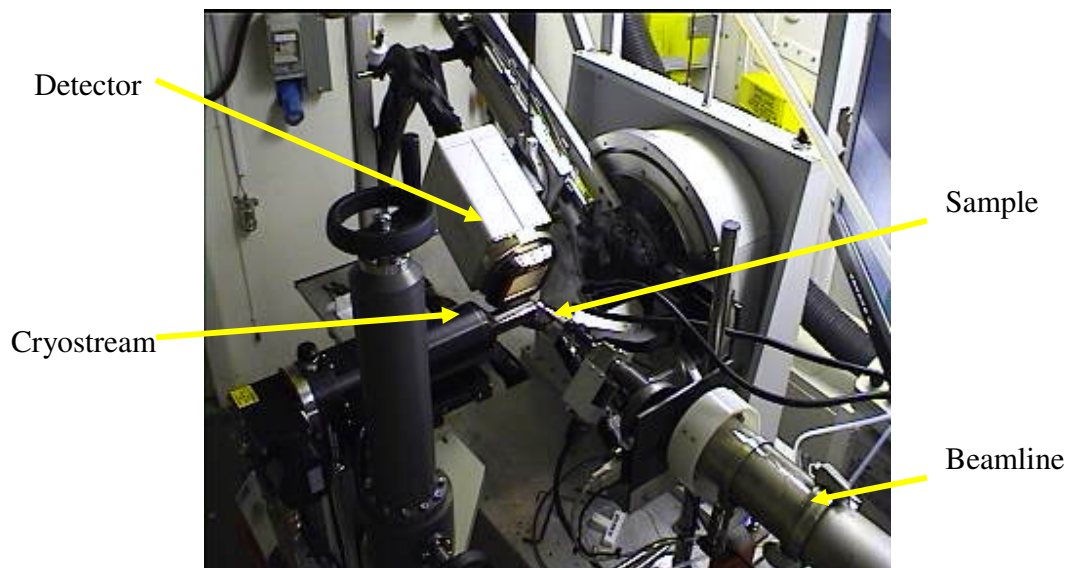


Figure 3.14: Station 9.8 set-up, the diffractometer is on its side in comparison to a standard lab source due to the polarisation characteristic of a synchrotron.

The diffractometer used on stations 9.8 is a 3 circle diffractometer where 2θ , Φ and ω are free to rotate whilst χ is fixed at the magic angle (54.74°).

3.16 Powder diffraction

Single crystal X-ray diffraction is a very powerful technique but relies on a single crystal being present which might not represent the bulk of the material. The “nice looking” crystal could be a by-product or a minor phase. Powder X-ray diffraction examines the bulk sample and is a useful technique to examine the crystallinity of a sample as it is a very quick process. The diffraction pattern obtained can be used as a fingerprint and compared to a database of known materials (ICSD) to show whether it is the phase required or a new structure. Single crystal data can be used to generate a simulation powder pattern for better comparison.

Powder X-ray diffraction works in a similar way to single crystal except instead of having diffraction spots from one crystal there are hundreds of tiny crystallites which all contribute diffraction spots and as a result diffraction rings (*Figure 3.15*). This property makes it difficult to solve the structure from a powder pattern as it is very difficult to deconvolute the data as the 3D array of the diffracting peaks is compressed into 2D and as a result there is a lot of peak overlap making it difficult to index and obtain a solution. If enough information is available about the structure it may still be solved but it is more time consuming than with single crystal data.

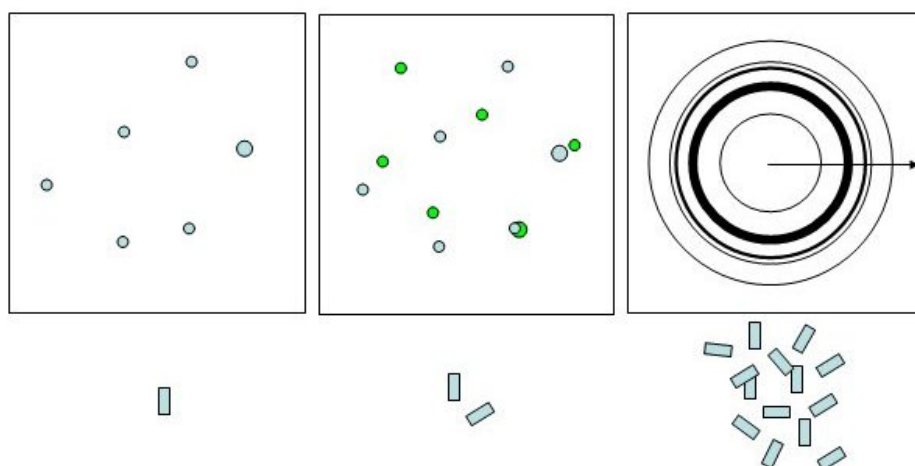


Figure 3.15: Powder diffraction is similar to single crystal however instead of examining a single crystal, a large number of crystallites are seen with random orientations leading to the diffraction spots overlapping to form rings (far right diagram). A normal powder diffraction pattern is viewed by slicing the rings as shown by the arrow. The direction of the arrow indicated an increasing diffraction angle (2θ).

3.17 Experimental

A powder diffractometer consists of an X-ray source, a movable sample platform, an X-ray detector, and associated computer-controlled electronics. The sample is placed in a sample holder which spins slowly during the experiment to ensure that all orientations of the crystals in the powder are in the X-ray beam. The X-ray beam is fixed and the sample platform rotates with respect to the beam by an angle θ . The detector rotates at twice the rate of the sample and is at an angle of 2θ with respect to the incoming X-ray beam.

My data were collected on a STOE STADIP diffractometer (*Figure 3.16*) using monochromated $\text{Cu K}\alpha_1$ radiation working in transmission mode.



Figure 3.16: Stoe Powder diffractometer.

3.18 Rietveld refinement

If a structural model is known it can be refined against the observed powder pattern using a Rietveld refinement⁸. The model is refined by minimising the residual, S , by a least squares process where y_{io}, y_{ic} and w_i are the observed and calculated intensities and a suitable weight respectively at the i th step.

$$S = \sum w_i |y_{io} - y_{ic}|^2 \quad (3.15)$$

A least-squares method can be used to try and minimise the difference between y_{obs} and y_{calc} this is usually achieved by refining different parameters such as the diffractometer zero point, background shape and peak shape. Once a good model is achieved the x , y , z coordinates, the unit cell, thermal parameters and site occupancies can also be refined.

The quality of the refinement can be checked by using similar techniques to single crystal diffraction such as the use of weighted residual factors R_{wp} (3.16) and goodness of fit χ^2 (3.18), a powder pattern is expressed in terms of y_{obs} and the intensity is compared to the y_{calc} at a given 2θ .

$$R_{wp} = \left\{ \frac{\sum_i w_i [y_i(obs) - y_i(calc)]^2}{\sum_i w_i [y_i(obs)]^2} \right\}^{\frac{1}{2}} \quad (3.16)$$

A measure of the quality of the data R_{exp} is shown in equation 3.17 where N and P are the number of profile points and refined parameters respectively.

$$R_{exp} = \left\{ \frac{(n-p)}{\sum_{i=1}^n w_i y_i^2} \right\}^{\frac{1}{2}} \quad (3.17)$$

The refined R_{wp} value should approach that of R_{exp} and this is measured by the goodness of fit χ^2 which indicated how well the calculated model fits the observed.

$$\chi^2 = \frac{R_{wp}}{R_{exp}} \quad (3.18)$$

Powder X-ray diffraction has been used in this thesis as a way to determine the crystallinity and purity of the samples.

3.19 Nuclear Magnetic Resonance (NMR)

Single crystal X-ray diffraction is an extremely powerful and informative tool. However, it is not always possible to grow crystals of sufficient quality to obtain a detailed analysis of the compound. Nuclear Magnetic Resonance (NMR)⁹ is a complementary spectroscopic technique which when used in conjunction with X-ray data can provide a wealth of new information. Nuclear Magnetic Resonance was first discovered by Bloch and Purcell in 1945^{10,11} as a tool for physicists but is now probably more widely used by chemists as one of the most important characterisation tools for examining structures in both the solution and solid phases.

3.20 Solution NMR

Atomic nuclei possess an intrinsic angular momentum known as spin (I) quantised in units of \hbar (3.19), which is determined by the number of protons and neutrons a nucleus possesses. If a nucleus has an angular momentum (I) of zero the nucleus is NMR inactive (e.g. ^{12}C , ^{16}O).

$$|I| = \hbar(I(I+1))^{1/2} \quad (3.19)$$

Spin is a vector with both a magnitude and a direction. It is related to the magnetic moment (μ) of a nucleus (3.20) through the gyromagnetic ratio (γ) making the nuclei act like tiny bar magnets.

$$\mu = \gamma I \quad (3.20)$$

When a magnetic nucleus is placed in a magnetic field it can adopt one of a small number of orientations ($2I + 1$). For example a ^1H with a spin of $\frac{1}{2}$ can have two orientations aligned either with the field or against the field (*Figure 3.17*). These orientations are separated by an energy ΔE and are dependent of the interaction on the nucleus with the field applied. This value can be measured by applying electromagnetic radiation of frequency (ν) and it is this energy which can flip the nuclei from low to high energy $\Delta E = h\nu$ (h is Planck's constant).

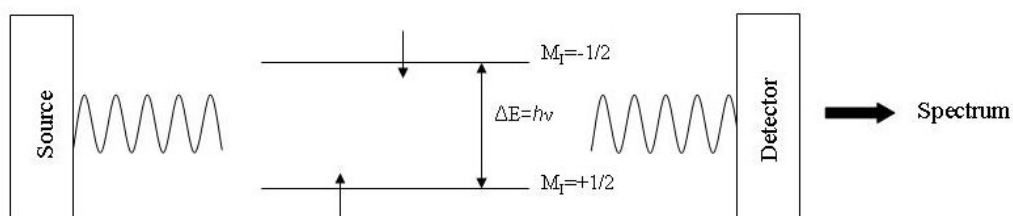


Figure 3.17: A radiofrequency pulse is applied to a system which causes a change in the spin orientation and thus energy. When there is a relaxation a Free Induction Decay is recorded and transformed to produce a spectrum which can be interpreted.

The coherence produced by the precession of the nuclei to equilibrium is recorded as a time domain signal known as a Free Induction Decay (FID), which is then mathematically converted into frequency domain using a Fourier Transform (FT). The data is shown in parts per million (ppm) which defines the chemical shift (δ), a property that depends on the fact that electrons in a molecule shield the nucleus from the external magnetic field to varying degrees resulting in the nucleus absorbing energy at different frequencies in different chemical environments.

3.21 Zeeman Interaction

Without the presence of an external magnetic field all nuclei spins have $2I + 1$ possible orientations which are degenerate in energy. The application of a strong magnetic field B_0 defines the axis of quantisation and the degeneracy is lifted, this is known as the Zeeman interaction where the different orientations of the magnetic dipole moments μ_z now have different energies.

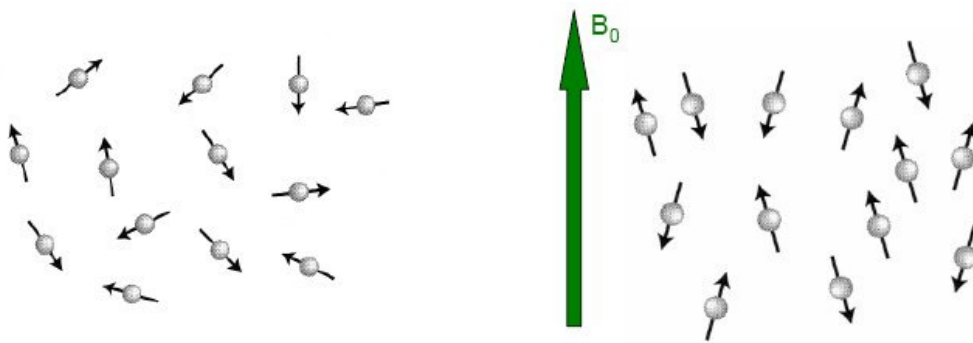


Figure 3.18: Zeeman interaction, in the presence of a magnetic field (B_0) the spins are either aligned with or against the field.

$$E = -\mu_z B_0 \quad (3.21)$$

When μ_z is parallel to the external magnetic field $I=1/2$ nuclei have lower energy, when antiparallel the nuclei have higher energy. The energy difference depends on B_0 and γ . When the spin angular momentum and the magnetic moment are aligned the gyromagnetic ratio is positive when they are not aligned the ratio is negative.

3.22 Chemical Shift

The chemical shift is an important characteristic of NMR as it helps to distinguish between nuclei and arises because the field experienced by a nucleus (B) is not equal to the field that a bare nucleus (B_0) would experience. This is due to an external field causing the electrons to circulate within their atomic orbitals thus generating a field B' in the opposite direction to B_0 .

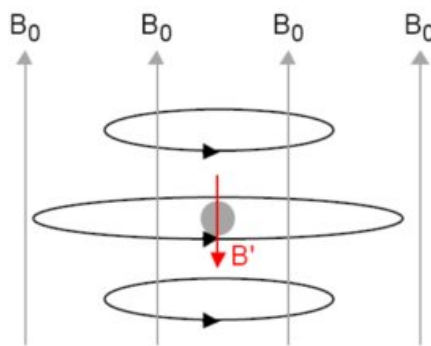


Figure 3.19: The external field B_0 causes the electrons to circulate generating an opposite field B' .

The nucleus is said to be “shielded” from the external field, B' and is proportional to B_0 . The higher the field the faster the frequency of precession as defined by equation 3.22 where σ is the shielding constant.

$$B = B_0 - B' = B_0(1 - \sigma) \quad (3.22)$$

$$\nu = \frac{\gamma B}{2\pi} \quad (3.23)$$

As a result of shielding the resonance condition (3.23) can be rewritten (equation 3.24).

$$\nu = \frac{\gamma B_0 (1 - \sigma)}{2\pi} \quad (3.24)$$

The chemical shift is usually defined in terms of the difference in resonance frequencies between the nucleus of interest (ν) and a reference nucleus (ν_{ref}) (equation 3.25) and is shown in parts per million (ppm) with a spectrum plotted with increasing δ from right to left.

$$\delta = \frac{10^6 (\nu - \nu_{ref})}{\nu_{ref}} \quad (3.25)$$

3.23 Solid state NMR

Solution state NMR is a very powerful technique although sometimes it is not always possible to readily dissolve some materials. However with the development of solid state NMR techniques it is possible to examine these materials and it has become an extremely valuable complementary technique to those already used by materials chemists to probe materials further.

3.24 Solid vs. solution state NMR

Solid state NMR¹² is theoretically the same as in the solution state however there are some fundamental practical differences between the techniques and as such experiments have to be changed to accommodate these differences.

Solids are by definition rigid and anisotropic in nature (orientation dependent) whilst the molecules in the liquid phase are free to tumble (isotropic). This affects the chemical shifts and is known as chemical shift anisotropy.

3.25 Chemical shift anisotropy

In a single crystal all molecules have the same orientation with respect to B_0 . However different single crystals will have a different orientation with respect to B_0 . Within a powdered sample there are millions of single crystals with different orientations resulting in a characteristic broad powder pattern lineshape (*Figure 3.20*). An isotropic environment produces a sharp single peak which can be seen in the solution state, an anisotropic environment leads to a broad peak which is difficult to resolve with the possibility of peaks lying on top of each other.



Figure 3.20: Characteristic powder pattern of an solid state NMR experiment.

3.26 Dipolar interactions

Nuclear spins possess a magnetic moment and in a collection of spins these can interact with each other which are referred to as a dipolar interaction. In solution this interaction is averaged to its isotropic value of zero due to molecular tumbling. However this is not the case in solids and can lead to line broadening.

The strength of the dipolar interaction between two spins k and j is given by equation 3.26 where ω_D^{PAS} is the dipolar coupling constant and θ_{jk} is the angle that the internuclear vector makes with the B_0 , the external magnetic field and ω_D^{PAS} is the dipolar-coupling constant given by equation 3.27 with the strength of the interactions proportional to the gyromagnetic moments of either nuclei and inversely proportional to the distance cubed between spins.

$$\omega_D = \omega_D^{PAS} \frac{1}{2} (3 \cos^2 \theta_{jk} - 1) \quad (3.26)$$

$$\omega_D^{PAS} = \left(\frac{\mu_o}{4\pi} \right) \frac{\gamma_j \gamma_k \hbar}{r^3} \quad (3.27)$$

The dipolar interaction is orientation dependant and as the angle with the internuclear vector makes with the magnetic field varies the dipolar splitting also varies until it is zero at 54.736° .

Even though we are interested in removing these interactions it should be noted that in materials science these interactions are very useful as they can provide us with information not previously known. This is due to the direct dependence of its magnitude on the distance r_{jk} between the two spins k and j and as such can provide us with a way of determining internuclear distances, geometry and conformation of molecules.

3.27 Magic-angle spinning

Magic Angle Spinning (MAS) exploits the fact that chemical shift anisotropy and dipolar couplings have a similar orientation dependence. To remove the broadening in a powdered sample all the crystallites to have the same orientation simultaneously. It has been noted that dipolar interactions and CSA are zero when the sample is oriented at the magic angle of 54.736° (Figure 3.21) and the rotation is fast. Experimentally, if we are able to rotate the powdered sample at very fast speeds around this angle the contribution from the dipolar interaction and the chemical shift anisotropy is zero thus improving the resolution and sensitivity of the spectrum.

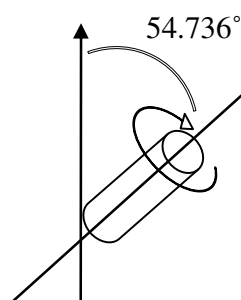


Figure 3.21: The magic angle of 54.736° is used to mimic isotropic motion present in solution NMR.

3.28 Decoupling

Dipolar interactions can also be removed by decoupling where a radiofrequency irradiation can be applied to remove the interaction of an undesired nuclei.

3.29 Quadrupolar interactions

Quadrupolar nuclei are those with a spin number $I > 1/2$ (^{27}Al , ^{17}O) and give rise to a quadrupole moment (eQ) which interacts with electric field gradient present at the nucleus (eq). This interaction is anisotropic in nature and therefore orientation dependent with respect to B_0 , producing broad lines in solids, but it is averaged away in liquids by the rapid molecular motion.

The magnitude of this interaction is defined by the Quadrupolar coupling constant (C_Q) and is measured in Hertz (3.28).

$$C_Q = eQV_{zz}/h$$

A quadrupolar constant equal to zero indicates high symmetry and as the symmetry of the system decreases C_Q increases. The broadening from quadrupolar interactions can be very large and can even be known as the dominant interaction in solid-state NMR.

3.30 Multiple Quantum (MQ) MAS

As mentioned previously magic angle spinning is an extremely useful tool in solid state NMR in that it can remove first order quadrupolar broadening but not second order broadening. A Multiple Quantum (MQ) MAS experiment can be performed to produce a

high resolution 2-D spectrum (*Figure 3.22*) which involves correlating a MAS spectrum with a multiple-quantum spectrum to produce a high resolution spectrum.

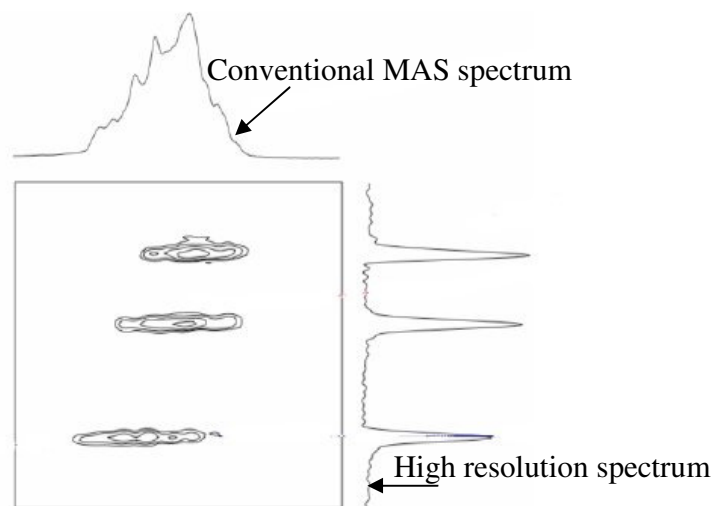


Figure 3.22: A two dimensional Multiple Quantum (MQ) MAS

3.31 CASTEP

NMR calculations were carried out using the CASTEP^{13,14} density functional theory (DFT) code, which employs the gauge including projector augmented wave (GIPAW)¹⁵ algorithm, to reconstruct the all-electron wave function in a magnetic field. The generalized gradient approximation (GGA) PBE¹⁶ functional was used and the core-valence interactions were described by ultrasoft pseudopotentials¹⁴. The NMR parameters are calculated from diffraction data (X-ray/neutron). The cut-off energy determines the number of plane waves in the basis set, and the k-point spacing determines, the accuracy with which the electron density is calculated

3.32 Techniques used

Within this thesis the following techniques were used, Magic Angle Spinning and High resolution ^{27}Al and ^{31}P spectra. Solution NMR ^1H was also used to confirm if the ionic liquid had been synthesised. Calculations were performed using the EaStCHEM Research Computing Facility, which consists of 136 AMD Opteron processing cores partly connected by Infinipath high speed interconnects. Typical NMR calculation (CASTEP) times were 24 hours using 3 cores.

3.33 Thermogravimetric Analysis (TGA)

Thermogravimetric Analysis is used to measure the loss of mass in microporous materials when heated under an atmosphere of either nitrogen or oxygen. The loss in mass can provide information on the stability of the material and help to confirm the molecular formula. Samples were examined using a Netzsch thermische Analyse TG 209 analyser.

3.34 Bibliography

¹ G. Burns, A.M. Glazer, *Space Groups for Solid State Scientists*, Academic Press, New York, 1990.

² T. Hahn, *International Tables for Crystallography*, Kluwer Academic Publishers, Boston, 1996.

³ http://en.wikipedia.org/wiki/X-ray_tube

⁴ <http://www.diamond.ac.uk/default.htm>

⁵ <http://www.cds.dl.ac.uk>

⁶ G.M. Sheldrick, *Acta Cryst A.*, 2008, 64,112-122

⁷ <http://icsdweb.fiz-karlsruhe.de/>

⁸ H.M. Rietveld, *J.Appl.Cryst.*, 1969, **2**, 65-71

⁹ J. P. Gluster and K. N. Trueblood, *Crystal Structure Analysis*, Oxford University Press, 1972

¹⁰ C. Hammond, *The Basics of Crystallography and Diffraction*, International union of crystallography Oxford Press,1997

¹¹ W. Clegg, *Crystal Structure Determination*, Oxford University Press, 1998

⁹ P. J. Hore, *Nuclear Magnetic Resonance*, Oxford University Press, 1995

¹⁰ E. M. Purcell, H.C. Torrey, and R.V. Pound. *Phys. Rev.*, 1946, **69**, 37

¹¹ F. Bloch, W.W. Hansen and M. Packard, *Phys Rev*, 1946, **69**, 127

¹² M. J. Duer, *Solid-state NMR spectroscopy principles and applications*, Blackwell Science, 2002

- ¹³ M. D. Segall, P. J. D. Lindan, M. J. Probert, C. J. Pickard, P. J. Hasnip, S. J. Clark and M. C. Payne, *J. Phys. Cond. Matt.*, 2002, **14**, 2717.
- ¹⁴ J. R. Yates, C. J. Pickard and F. Mauri, *Phys. Rev B.*, 2007, **76**, 024401.
- ¹⁵ C. J. Pickard and F. Mauri, *Phys. Rev B.*, 2001, **63**, 245101
- ¹⁶ J. P. Perdew, K. Burke and M. Ernzerhof, *Phys. Rev. Lett.*, 1996, **77**, 3865.

4 Ionothermal Synthesis of Metal Phosphonates

4.1 Introduction

As described in chapter 1 metal phosphonates ($M(RPO_3)_x$) are an example of an inorganic-organic hybrid which have potential in many applications such as in sorption¹, NLO^{2,3} and catalysis.⁴ They are similar to metal phosphates. However, unlike the purely inorganic phosphates functionality can be introduced to these materials by replacing a hydroxide with an organic substituent.

In general, new phosphonate materials have been prepared using traditional hydro/solvothermal approaches using water or organic molecular solvents.^{5,6,7,8} Ionothermal synthesis^{9,10} is the use of an ionic liquid¹¹ as solvent, and in many cases the template provider, in materials synthesis.^{12,13} A major advantage over hydrothermal and traditional solvothermal reaction conditions is that ionothermal synthesis takes place at ambient pressures due to the ionic liquid's vanishingly low vapour pressure, thus avoiding the high autogenous pressures (up to 15 atm at 200°C) and associated safety concerns that accompany hydrothermal/solvothermal synthesis.

The different chemistry of the ionothermal solvent system, as compared to that of the traditionally used hydrothermal and solvothermal systems, produces conditions under which novel structure types appear to be accessible. In the field of aluminium phosphates these include several new zeolites or zeolite analogues while other materials, such as metal-organic-frameworks (MOFs),¹⁴ are equally accessible. A recent paper by Parnham *et al*¹⁵ reported the first ionothermal synthesis of a transition metal diphosphonate material.

4.2 Aim

The aim of this chapter is develop the ionothermal method by synthesising and characterising novel aluminium and gallium metal phosphonates. Group 13 metals are of particular interest due to their heavy use in phosphate synthesis which usually results in many different porous networks, which have many potential applications.¹⁶

4.3 Aluminium Phosphonates

Aluminium phosphates are of great interest in industry thanks to their porous nature and stability, phosphonates are therefore a natural progression to try and provide functionality to a framework. Much of the work on aluminium phosphonate solids have led to layered^{17,18,19,20,21} structures, this due to the bulky nature of the organic used. Pillared diphosphonates^{22,23,24} have also attracted much attention because the organic groups lead to unusual chemistry lining the internal surfaces of the channels. However one of the most interesting aluminium phosphonates was synthesised by Maeda *et al* who successfully used methylphosphonates to synthesis the porous frameworks AlMePO- α ²⁵ (*Figure 4.1*) and AlMePO- β ^{26,27} which has been shown as a potential catalyst for the oxidation of phenol²⁸. Another interesting aluminium phosphonate is the MIL-91²⁹ structure as it has demonstrated porosity to molecules other than water.

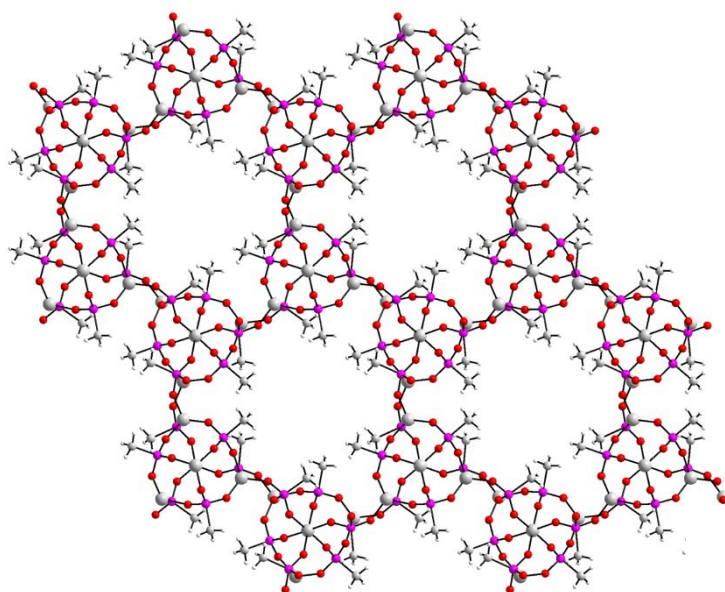


Figure 4.1: The structure of AlMePO- α with the methyl groups from the phosphonic acid clearly visible pointing into the channels

Other porous metal phosphonates have been synthesised³⁰ but so far only the AlMePO- β and AlMePO- α frameworks are known to reversibly adsorb molecules larger than water within their pores.¹ Harvey and co-workers³¹ synthesised a novel aluminium diphosphate ($\text{Al}_2[\text{O}_3\text{PC}_2\text{H}_4\text{PO}_3](\text{H}_2\text{O})_2\text{F}_2 \cdot \text{H}_2\text{O}$) which contains relatively small channels ($5.7 \times 5.3 \text{ \AA}$) and as such when the framework was heated to 190°C to remove the extra-framework and coordinated water molecules it was not possible for the structure to reversibly reabsorb the extra-framework water molecules. An increase in carbon length (e.g. ethyl, propyl etc.) results in an as expected larger framework Attfield *et al*³² synthesised $\text{Al}_2[\text{O}_3\text{PC}_4\text{H}_8\text{PO}_3](\text{H}_2\text{O})_2\text{F}_2 \cdot 2\text{H}_2\text{O}$ which has a pore size of $3.394 \times 4.861 \text{ \AA}$, when heated 92% of the extra-framework waters are removed up to

200°C and above this temperature framework water molecules are removed but a loss in crystallinity results highlighting the importance of the framework water molecules in the structure.

4.4 Gallium Phosphonates

Gallium phosphonates have also been investigated in this work due to their similarities with phosphates. It was not until 1998 when the first gallium phosphonates³³ $\text{Ga}(\text{OH})(\text{O}_3\text{PC}_2\text{H}_4\text{CO}_2\text{H})\cdot\text{H}_2\text{O}$ and $\text{Ga}_3(\text{OH})_3(\text{O}_3\text{PC}_2\text{H}_4\text{CO}_2)_2\cdot 2\text{H}_2\text{O}$ structures were successfully synthesised by using (2- carboxymethyl)phosphonic acid, resulting in layered structures. Many different types of gallium phosphonate structures have been identified; clusters,³⁴ layered⁵ and more recently pillared materials²³ have been synthesised. Unlike aluminium phosphonates no known porous gallium phosphonate has been successfully synthesised. However, an isostructural Ga form of $(\text{Al}_2[\text{O}_3\text{PC}_2\text{H}_4\text{PO}_3](\text{H}_2\text{O})_2\text{F}_2\cdot\text{H}_2\text{O})^{31}$ was successfully synthesised and unlike the Al version it reversibly reabsorbed approximately 40% of the extra-framework water, which was attributed to the larger cation used resulting in a larger channel. Harvey and co-workers⁸ have provided a novel approach to phosphonate chemistry by synthesising a $\text{Ga}_2\{[\text{O}_3\text{PCH}_2(\text{C}_6\text{H}_4)\text{CH}_2\text{PO}_3]_{1-x}(\text{HPO}_3)_{2x}\}$ ($0 \leq x \leq 0.146$) framework where some diphosphonate groups were replaced with phosphite groups in the reaction mixture to result in a more open structure and the largest aperture for a group 13 diphosphonate.

4.5 Aluminium Phosphonates

4.6.1 $\text{Al}_5\text{F}((\text{C}_4\text{H}_9)\text{PO}_3)_6(\text{OH})_2(\text{C}_8\text{N}_4\text{H}_6)_2$

A novel ionothermally prepared aluminium phosphonate $\text{Al}_5\text{F}((\text{C}_4\text{H}_9)\text{PO}_3)_6(\text{OH})_2(\text{C}_8\text{N}_4\text{H}_6)_2$ was synthesised and characterised using X-ray diffraction on station 9.8 at the SRS.

4.6.2 Experimental

All reagents were used as received except for the ionic liquid EMImBr which was prepared as in the literature.¹¹ $\text{Al}_5\text{F}((\text{C}_4\text{H}_9)\text{PO}_3)_6(\text{OH})_2(\text{C}_8\text{N}_4\text{H}_6)_2$ was prepared as follows. Aluminium iso-propoxide, tert-butylphosphonic acid, hydrofluoric acid and EMImBr in a molar ratio 1:1:1:62 were added to a Teflon-lined autoclave and heated to 150°C for 3 days and allowed to cool to room temperature. The products were then recovered via filtration and dried in air.

4.6.3 Powder X-ray diffraction data

Powder X-ray diffraction patterns were collected on a STOE diffractometer operating on monochromated Cu $K_{\alpha 1}$ radiation ($\lambda=1.54056\text{\AA}$) in transmission mode. The Rietveld method³⁵ was used to refine the structural model from the single crystal data using the GSAS³⁶ package and confirm the phase purity of the compounds.

4.6.4 Single crystal X-ray diffraction data.

The crystals were too small for X-ray data to be collected on the in-house X-ray source and so data was collected on the high flux station 9.8^{37,38} at the Synchrotron Radiation Source (SRS), Daresbury U.K at low temperature (30K) using an Oxford n-Helix. The experiment used a Bruker-Nonius APEXII CCD area detector and D8 diffractometer at a wavelength of 0.6703Å. The size of the crystals led to relatively weak data sets. However, all atomic positions could be refined successfully. The structures were solved using direct methods (SHELXS-97³⁹) and refined against F² using the least squares package (SHELXL-97). The hydrogens were added geometrically and all the non hydrogen atoms were refined anisotropically.

Table 4.1: Crystal structure, data collection and refinement details

Sample title	Al ₅ F((C ₄ H ₉)PO ₃) ₆ (OH) ₂ (C ₈ N ₄ H ₆) ₂
Temperature (K)	30
Crystal System	Trigonal
Space group	P3 ₂
Wavelength (Å)	0.6703
Unit Cell Å a, b, c	12.5125(18), 12.5125(18), 29.518(8)
α, β, γ	90, 90, 120
Cell Volume (Å ³)	4002.3(14)
Z	3
Density (calculated) (Mg/m ³)	1.457
Absorption coefficient (mm ⁻¹)	0.361
F(000)	1833
Crystal Size (mm)	0.05 × 0.017 × 0.01
θ range(°)	0.982-24.51
Unique reflections	6201
Reflections collected	10550
Parameters/restraints	633/1
Goodness-of-fit (F ²)	0.963
Final R indices[I>2sigma(I)]	R ₁ = 0.0689, wR ₂ = 0.1411
R indices (all data)	R ₁ = 0.1362, wR ₂ = 0.1721
Largest diff. peak and hole (eÅ ⁻³)	0.65 and -0.56
Index ranges	-15<=h<=15, -12<=k<=15, -35<=l<=36
Refinement method	Full-matrix least-squares on F ²

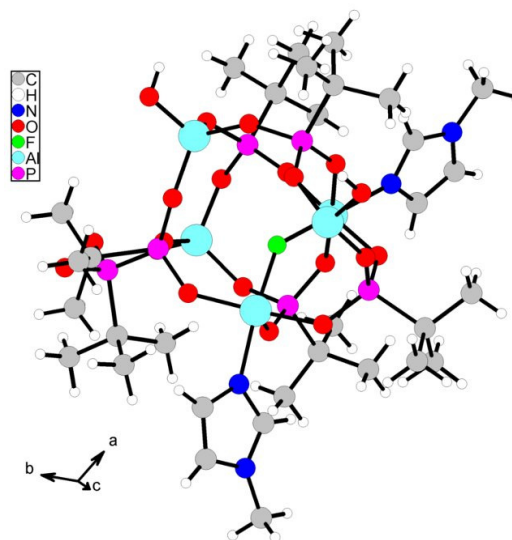


Figure 4.2: The building unit of $\text{Al}_5\text{F}((\text{C}_4\text{H}_9)\text{PO}_3)_6(\text{OH})_2(\text{C}_8\text{N}_4\text{H}_6)_2$ showing the methyl imidazole coordinating to the octahedral aluminium atoms.

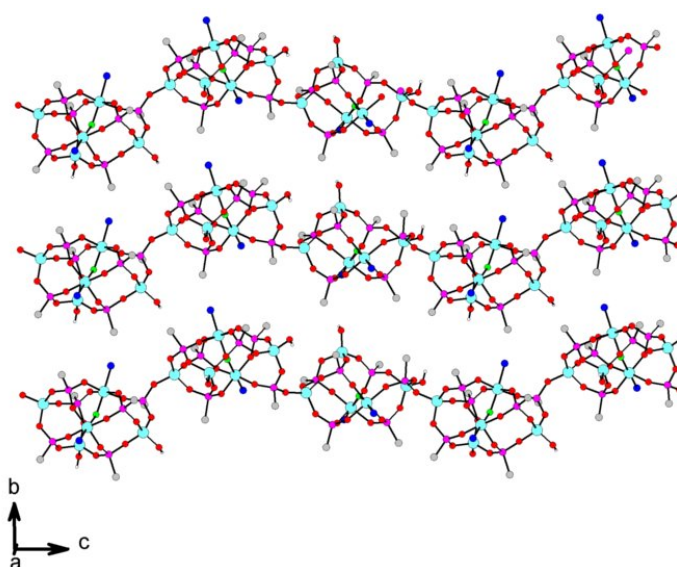


Figure 4.3: The structure of $\text{Al}_5\text{F}((\text{C}_4\text{H}_9)\text{PO}_3)_6(\text{OH})_2(\text{C}_8\text{N}_4\text{H}_6)_2$ viewed parallel to the crystallographic *a*-axis. The imidazole units have been removed for clarity with the nitrogen atoms remain to show the coordination of the metal. The key is as in Figure 4.2.

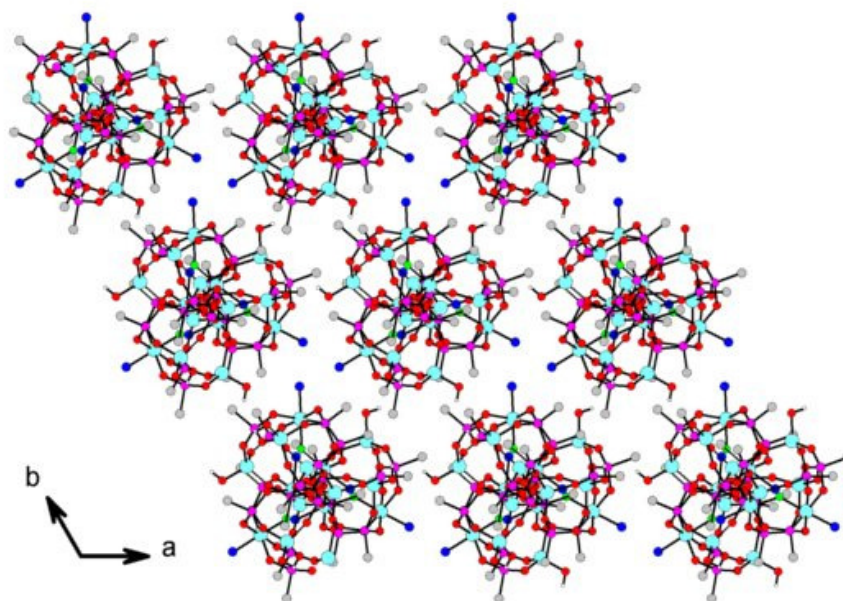


Figure 4.4: View of the chain nature of the structure as views down the crystallographic *c*-axis. The key is as in Figure 4.2.

4.6.5 Results and discussion

The crystal structure, data collection and refinement details for $\text{Al}_5\text{F}((\text{C}_4\text{H}_9)\text{PO}_3)_6(\text{OH})_2(\text{C}_8\text{N}_4\text{H}_6)_2$ can be found in *Table 4.1*. The structure can be described as comprising of a series of cluster-like secondary building units connected parallel to the crystallographic *c*-axis to form a chain. The secondary building unit contains five crystallographically independent aluminium atoms, three of which are coordinated to four oxygen atoms in an approximately regular tetrahedron and the others are octahedrally coordinated. 1-methyl imidazole from the ionic liquid is bound via a nitrogen to the octahedral Al with a fluorine atom bridging the two octahedral Al sites. A hydroxyl group, confirmed by IR spectroscopy with a broad peak at 3500cm^{-1} , is located at one of the tetrahedral Al sites.

Unlike in many instances of ionothermal synthesis where the imidazolium is incorporated into the material as a template the methyl imidazole acts as a ligand and is complexed to the octahedral aluminium atoms. For this to occur there must have been some breakdown of the ionic liquid *in-situ* during the synthesis process, with elimination of ethyl bromide. While ionic liquids are often credited with being extremely stable it is known that they can breakdown under ionothermal conditions, especially in the presence of fluoride ion mineralisers.⁴⁰

The bridging F atom is connected to the two octahedral aluminums with an average bond length of 1.881(5) Å. The tetrahedral P-O distances range from 1.491(5) to 1.552(6) Å whilst those of the P-C bond range from 1.785(9) to 1.802(9) Å. There are two aluminum sites with a bond range of 1.654(5) – 1.770(5) Å for the tetrahedral Al-O bond whilst the octahedral site has a range of 1.858(6) – 1.895(6) Å, F and N complete the octahedral coordination with bond lengths of Al-F 1.866(5)-1.895(5) Å and Al-N 1.999(7)-2.008(7) Å

4.6.6 Thermogravimetric analysis

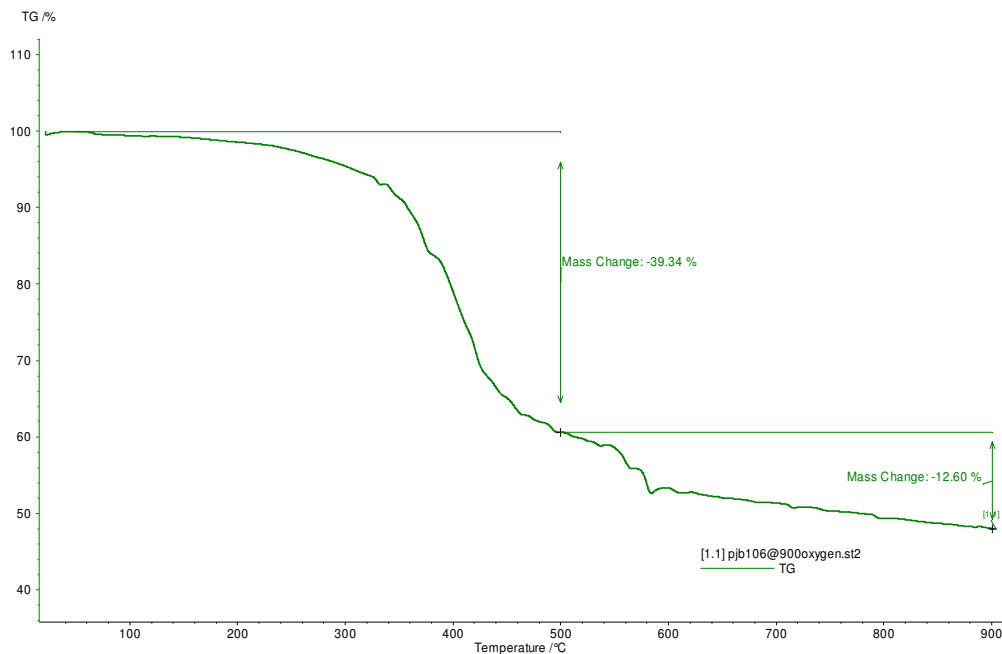


Figure 4.5: Thermogravimetric analysis of $Al_5F(C_4H_9PO_3)_6(OH)_2(C_4N_2H_6)_2$

Thermogravimetric analysis shows that the organic material from the structure begins to be lost at around 300°C and is lost in several distinct steps until about 600°C. The total mass loss measured accounts for the loss of the ionic liquid cation plus the fluorine, followed by decomposition of the phosphonate to lose the organic portion. The overall mass loss (51.9%) is slightly higher than expected simply on the basis of the organic content (47.9%) which possibly indicates that some more complex condensation reactions involving loss of oxygen species are ongoing during thermal decomposition.

4.7 Gallium Phosphonates

4.7.1 GaF(HO₃PCH₃)₂(NH₃CH₃)₂

A novel ionothermally prepared gallium phosphonate (GaF(HO₃PCH₃)₂(NH₃CH₃)₂) was synthesised and characterised using X-ray diffraction on station 9.8 at the SRS.

4.7.2 Experimental

All reagents were used as received except for eutectic mixture (EU) of dimethylurea and choline chloride which was mixed in a ratio of 2:1 respectively. The solid was synthesised by charging a Teflon lined autoclave with gallium (III) sulfate hydrate (0.2g, Aldrich), methylphosphonic acid (0.05g, Aldrich), hydrofluoric acid (10µl, 48% wt in H₂O Aldrich) and 7g EU. The reagents were then heated to 150°C for 7 days and allowed to cool to room temperature. The product was then recovered via filtration washed with water and dried in air.

4.7.3 Single crystal data

The crystals were too small for data to be collected on the in-house X-ray source and so data was collected on Station 9.8^{37,38} at the Synchrotron radiation source (SRS) Daresbury laboratory at 150K. The experiment used a Bruker-Nonius APEXII CCD area detector and D8 diffractometer at a wavelength of 0.69390Å.

GaF(HO₃PCH₃)₂(NH₃CH₃)₂ was solved in direct methods (SHELXS-97³⁹) and refined using the least square package (SHELXL-97³⁹). The hydrogen atoms were added using DFIX, and the non hydrogen atoms were refined anisotropically. Crystallographic data are summarised in *Table 4.2*.

Table 4.2: Crystal structure, data collection and refinement details.

Sample title	GaF(HO ₃ PCH ₃) ₂ (NH ₃ CH ₃) ₂
Temperature (K)	150
Crystal System	Monoclinic
Space group	Cc
Wavelength (Å)	0.6939
Unit Cell Å a,b,c	12.441(25), 14.674(29), 14.674(14)
α,β,γ	90, 90.00(3), 90
Cell Volume (Å ³)	1271.7(4)
Z	4
Density (calculated) (Mg/m ³)	1.791
Absorption coefficient (mm ⁻¹)	2.28
F(000)	704
Crystal Size (mm)	0.2x0.025x0.02
θ range(°)	3.2-30.14
Unique reflections	3644
Reflections collected	6859
Parameters/restraints	181/23
Goodness-of-fit (F ²)	1.056
Final R indices[I>2σ(I)]	R ₁ = 0.0394, wR ₂ = 0.101
R indices (all data)	R ₁ = 0.0415, wR ₂ = 0.1023
Largest diff. peak and hole (eÅ ⁻³)	0.80 and -0.74
Index ranges	-17<=h<=17, -21<=k<=20, -10<=l<=9
Refinement method	Full-matrix least-squares on F ²

4.7.4 Results and discussion

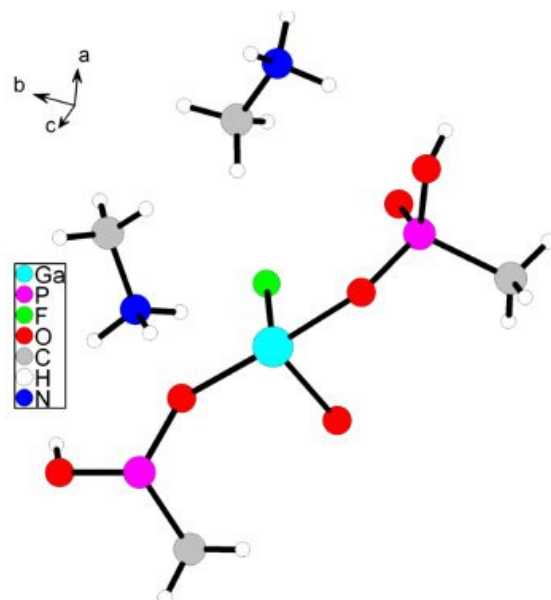


Figure 4.6: The asymmetric Unit (ASU) of GaF(HO₃PCH₃)₂(NH₃CH₃)₂

$\text{GaF}(\text{HO}_3\text{PCH}_3)_2(\text{NH}_3\text{CH}_3)_2$ is a chain structure with one gallium and two phosphorus atoms in the asymmetric unit. The gallium atom is octahedrally coordinated with four oxygen atoms provided from the tetrahedrally coordinated phosphorus atom. The coordination is completed by the bridging F atoms (Figure 4.8) between the gallium atoms. The methyl groups remain intact and are coordinated to the phosphorus. One of the oxygen atoms attached to the phosphorus is not bound to the framework but exists as a hydroxyl group. The P-O bonds range from 1.489(3)-1.533(4) Å and the P-C bond is 1.780(5) Å whilst the Ga-O bond ranges from 1.905(3)-1.939(3) Å. Two methyl ammonium molecules provided from the solvent in the asymmetric unit (Figure 4.6). The building unit is shown in Figure 4.7 and is extended to form a chain material (Figure 4.8) which runs along the crystallographic c axis.

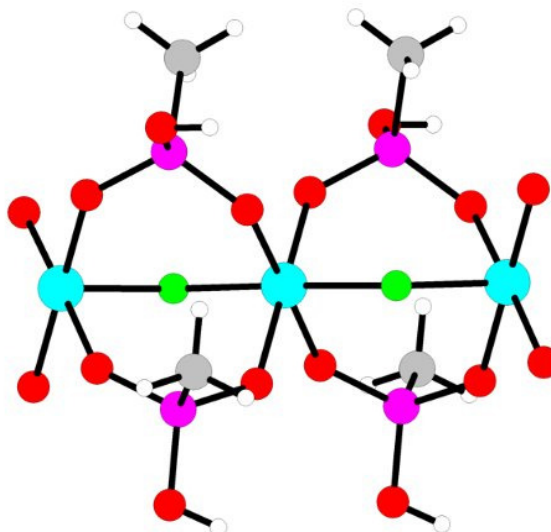


Figure 4.7: Building unit which when extended forms a chained structure along the C axis as viewed in Figure 4.8. The key is as in Figure 4.6.

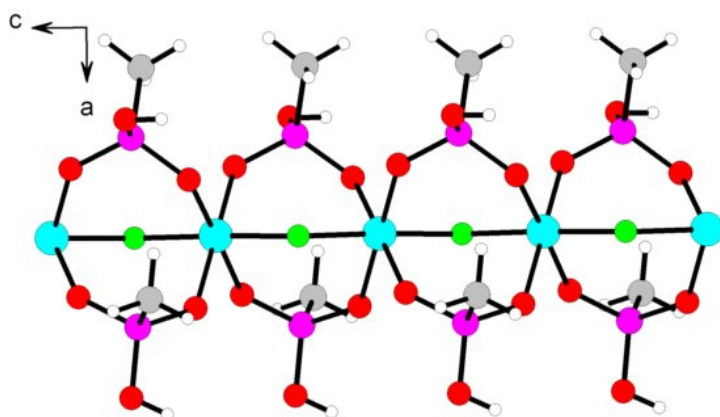


Figure 4.8: This view shows the chain nature of the structure with the gallium atoms bridged by fluorine atoms, the methyl ammonium molecules have been removed for clarity. The key is as in Figure 4.6.

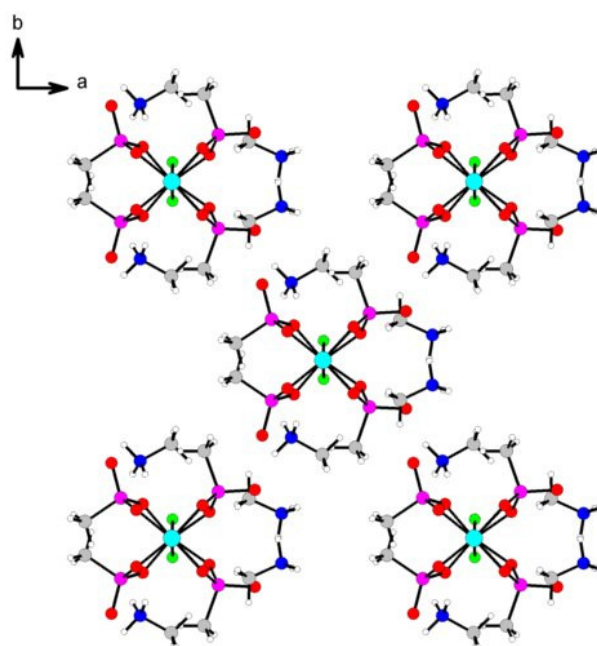


Figure 4.9: The chained nature of the material is clearly visible when viewed down the c axis. The key is as in Figure 4.6.

4.7.5 Powder X-ray diffraction data

A powder X-ray diffraction pattern was collected to confirm the purity of the bulk sample on a STOE diffractometer operating on monochromated Cu $K_{\alpha 1}$ radiation ($\lambda=1.54056\text{\AA}$) in transmission mode. After comparing the theoretical and the observed powder patterns it is evident that the bulk sample is not phase pure. The impurity is unknown at the present time.

4.7.6 TGA

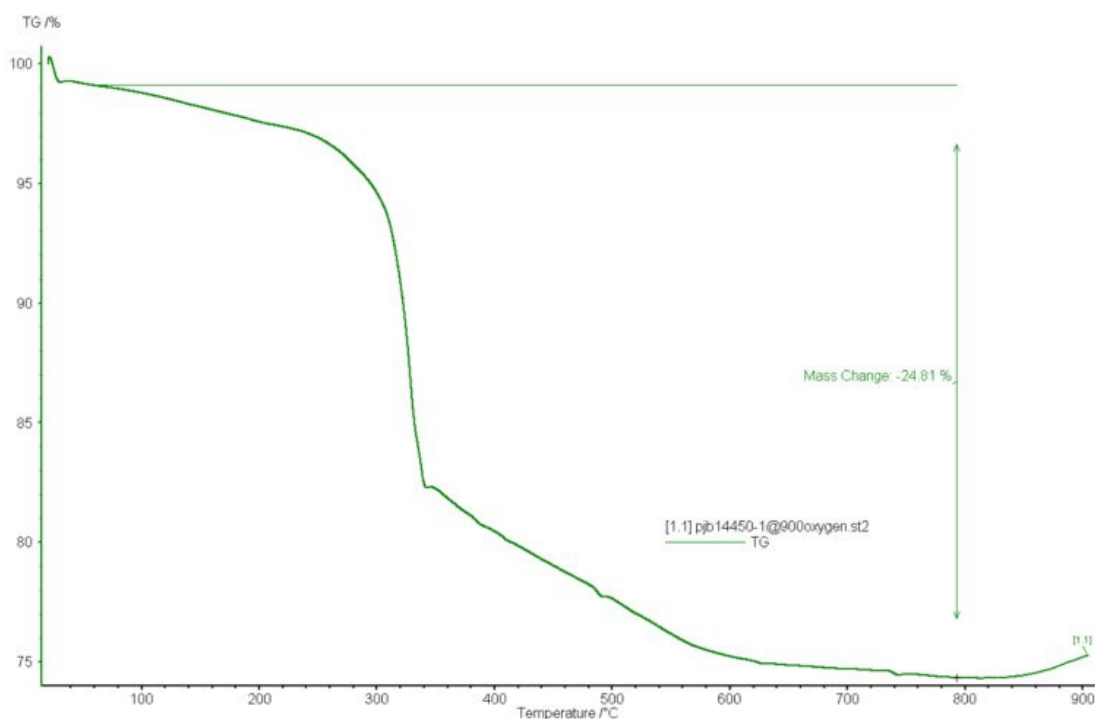


Figure 4.10: Thermogravimetric analysis of $\text{GaF}(\text{HO}_3\text{PCH}_3)_2(\text{NH}_3\text{CH}_3)_2$

Thermogravimetric analysis shows (*Figure 4.10*) one distinct weight loss centred at 325°C with an overall mass loss of 24.81% much smaller than the calculated 33.5% indicating that there is probably another phase present.

4.8.1 Ga₂(O₃PCH₃)₃

A novel ionothermally prepared gallium phosphonate Ga₂(O₃PCH₃)₃ was synthesised and characterised using X-ray diffraction on Station 11.3.1 at the Advanced Light source (ALS) Berkley.

4.8.2 Experimental

All reagents were used as received except for the ionic liquid (1-Methyl 3-ethyl imidazolium bromide EMImBr) which was prepared as described.¹¹ The solid was synthesised by charging a Teflon lined autoclave with gallium (III) sulfate hydrate (0.2g, Aldrich), methylphosphonic acid (0.1g, Aldrich), hydrofluoric acid (10µl, 48% wt in H₂O Aldrich) and 1.7g EMImBr. The reagents were then heated to 150°C for 4 days and allowed to cool to room temperature. The product was then recovered via filtration washed with water and dried in air.

4.8.3 Single crystal data

The crystals were too small for data to be collected on the in-house X-ray source and so data was collected on Station 11.3.1 at the Advanced Light Source (ALS) Berkley USA at 150K. The experiment used a Bruker-Nonius APEXII CCD area detector and D8 diffractometer at a wavelength of 0.71073Å.

$\text{Ga}_2(\text{O}_3\text{PCH}_3)_3$ was solved in direct methods (SHELXS-97³⁹) and refined using the least square package (SHELXL-97³⁹). The hydrogen atoms were added geometrically and all the non hydrogen atoms were refined anisotropically. Crystallographic data are summarised in Table 4.3.

Table 4.3: Crystal structure, data collection and refinement details.

Sample title	$\text{Ga}_2(\text{O}_3\text{PCH}_3)_3$
Temperature (K)	150
Crystal System	Monoclinic
Space group	P2(1)/c
Wavelength (Å)	0.71073
Unit Cell Å a,b,c	9.842(5), 4.950(2), 24.676(11)
α,β,γ	90, 95.203(6), 90
Cell Volume (Å ³)	1197.1(10)
Z	4
Density (calculated) (Mg/m ³)	2.338
Absorption coefficient (mm ⁻¹)	6.214
F(000)	824
Crystal Size (mm)	0.09x0.03x0.015
θ range(°)	2.5-26.5
Unique reflections	2472
Reflections collected	2472
Parameters/restraints	154/0
Goodness-of-fit (F ²)	1.042
Final R indices[I>2 σ (I)]	R ₁ = 0.060, wR ₂ = 0.154
R indices (all data)	R ₁ = 0.083, wR ₂ = 0.169
Largest diff. peak and hole (eÅ ⁻³)	2.75 and -1.59
Index ranges	-12<=h<=12, -6<=k<=6, -30<=l<=30
Refinement method	Full-matrix least-squares on F ²

4.8.4 Results and discussion

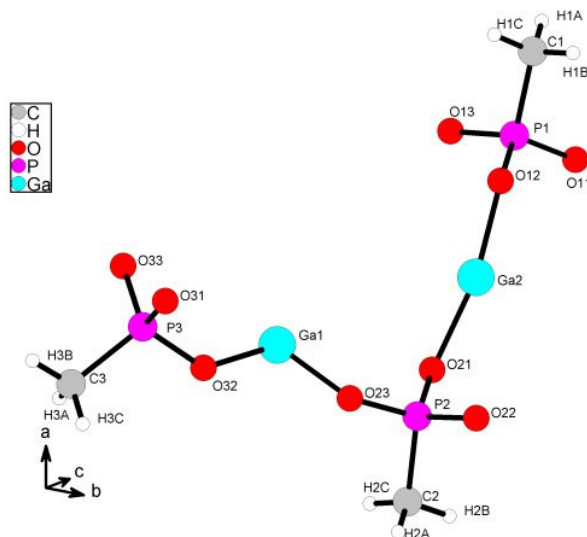


Figure 4.11: The asymmetric unit (ASU) of $Ga_2(O_3PCH_3)_3$

The asymmetric unit consists of 2 gallium, 3 phosphorus, 9 oxygen, 3 carbon and 9 hydrogen atoms. The gallium metal exists as a trigonal bipyramidal and tetrahedral unit (Figure 4.11) bound via the oxygen from the tetrahedrally co-ordinated phosphorus whilst the methyl group remains attached to the phosphorus and points into the voids of this layered structure (Figure 4.12). The layers are separated by an average distance of $3.4626(1) \text{ \AA}$ measured between the hydrogen atoms. The repeating unit in this layered structure occurs at the 5 coordinated gallium. The unit is made up of a four ring which shares an edge with a 6 ring in turn connected to another 4 ring via a corner (Figure 4.13).

The repeating unit (Figure 4.13) builds the layer in the (010) plane (Figure 4.15 is the alternative view of the layer in the (100) plane).

The distances for the P-O bond range from 1.5010(54) to 1.5499(53) Å whilst those of Ga-O bond range from 1.8112 (55) – 1.28281(53) Å and 1.8582(52) -1.9901 (55) Å in the tetrahedral and trigonal bipyramidal units respectively.

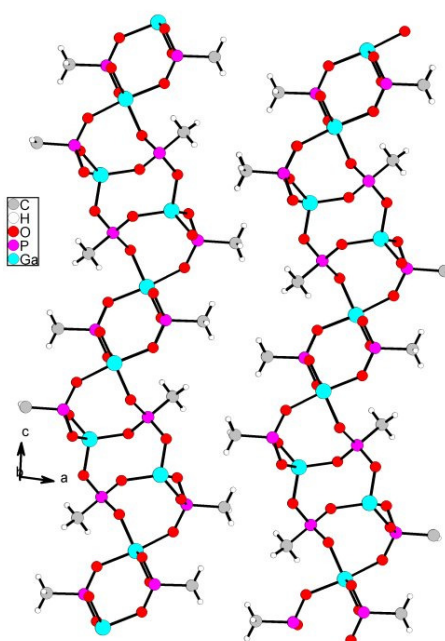


Figure 4.12: Layered structure of $Ga_2(O_3PCH_3)_3$, with the methyl group pointing into the voids. Key is as in Figure 4.11

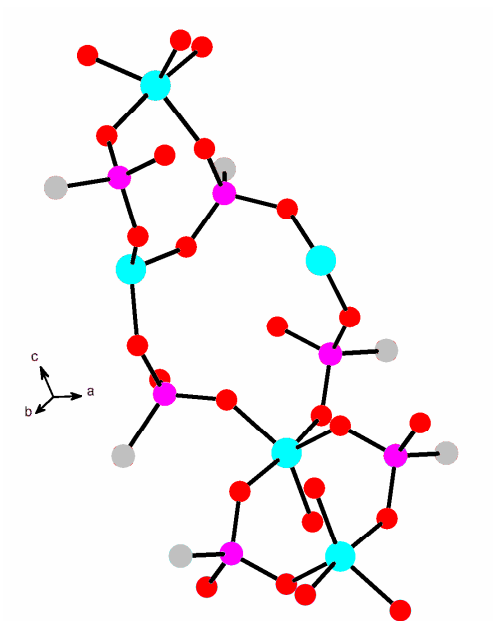


Figure 4.13: 4 ring sharing an edge with a 6 ring coordinated to another 4 ring via a corner. Key is as in Figure 4.11

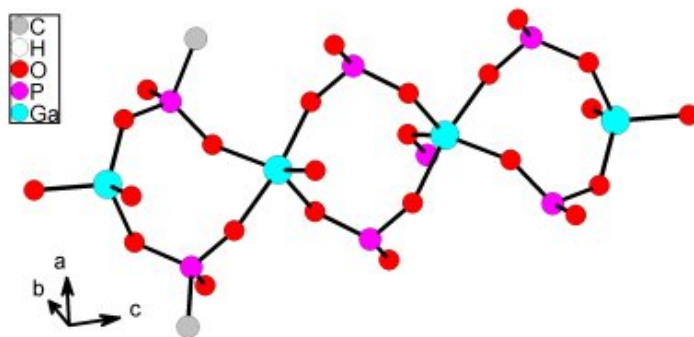


Figure 4.14: Gallium in $Ga_2(O_3PCH_3)_3$ exists in trigonal bipyramidal and tetrahedral units. Key is as in Figure 4.11

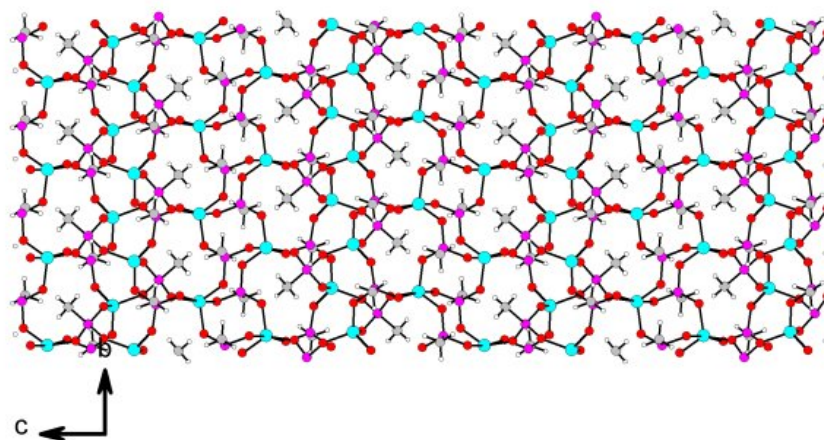


Figure 4.15: A view of the Layer along the 100 plane of $Ga_2(O_3PCH_3)_3$. Key is as in Figure 4.11

4.8.5 Thermogravimetric analysis

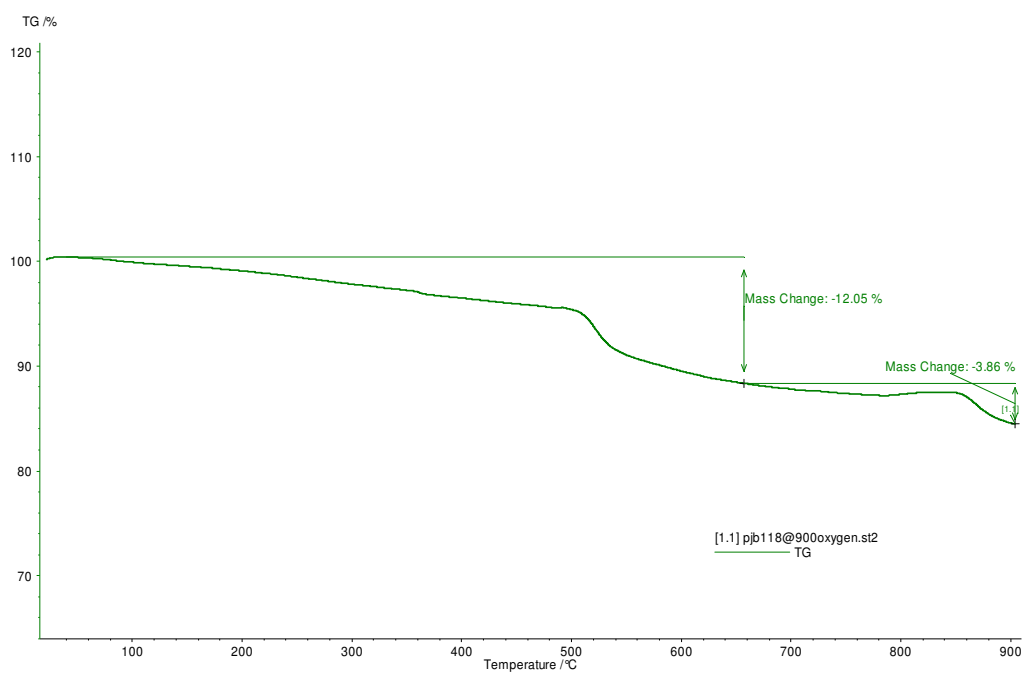


Figure 4.16: Thermogravimetric analysis of $Ga_2(O_3PCH_3)_3$

The sample was heated to 900°C for thermogravimetric analysis (*Figure 4.16*) under an oxygen atmosphere to result in a mass loss at 520°C and 860°C. The loss of 12.05% at 520°C can be attributed to that of the methylgroups whilst that at 860°C (3.86%) is due to the breakdown of the structure.

4.9.1 $\text{Ga}_6(\text{C}_4\text{N}_2\text{H}_6)_4\text{F}_2(\text{O}_3\text{PCH}_3)_8(\text{H}_2\text{O})_{0.4}$

A novel ionothermally prepared gallium phosphonate $\text{Ga}_6(\text{C}_4\text{N}_2\text{H}_6)_4\text{F}_2(\text{O}_3\text{PCH}_3)_8(\text{H}_2\text{O})_{0.4}$ was synthesised and characterised using X-ray diffraction on station 9.8 at the SRS.

4.9.2 Experimental

All reagents were used as received except for the ionic liquid (1-Methyl 3-ethyl imidazolium bromide EMImBr) which was prepared as described¹¹. The solid was synthesised by charging a Teflon lined autoclave with gallium (III) sulfate hydrate (0.2g, Aldrich), methylphosphonic acid (0.1g, Aldrich), hydrofluoric acid (10µl, 48% wt in H₂O, Aldrich) and EMImBr (1.7g). The reagents were then heated to 150°C for 7 days and allowed to cool to room temperature. The product was then recovered via filtration washed with water and dried in air.

4.9.3 Single crystal data

The crystals were too small for data to be collected on the in-house X-ray source and data had to be collected on the high flux station 9.8^{37,38} at the Synchrotron Radiation Source (SRS) Daresbury laboratory, Cheshire, U.K. at 100K. The experiment used a Bruker-Nonius APEXII CCD area detector and D8 diffractometer at a wavelength of 0.6942 Å. Ga₆(C₄N₂H₆)₄F₂(O₃PCH₃)₈(H₂O)_{0.4} was solved in direct methods (SHELXS-97³⁹) and refined using the least square package (SHELXL-97³⁹). The data was not of high quality and ISOR was used to ensure all the non hydrogen atoms could be refined anisotropically to ensure a reasonable model, with the hydrogen atoms added geometrically. Crystallographic data are summarised in *Table 4.4*.

Table 4.4: Crystal structure, data collection and refinement details.

Sample title	Ga ₆ (C ₄ N ₂ H ₆) ₄ F ₂ (O ₃ PCH ₃) ₈ (H ₂ O) _{0.4}
Temperature (K)	100
Crystal System	Monoclinic
Space group	P2(1)/c
Wavelength (Å)	0.6942
Unit Cell Å a,b,c	18.701(12), 14.032(9), 19.093(12)
α,β,γ	90, 94.179(9), 90
Cell Volume (Å ³)	4997(5)
Z	4
Density (calculated) (Mg/m ³)	2.053
Absorption coefficient (mm ⁻¹)	3.542
F(000)	3072
Crystal Size (mm)	0.057x0.03x0.02
θ range(°)	1.42-23.37
Unique reflections	6281
Reflections collected	34725
Parameters/restraints	665/432
Goodness-of-fit (F ²)	1.016
Final R indices [I>2σ(I)]	R ₁ = 0.0993, wR ₂ = 0.2497
R indices (all data)	R ₁ = 0.1787, wR ₂ = 0.3068
Largest diff. peak and hole (eÅ ⁻³)	2.18 and -1.52
Index ranges	-19<=h<=19, -14<=k<=14, -20<=l<=20
Refinement method	Full-matrix least-squares on F ²

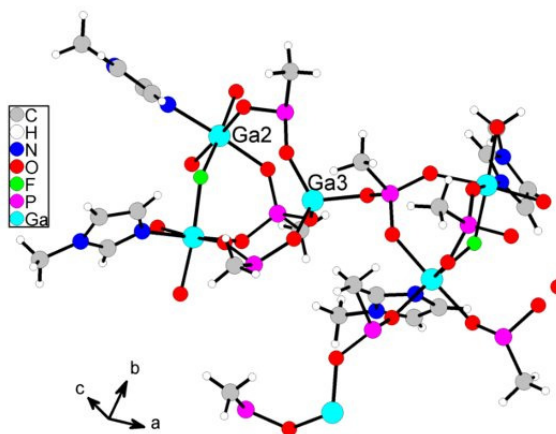


Figure 4.17: The asymmetric unit of $Ga_6(C_4N_2H_6)_4F_2(O_3PCH_3)_8(H_2O)_{0.4}$ with Ga2 octahedrally and Ga3 tetrahedrally coordinated.

$Ga_6(C_4N_2H_6)_4F_2(O_3PCH_3)_8O_{0.4}$ is a layered structure consisting of 6 gallium atoms in the asymmetric unit, 3 of which are octahedrally coordinated whilst the other 3 are tetrahedrally bound. The octahedral gallium atoms have four oxygen atoms around the site and are connected to another octahedral gallium via a bridging fluorine atom. Nitrogen from the ionic liquid completes the co-ordination of the octahedral Ga, a property which has previously been shown by the authors whereby the ionic liquid was bound to an aluminium atom.

There are 8 phosphorus atoms in the asymmetric unit which are tetrahedrally coordinated with three oxygen atoms and the coordinated completed by a methyl group. An oxygen atom was also located between the layers and is probably from the water in the HF solution, the site is only partially occupied and as such it was not possible to locate the hydrogen atoms associated with it.

Figure 4.18 shows the layered undulating nature of the structure as viewed down the [010] with an interlayer distance of 5.710(3) Å as measured between the methyl groups. The distances for the P-O bond range from 1.48(2)-1.58(2) Å whilst those of Ga-O bond range from 1.98(1) -1.92(2) Å and 1.80(1) -1.86(1) Å for the octahedral and tetrahedral sites respectively.

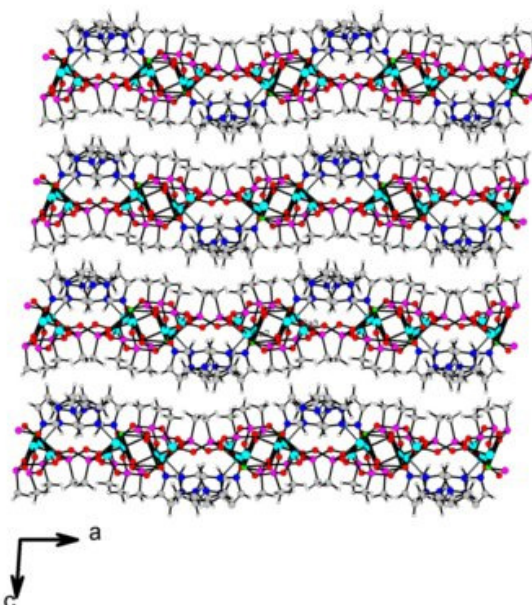


Figure 4.18: Undulating layer structure of $Ga_6(C_4N_2H_6)_4F_2(O_3PCH_3)_8(H_2O)_{0.4}$ as viewed down the [010] plane, the legend is same as in Figure 4.17.

Each layer consists of chains running along the b axis connected via a tetrahedral phosphonate group, each chain can be broken down into building units (*Figure 4.19*), which consist of 2 four membered rings with the octahedral Ga bridged by a fluorine atom. An inversion centre (**I**) can be seen to continue the building unit into a chain like structure. The chains are connected via phosphonate groups to form an 8 membered ring (**A**) in which two ionic liquid rings sit. The 8 membered ring follows the chain with a

90° rotation. The ring from the ionic liquid has been removed for clarity however the N is left to show the coordination of the metal.

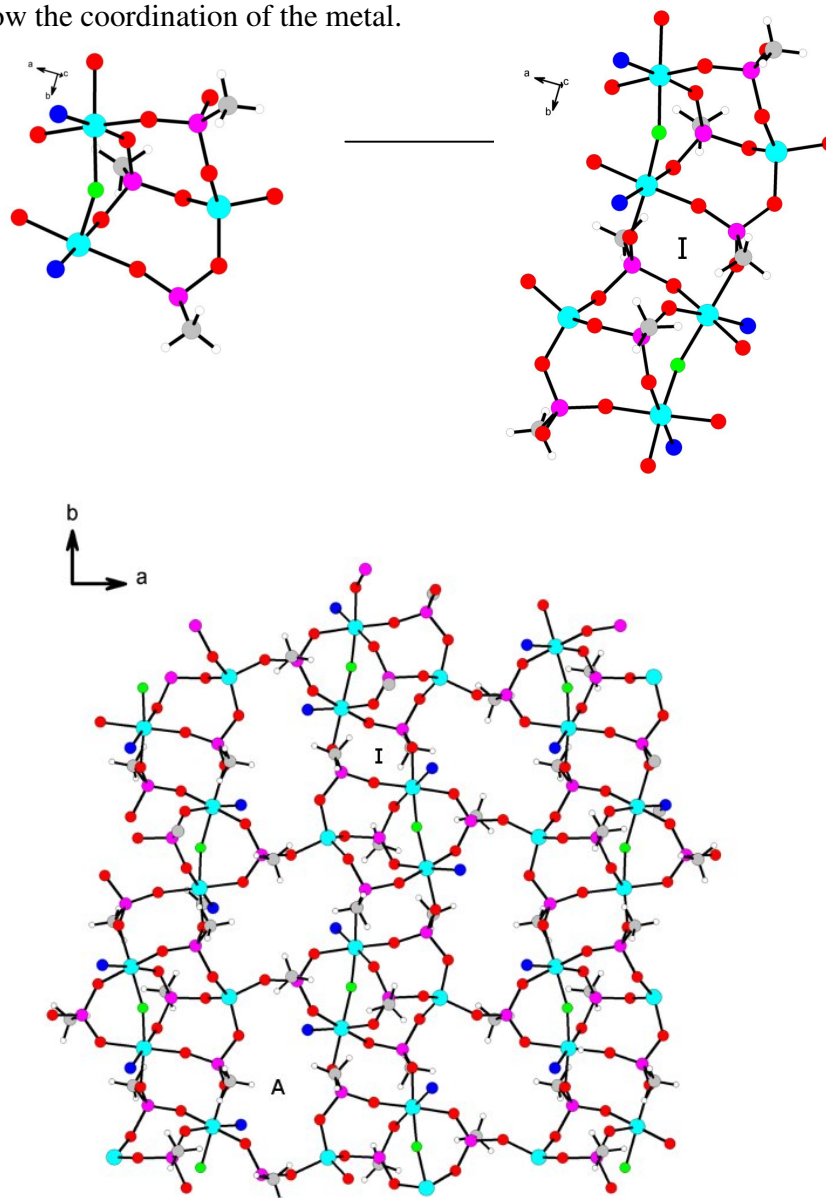


Figure 4.19: The figure at the top left is the primary building unit for the structure which forms a chain via the inversion centre (**I**). The chains are connected via phosphonate groups to form an 8 membered ring (**A**) in which two ionic liquid rings sit. The 8 membered ring follows the chain with a 90° rotation. The ring from the ionic liquid has been removed for clarity with the nitrogen from the ring completing the coordination of the metal.

4.9.4 Powder X-ray diffraction data

Powder X-ray diffraction data were collected on a STOE diffractometer operating on monochromated Cu $K_{\alpha 1}$ radiation ($\lambda=1.54056\text{\AA}$) in transmission mode. The Rietveld method³⁵ was used to refine the structural model from the single crystal data using the GSAS³⁶ package and confirmed the phase purity of the compounds.

4.9.5 Thermogravimetric analysis

Thermogravimetric analysis *Figure 4.20* shows that there is a mass loss at 340°C which accounts for the loss of the ionic liquid cation, the fluorine and water molecule, followed by decomposition of the phosphonate to lose the organic portion. The overall mass loss (28.62%) is slightly lower than expected (31.8%) due to the balancing of charge required on the phosphorus atom to PO_4 .

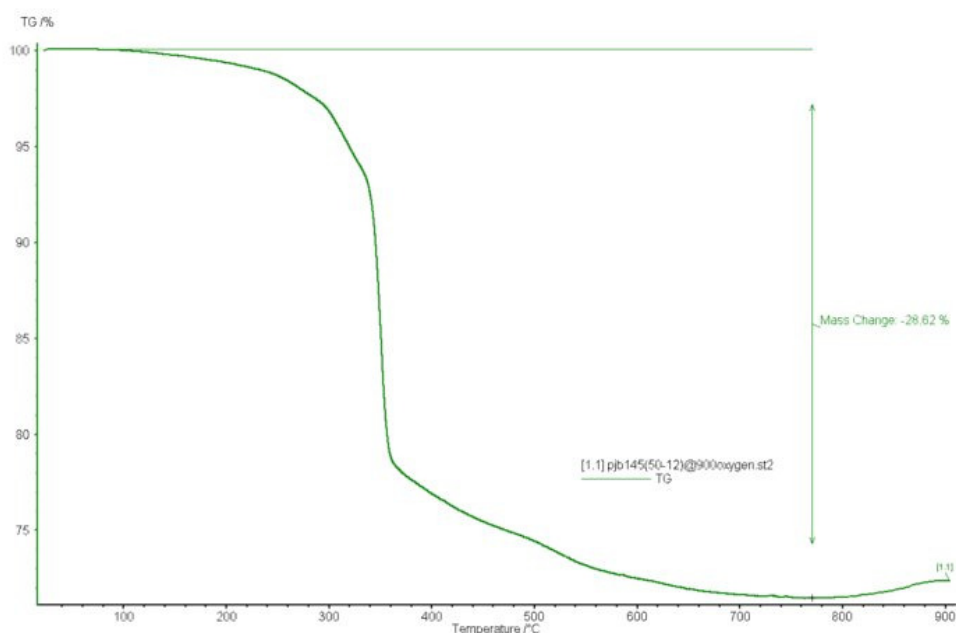


Figure 4.20: Thermogravimetric analysis of $\text{Ga}_6(\text{C}_4\text{N}_2\text{H}_6)_4\text{F}_2(\text{O}_3\text{PCH}_3)_8(\text{H}_2\text{O})_{0.4}$

4.10.1 $\text{Ga}_2\text{F}(\text{C}_4\text{H}_9\text{PO}_3)_4\text{H}_{2.5}(\text{C}_7\text{N}_2\text{H}_{11})_{0.5}$

A novel ionothermally prepared gallium phosphonate $\text{Ga}_2\text{F}(\text{C}_4\text{H}_9\text{PO}_3)_4\text{H}_{2.5}(\text{C}_7\text{N}_2\text{H}_{11})_{0.5}$ was synthesised and characterised using X-ray diffraction on station 9.8 at the SRS.

4.10.2 Experimental

All reagents were used as received except for the ionic liquid EMImBr which was prepared as described in the literature¹¹. $\text{Ga}_4\text{F}_2(\text{C}_4\text{H}_9\text{PO}_3)_8\text{H}_5(\text{C}_7\text{N}_2\text{H}_{11})$ was prepared as follows: Gallium sulphate, tert-butylphosphonic acid, hydrofluoric acid and ethyl methyl imidazolium bromide (EMImBr) in a molar ratio 1:2:1:29 were mixed in a Teflon-lined autoclave and heated to 150°C for 3 days and allowed to cool to room temperature and the products recovered via filtration and dried in air.

4.10.3 Powder X-ray diffraction data

Powder X-ray diffraction data were collected on a STOE diffractometer operating on monochromated Cu $K_{\alpha 1}$ radiation ($\lambda=1.54056\text{\AA}$) in transmission mode. The Rietveld method³⁵ was used to refine the structural model from the single crystal experiment using the GSAS³⁶ package and confirmed the phase purity of the compound.

4.10.4 Single crystal X-ray diffraction data.

The crystals were too small for data to be collected on the in-house X-ray source and so data was collected on the high flux station 9.8^{37,38} at the Synchrotron Radiation Source (SRS), Daresbury U.K at low temperature (30K) using an Oxford n-Helix. The experiment used a Bruker-Nonius APEXII CCD area detector and D8 diffractometer at a

wavelength of 0.6703Å. The size of the crystals led to relatively weak data sets. However, all atomic positions could be refined successfully. The structure was solved using direct methods (SHELXS-97³⁹) and refined against F^2 using the least squares package (SHELXL-97³⁹). The hydrogen atoms were added geometrically and all the non hydrogen atoms were refined anisotropically. The solvent molecules were disordered and could not be located from the difference Fourier maps therefore the program squeeze⁴¹ was used to remove the solvent electron density from the density map.

Table 4.5: Crystal structure, data collection and refinement details

Sample title	$\text{Ga}_2\text{F}(\text{C}_4\text{H}_9\text{PO}_3)_4\text{H}_{2.5}(\text{C}_7\text{N}_2\text{H}_{11})_{0.5}$
Crystal System	Triclinic
Space group	P-1
Sum Formula	C16 H38.5 F Ga2 O12 P4
Wavelength (Å)	0.6703
Unit Cell Å, a,b,c	11.892(4), 12.388(4), 13.6868(4)
α,β,γ	110.103(5), 99.824(5), 95.923(11)
Cell Volume (Å ³)	1861.3(11)
Z	2
Density (calculated) (Mg/m ³)	1.261
Absorption coefficient (mm ⁻¹)	1.492
F(000)	726
Crystal Size (mm)	0.062 × 0.012 × 0.012
θ range(°)	1.5-20.4
Unique reflections	4379
Reflections collected	10871
Parameters/restraints	332/0
Goodness-of-fit (F^2)	1.412
Final R indices [$I > 2\sigma(I)$]	$R_1 = 0.0705$, $wR_2 = 0.1768$
R indices (all data)	$R_1 = 0.0819$, $wR_2 = 0.1808$
R(int)	0.0586
Largest diff. peak and hole (eÅ ⁻³)	1.34 and -0.63
Index ranges	$-12 \leq h \leq 12$, $-12 \leq k \leq 12$, $-14 \leq l \leq 14$
Refinement method	Full-matrix least-squares on F^2

4.10.5 Results and discussion

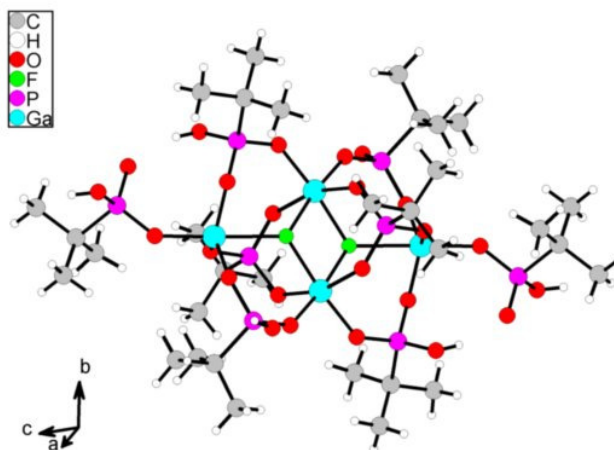


Figure 4.21: The molecular unit for compound $\text{Ga}_4\text{F}_2(\text{C}_4\text{H}_9\text{PO}_3)_8\text{H}_5 \cdot (\text{C}_7\text{N}_2\text{H}_{11})$

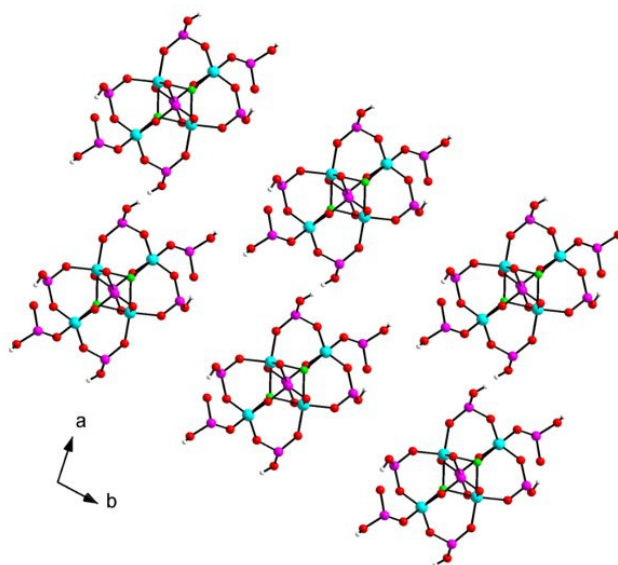


Figure 4.22: Packing diagram of $Ga_4F_2(C_4H_9PO_3)_8H_5 \cdot (C_7N_2H_{11})$ the tert-butyl group has been removed for clarity with the legend the same as Figure 4.21.

Crystal structure, data collection and refinement details for $Ga_4F_2(C_4H_9PO_3)_8H_5 \cdot (C_7N_2H_{11})$ can be found in *Table 4.5*. Analysis shows that the structure consists of discrete units (*Figure 4.21*) composed of two octahedral gallium atoms with an internuclear separation of 3.175 Å connected via bridging fluorine atoms. There are also two gallium sites in the unit which are tetrahedrally bound to the oxygens present from $-PO_3$ groups. There are also four unique phosphorus sites present in the asymmetric unit which still have the tert-butyl phosphonate intact. It was not possible to resolve the template and therefore the program SQUEEZE (contained in the crystallographic program PLATON)⁴² was used to remove any residual electron density, consistent with approximately one ionic liquid cation per molecular $Ga_4F_2(C_4H_9PO_3)_8$ unit.

The distances for the P-O bond range from 1.504(7) - 1.548(7) Å whilst those of P-C range from 1.816(11)-1.822 (11) Å. There are two Ga sites an octahedral site where the Ga-O bond ranges from 1.882(7) - 1.936(7) Å with a Ga-F bond of 2.065(6) Å completing the coordination. The 5 co-ordinate sites have a Ga-O bond range of 1.818(7)-1.862(7) Å. The charge on the unit is balanced by the ionic liquid cation between the units. The diffraction data is not quite good enough to locate the hydrogen positions from Fourier maps but there are several arrangements in the structure that suggest hydrogen bonds are important and hydrogen atoms have been placed in these positions. The majority of these hydrogen bonds are intramolecular, although one per asymmetric unit is intermolecular.

4.10.6 Thermogravimetric analysis

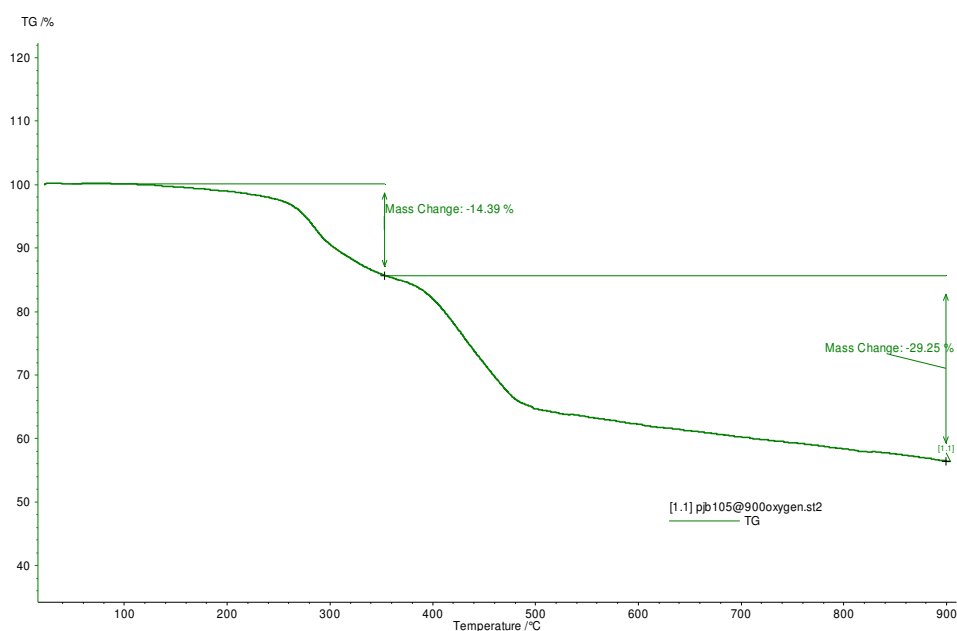


Figure 4.23: Thermogravimetric analysis of $Ga_4F_2(C_4H_9PO_3)_8H_5 \cdot (C_7N_2H_{11})$

Thermogravimetric analysis (*Figure 4.23*) shows two distinct weight losses centred at 325 and 450°C respectively these are likely due to first loss of the ionic liquid cation and fluoride (14.4 %) followed by breakdown of the phosphonate (29.0%). Once again the overall loss is slightly greater than that expected based only on the organic content (40.5%), indicating other process may be ongoing.

Elemental and crystallographic analysis are in reasonable agreement with the structural formula $\text{Ga}_4\text{F}_2(\text{C}_4\text{H}_9\text{PO}_3)_8\text{H}_5\cdot(\text{C}_7\text{N}_2\text{H}_{11})$ calculated C=30.5%, H=5.7%, N=1.8% experimental C=27.49%, H=4.8%, N=2.35%.

4.11 Conclusion

The aim of this chapter was to investigate the influence of ionic liquids in the synthesis of group 13 metal phosphonates and to develop the work previously done by Cooper *et al*^{9,15} on ionothermal synthesis. This work has focused on aluminium and gallium metal phosphonates as they are a natural progression from the work done previously on phosphates and it was believed that using less reagents it might be possible to synthesis materials in a more systematic way. The results found within this chapter demonstrate that it is possible to synthesis metal phosphonates with the use of the ionothermal method whereby the ionic liquid acts as both template and solvent highlighting the diversity of materials which can be produced using this method.

This chapter has shown how it is possible to synthesis many different phosphonates with various substituents using the ionothermal method from which it was possible to

synthesise a molecular structure $(\text{Ga}_2\text{F}(\text{C}_4\text{H}_9\text{PO}_3)_4 \text{H}_{2.5}(\text{C}_7\text{N}_2\text{H}_{11})_{0.5})$ which is unlike the vast majority of hydrothermally prepared methyl phosphonates which result in layered materials. The template, like in many zeolite and zeotype reactions plays a pivotal role in the synthesis process and the use of an ionic liquid is no exception with the template being responsible for three distinct roles which are evident in this work. One of the most interesting roles the ionic liquid played in this work has been as a coordinating ligand, where the ionic liquid breaks down and is included in the framework. This occurred in two of the structures within this chapter $\text{Al}_5\text{F}((\text{C}_4\text{H}_9)\text{PO}_3)_6(\text{OH})_2(\text{C}_8\text{N}_4\text{H}_6)_2$ and $\text{Ga}_6(\text{C}_4\text{N}_2\text{H}_6)_4 \text{F}_2(\text{O}_3\text{PCH}_3)_8(\text{H}_2\text{O})_{0.4}$ whereby the methyl imidazole from the ionic liquid is found bound via the metal site. The coordinating property of a solvent is akin to that provided by water in many hydrothermal preparations such as in the metal organic frameworks HKUST-1⁴³ and CPO-27-Co⁴⁴ but also in the novel aluminium diphosphate $(\text{Al}_2[\text{O}_3\text{PC}_2\text{H}_4\text{PO}_3] (\text{H}_2\text{O})_2\text{F}_2 \cdot \text{H}_2\text{O})$ synthesised by Harvey and co-workers³¹. This property could be adapted and developed to provide another dimension in the functionality capabilities of these systems, which could be useful for other potential applications. Another interesting property provided by the ionic liquid is when it acts as a template delivery agent, where it is possible to locate the template sitting near to the framework, highlighting its charge balancing effect such as that witnessed in the preparation of SIZ-10,⁴⁰ where 1,3-dimethylimidazolium is required to balance the charge from the framework. Within this chapter only one example of the ionic liquid acting as a template delivery agent is demonstrated, this occurred when dimethylurea and choline chloride were used in a eutectic mixture to synthesise $\text{GaF}(\text{HO}_3\text{PCH}_3)_2(\text{NH}_3\text{CH}_3)_2$ from which it was possible to locate methyl ammonium

molecules which were provided by the break down of the eutectic. The final role played by the ionic liquid witnessed in this thesis is its role as a solvent such as in the $\text{Ga}_2(\text{O}_3\text{PCH}_3)_3$ structure where it was not possible to locate the template indicating that the role of the ionic liquid was purely solvent based. This shows the rich behaviour of the ionic liquid in the synthesis process, and highlights its many similarities to water used in the hydrothermal method.

Looking at the conditions used in the preparation of all these materials it would appear that if the ionic liquid can break down during the reaction it will be occluded into the structure. This however is a preliminary observation due to the very few structures that have been synthesised so far using this method. Further work would be needed to confirm these findings so that we can predict the resultant frameworks. NMR studies of the resultant liquid could be used to confirm the breakdown of the template.

4.12 References

- ¹ K. Maeda, Y. Kiyozumi and F. Mizukami, *J. Phys. Chem. B.*, 1997, **101**, 4402
- ² H.E. Katz, G. Scheller, T.M. Putvinski, M.L. Schilling, W.L. Wilson, and C.E.D. Chidsey, *Science*, 1991, **254**, 1485.
- ³ J. Wu, Y. Song, E. Zhang, H. Hou, Y. Fan and Y. Zhu, *Chem. Eur.J.*, 2006, **12**, 5823-5831
- ⁴ C. Maillet, P. Janvier, M. Pipelier, T. Praveen, Y. Andres and B. Bujoli, *Chem. Mater.*, 2001, **13**, 2879
- ⁵ M.P. Attfield, H.G. Harvey and S.J. Teat, *J. Solid State Chem.*, 2004, **177**, 2951-2960
- ⁶ Z. Wang, J. M. Heising and A. Clearfield, *J. Am. Chem. Soc.*, 2003, **125**, 10375-10383
- ⁷ A. Cabeza, M.A.G. Aranda, S. Bruque, D.M. Poojary, A. Clearfield and J. Sanz, *Inorg. Chem.* 1998, **37**, 4168-4178
- ⁸ H.G. Harvey, A.C. Herve, H.C. Hailes and M.P. Attfield, *Chem. Mater.*, 2004, **16**, 3756-3766
- ⁹ E.R. Cooper, C.D. Andrews, P.S. Wheatley, P.B. Webb, P. Wormald and R.E. Morris, *Nature*, 2004, **430**, 1012-1016
- ¹⁰ E.R. Parnham and R.E. Morris *Acc. Chem. Res.*, 2007, **40**, 1005-1013.
- ¹¹ P. Wasserscheid, and T. Welton, T. Ionic Liquids in Synthesis Ch. 2.1.2, 9–12 Wiley-VCH, Weinheim, Germany, 2003
- ¹² E.R. Parnham and R. E. Morris, *J. Am. Chem. Soc.*, 2006, **128**, 2204-2205
- ¹³ E.R. Parnham, P.S. Wheatley and R.E. Morris, *Chem. Commun.*, 2006, 380-382

- ¹⁴ Z. J. Lin, A.M.Z. Slawin and R.E. Morris, *J. Am. Chem. Soc.*, 2007, **129**, 4880-4881;
Z. J. Lin, D.S. Wragg and R.E. Morris, *Chem. Commun.*, 2006, 2021-2023
- ¹⁵ E.R. Parnham, E.A. Drylie, P.S. Wheatley, A.M. Z. Slawin and R.E. Morris, *Angew. Chem. Intl. Ed.*, 2006, **45**, 4962-4966
- ¹⁶ M.E. Davis, *Nature*, 2002, **417**, 813
- ¹⁷ A. Clearfield, *Curr. Op. Sol. State Mater. Sci.* 2002, **6**, 495-506.
- ¹⁸ F. Fredoueil, D. Massiot, D. Poojary, M. Bujoli-Doeuff, A. Clearfield and B. Bujoli, *Chem. Commun.*, 1998, 175-176
- ¹⁹ G.B. Hix, D.S. Wragg, P.A. Wright and R.E. Morris, *Dalton Trans.*, 1998, 3359-3361
- ²⁰ G.B. Hix, V.J. Carter, D.S. Wragg, R.E. Morris and P.A. Wright, *J. Mater. Chem.*, 1999, **9**, 179-185
- ²¹ L. Sawers, V.J. Carter, A.R. Armstrong, P.G. Bruce, P. A. Wright and B.E. Gore, *J.Chem. Soc., Dalton Trans*, 1996, 3159-3161
- ²² H.G. Harvey, B. Slater and M.P. Attfield, *Chem-a Eur. J.*, 2004, **10**, 3270-3278
- ²³ M. Bujoli-Doeuff, M. Evain, P. Janvier, D. Massiot, A. Clearfield, Z. H. Gan and B. Bujoli, *Inorg. Chem.*, 2001, **40**, 6694-6698
- ²⁴ Z.H. Yuan, W. Clegg and M.P. Attfield, *J. Solid State Chem.*, 2006, **179**, 1739-1749
- ²⁵ K. Maeda, J. Akimoto, Y. Kiyozumi and F. Mizukami, *Angew. Chem. Intl. Ed.*, 1995, **34**, 1199-1201
- ²⁶ K. Maeda, *Microporous Mesoporous Mater.*, 2004, **73**, 47-55
- ²⁷ K. Maeda, J. Akimoto, Y. Kiyozumi and F. Mizukami, *Chem. Commun.*, 1995, 1033-1034

- ²⁸ G.O. Rochar, J. Rocha, Z. Lin, *Catal. Lett.*, 2003, **89**, 69
- ²⁹ C. Serre, J.A.Groves, P. Lightfoot, A.M.Z. Slawin P.A. Wright, N. Stock, T. Bein, M. Haouas, F. Taulelle and G. Férey, *Chem. Mater.*, 2006, **18**, 1451-1457
- ³⁰ J. A. Groves, S. R. Miller, S. J. Warrender, C. Mellot-Draznieks, P. Lightfoot, P. A.Wright, *Chem Commun*, 2006, **31**, 3305
- ³¹ H.G. Harvey, S.J. Teat and M.P. Attfield, *J. Mater. Chem.*, 2000, **10**, 2632-2633
- ³² M.P. Attfield, C. Mendieta-Tan, Z. Yuan and W. Clegg, *Solid State Sciences.*, 2008, **10**, 1124-1131
- ³³ F. Fredoueil, D. Massiot, D. Poojary, M. Bujoli-Doeuff, A. Clearfield and B. Bujoli, *Chem. Commun.*, 1998, 175
- ³⁴ C.R. Samanamu, M.M. Olmstead, J. Montchamp, and A. F. Richards, *Inorg. Chem.*, 2008, **47**, 3879-3887
- ³⁵ H.M. Rietveld, *Acta Cryst.*, 1967, **22**, 151-152
- ³⁶ (a) B.H. Toby, EXPGUI, a graphical user interface for GSAS, *J.Appl.Cryst.* 2001, **34**, 210, (b) A.C. Larson and R.B. Von Dreele, General Structure Analysis System (GSAS), Los Alamos National Laboratory Report, 2000, 86
- ³⁷ R.J. Cernik, W. Clegg, C.R.A Catlow, G. Bushnell-Wye, J.V. Flaherty, G.N. Greaves, I. Burrows, D.J. Taylor, S.J. Teat, M. Hamichi, *J. Synchrotron Radiat.* 1997, **4**, 279.
- ³⁸ W. Clegg, M.R.J. Elsegood, S.J. Teat, C. Redshaw, V.C. Gibson, *J.Chem.Soc., Dalton Trans.* 1998, 3037.
- ³⁹ G.M. Sheldrick, *Acta Cryst A.* 2008, **64**,112-122
- ⁴⁰ E.R. Parnham and R.E. Morris, *Chem. Mater.* 2006, **18**, 4882-4887.

- ⁴¹ L. J. Farrugia, *J. Appl. Cryst.* 1999, **32**, 837-838.
- ⁴² P.V.D. Sluis and A.L. Spek, *Acta Crystallogr.*, 1990, **46**, 194-201.
- ⁴³ S.S. Y. Chui, S. M. F. Lo, J. P.H. Charmant, A.G. Orpen, and I.D. Williams, *Science.*, 1999, **283**, 1148-1150
- ⁴⁴ P.D.C. Dietzel, Y. Morita, R. Blom and H. Fjellvåg, *Angew. Chem. Int. Ed.*, 2005,**44**, 6354-6358

5 High resolution charge density X-ray diffraction

5.1 Introduction

As Ernest Rutherford discovered in 1909 an atom does not just consist of a highly dense atom core, it also contains electrons which are free to move and orbit around it. These electrons however interact with electrons in other atoms to form bonds. Until relatively recently it has not been possible to physically see these electrons and the interactions they have with each other. Improved technologies such as high quality area detectors and faster computers have enabled high resolution data sets ($d < 0.5 \text{ \AA}$ or $\sin\theta/\lambda > 1.0$)¹ to be collected with the intention of probing structures further to understand their fundamental properties and the quality of data has now made it possible to see atomic orbitals.²

We have shown how it is possible to obtain a model or atomic skeleton from X-ray diffraction in a previous section of this thesis. Areas of high electron density correspond to that of an atomic nucleus, and are treated as spherical in shape. This is a very simplistic model and with the advancement in apparatus and techniques such as low temperature devices and intense X-ray sources such as synchrotrons it is becoming easier to obtain electron density with more information about the structure and as such it is possible to model electron density in the valence shells using an aspherical model.

The aim of this project was to develop station 9.8 at the SRS so that charge density could become more accessible to more users as a routine experiment and as such I will

be focusing mainly on work done using these X-ray sources, a brief synopsis of charge density experiments performed on synchrotrons is available.³

Synchrotrons have some advantages over traditional X-ray sources which make them suitable for high resolution charge density type experiments for example, a wide range of X-ray energies can be selected and so that a short harder wavelength can be selected such as Ag (0.4\AA) this property helps to reduce systematic errors such as absorption and extinction. The high flux from the synchrotron ensure that smaller crystals can be collected whilst reducing the time required to collect the data it is now possible to collect a high resolution data set in less than a day¹ whereas on the older in-house facilities it was expected to take several weeks to obtain sufficient data for a full refinement. The monochromatic nature of the radiation eliminates the problem of α_1 - α_2 splitting. With the advantages of synchrotrons for charge density studies (C.D.) there are some disadvantages such as the beam decays with time and therefore is not constant throughout the day. A program BEAMISH was created to adjust the data accordingly as it uses a database of known beam current at the SRS and corrects for the decay. Synchrotrons also tend to be heavily over subscribed, and even with fast data collection times it is usual to only get a couple of days on a beamline, as such only a few data sets can be collected. The station also might not be fully equipped such as not having a low temperature device suitable for C.D. studies.

The first high resolution dataset on a synchrotron was not collected until 1986 when Nielsen *et al*⁴ managed to obtain a high resolution electron density study on

$\text{Cr}(\text{NH}_3)_6\text{Cr}(\text{CN})_6$ using a Huber 512 diffractometer over 9 days. This collection time was soon improved upon with the advent of CCD area detectors as Darovsky *et al*⁵ managed to get a full data collection in just 2 days. Further improvements are being reported continually and with advancement of technology means a high resolution data collection can now be performed under 1 day¹. The fastest reported data collection from a synchrotron was achieved in less than 2 hours with a study of magnesium formate dehydrate,⁶ this was achieved by using a wavelength of 2.2Å from the ESRF (Grenoble). These fast collections help to reduce any affects of beam fluctuations. Even with these advantages over lab sources there have been cases reported whereby the synchrotron data was not producing the same accuracy of data⁷ as a conventional X-ray source. However, work by Iversen *et al*⁸ has shown that synchrotrons can be as good as conventional X-ray sources so clearly this is dependent on the size and quality of the crystal as to whether an conventional lab source or synchrotron is used.

With this technique becoming more routine why are people interested in collecting these kinds of data sets?

Some groups are interested in the theoretical aspect of charge density i.e. to push the limits of what information crystallographers can get from a crystal. Work by Destro *et al*⁹ questions whether there is a real gain in using high quality by examining two crystals of the fungal metabolite citrin, one being of high quality whilst the other being much lower. Dittrich and co workers are interested in amino acids¹⁰ and are using high resolution X-ray data to improve their understanding of the many amino acids. With these data sets it is possible to partition a molecular structure into its functional groups and discrete molecular regions and the information obtained can be used in a

database^{11,12} which can be employed on more complicated systems such as proteins^{13,14} with a view to probing the charges and properties of the proteins so that we may understand their biological function.

The aim of this thesis was to use these techniques to try and examine crystallised ionic liquids and ionothermally prepared zeotypes to investigate the interesting properties of ionic liquid synthesis as previously described in chapter 1. Many different frameworks can be synthesised from the same ionic liquid with only a few subtle changes and we want to know if it is possible to examine ionic liquids with high resolution X-ray diffraction and see if their properties/charge density change when encapsulated within a framework. This is particularly important as the type of interaction the guest has on the host can drastically affect the properties of the framework as shown by Loiseau *et al*¹⁵ who used NMR studies to show how strong hydrogen bonding between a water molecule and Al(MIL-53) caused a change in cell parameters from 16.675(3) x 12.813(2) Å for the calcined version to 19.513(2)x 7.612(1) Å. There have only been a few examples of high resolution studies being carried out on zeotypes and this is due to the complexity of the frameworks and the poor crystals which usually result. Work by Poulsen^{16,17} and Claussen¹⁸ have shown that it is possible to get accurate charge density models with a view to understanding the properties of metal organic frameworks such as magnetic susceptibility. Whilst Aubert¹⁹ *et al* have shown that it is also possible to get a good data set from the aluminium phosphate AlPO₄-15 on which they investigated the electrostatic potential.²⁰

Organic molecules are the most dominant in charge density studies. This is mainly due to their relative light elements. Heavier element compounds are experimentally and theoretically more complicated and as such need more precise data. The heavier an element the smaller the fraction of scattering stemming from the valence electrons relatively to the core contribution. Stevens *et al*²¹ proposed a suitability factor which indicated the suitability for charge density.

$$S = \frac{V_{unitcell}}{\sum (N_{core}^2)}$$

N_{core} is the number of core electrons of each of the atoms. The higher the suitability factor S the more suited it is for these kind of experiments.

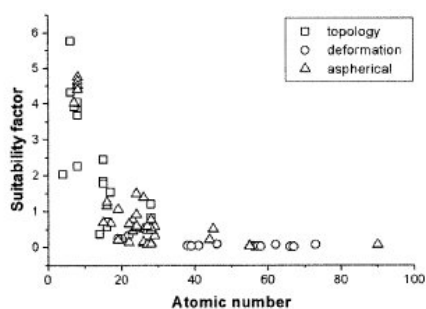


Figure 5.1: The suitability factors for a selection of recent X-ray charge density studies plotted against atomic number of the heaviest element in the structure.²² Even with the suitability factor it is still possible to study samples with as heavy atoms as thorium ($Z = 90$).

5.1.1 Quality of data

The quality of data from a charge density experiment has to be of a higher standard than normal as we are trying to fit all the individual electrons. There are certain criteria that have to be met to try and obtain data of high quality: A single crystal which diffracts well with minimal disorder is highly advantageous (however, this can be solved some of the time by using a low temperature device to lower the thermal motion of the crystal); The use of an intense X-ray source so that the weak high angle reflections can be collected. A short wavelength ($\sim 0.4 \text{ \AA}$) to minimise absorption and extinction and as large a crystal as possible to maximise the diffracted intensities, this can lead to absorption problems, as we are mainly looking at zeotypes this will not be a problem. A high redundancy is also advisable so that good reliability is achieved.

Charge density studies require long data collection times to ensure all the weak reflections are measured accurately. However, it has been shown that X-rays can damage single crystals with time. This usually happens during the longer collections (i.e. days) of proteins and not typically small molecules. Nevertheless, lowering the temperature of the crystal can help reduce this radiation damage as it helps to slow down the diffusion through the lattice and prevent the generation of X-ray radicals.²³ The most useful and applicable application of low temperature for small molecules is the reduction of thermal motion which can lead to dynamic disorder, a problem typically experienced by spherical anions such as PF_6^- , and helps to reduce the smearing of the electrons²⁴ helping to identify small features such as hydrogen atoms and the location of lone pairs.

Most of these problems and needs have been solved by using station 9.8^{25,26} at the SRS Daresbury, as it provides an intense source of X-rays which is tuneable to obtain the required wavelength (Ag in most of the cases), it is well equipped with a Bruker-Nonius APEXII CCD area detector and D8 diffractometer with a low temperature (n-Helix) device so data collections of 28 K are achievable.

5.1.2 Experimental electron density

Table 5.1 and *Table 5.2* show the data strategies for that of silver (0.4861 Å) and zirconium (0.6703 Å) edge respectively. For the silver edge experiment we were able to sort the runs into 3 batches where 2θ was 0° , 30° and 60° . Data collection at $2\theta=90^\circ$ was attempted. However, due to the positioning of the n-Helix there was a lot of ice build up (*Figure 5.3*) on the detector and as such the data was being affected (diffraction from the ice was visible on the detector). The high angle data i.e. that at 60° is weaker in comparison to the other angles and as such a slightly longer collection time of 2 sec a frame was used to try and ensure as strong as possible reflections were obtained. Data collections at $2\theta=90^\circ$ had to be collected to try and get the same amount of redundancy obtained for the silver edge.

Table 5.1: Data strategy for use with Ag (0.4765Å) radiation

Operation	Active	Distance (mm)	2Theta (deg)	Omega (deg)	Phi (deg)	Chi (deg)	Time (sec)	Width (deg)	Sweep (deg)	Direction
Omega Scan	Yes	55	-60	-55	0	54.74	2	Default	190	negative
Omega Scan	Yes	55	-60	-55	120	54.74	2	Default	190	negative
Omega Scan	Yes	55	-60	-55	240	54.74	2	Default	190	negative
Omega Scan	Yes	55	-60	-55	60	54.74	2	Default	190	negative
Omega Scan	Yes	55	-60	-55	180	54.74	2	Default	190	negative
Omega Scan	Yes	55	-60	-55	300	54.74	2	Default	190	negative
Omega Scan	Yes	55	-30	-30	0	54.74	1	Default	180	negative
Omega Scan	Yes	55	-30	-30	120	54.74	1	Default	180	negative
Omega Scan	Yes	55	-30	-30	240	54.74	1	Default	180	negative
Omega Scan	Yes	55	-30	-30	60	54.74	1	Default	180	negative
Omega Scan	Yes	55	-30	-30	180	54.74	1	Default	180	negative
Omega Scan	Yes	55	-30	-30	300	54.74	1	Default	180	negative
Omega Scan	Yes	55	0	0	0	54.74	1	Default	180	negative
Omega Scan	Yes	55	0	0	120	54.74	1	Default	180	negative
Omega Scan	Yes	55	0	0	240	54.74	1	Default	180	negative

Table 5.2: Data strategy for using with Zr (0.6703Å) radiation

Operation	Active	Distance (mm)	2Theta (deg)	Omega (deg)	Phi (deg)	Chi (deg)	Time (sec)	Width (deg)	Sweep (deg)	Direction
Omega Scan	Yes	55	-90	-85	0	54.74	2	default	190	negative
Omega Scan	Yes	55	-90	-85	120	54.74	2	default	190	negative
Omega Scan	Yes	55	-90	-85	240	54.74	2	default	190	negative
Omega Scan	Yes	55	-60	-55	0	54.74	1	default	190	negative
Omega Scan	Yes	55	-60	-55	120	54.74	1	default	190	negative
Omega Scan	Yes	55	-60	-55	240	54.74	1	default	190	negative
Omega Scan	Yes	55	-30	-30	0	54.74	1	default	180	negative
Omega Scan	Yes	55	-30	-30	120	54.74	1	default	180	negative
Omega Scan	Yes	55	-30	-30	240	54.74	1	default	180	negative
Omega Scan	Yes	55	-30	-30	60	54.74	1	default	180	negative
Omega Scan	Yes	55	-30	-30	180	54.74	1	default	180	negative
Omega Scan	Yes	55	-30	-30	300	54.74	1	default	180	negative

5.1.3 Experimental Problems

There are a lot of problems associated with these types of experiment partly due to the prolonged periods of time the crystal is exposed to X-rays and the harsh conditions required to obtain suitable data. Below are some figures which depict the problems experienced by the ultra low temperatures used. *Figure 5.2* shows how the goniometer head iced up within minutes, this was corrected for by using a 100% copper pin to hold the crystal in place as it provided a more efficient heat transfer from the heated motors. *Figure 5.3* shows how the detector can also ice up due to the long periods of time with which the helium gas is running over the detector severely affecting the detector and therefore high angle data sets are more difficult to achieve.

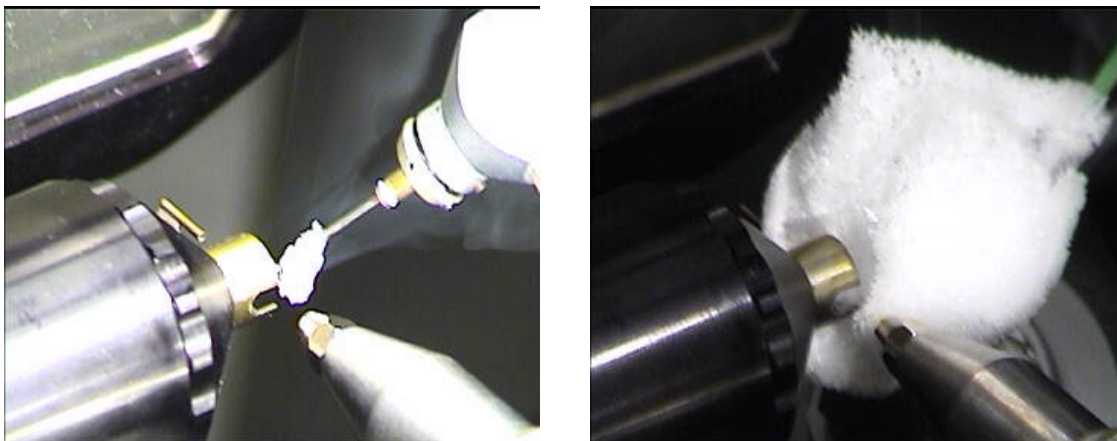


Figure 5.2: Icing on the crystal can affect the data and was resolved by using a 100% copper pip.

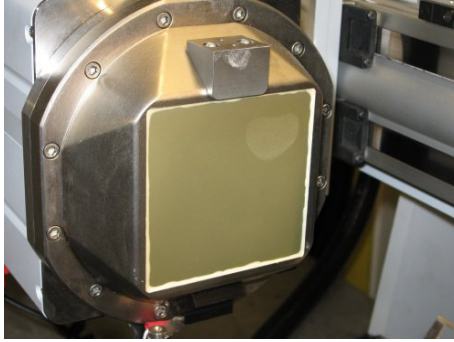


Figure 5.3: Icing on the detector can affect the data

5.1.4 Multipole model

Once an accurate data collection has been obtained it is important to try and fit a suitable aspherical model to the data, this can be done by using a multipole model as proposed by Hansen-Coppens²⁷(3.1) and incorporated in the XD 2006 software²⁸

$$\rho_{atom}(r) = \rho_{core}(r) + P_v k^3 \rho_v(kr) + \sum_{l=0}^{l_{max}} k^l R_l(k'r) \sum_{m=0}^l P_{lmp} Y_{lmp}(\theta, \phi) \quad (3.1)$$

where $\rho_{core}(r)$ and $\rho_v(r)$ correspond respectively to spherically averaged Hartree-Fock core and valence electron densities for isolated atoms. P_v and P_{lmp} are the valence and

multipole populations, κ and κ' are expansion/contraction parameters k , R_l are Slater type radial functions, and $y_{lm p}$ are spherical harmonic functions in the real form

The atomic core ρ_{core} is commonly fixed assuming no perturbation occurs due to the chemical bonding.

5.1.5 Processing

One of the most difficult aspects of charge density studies is the processing of the final data as subtle changes can often have a profound effect and there is no exact methodology. However herein I will describe the fundamentals of processing a data set which resulted in a good multipole model and is a good basis for further datasets.

Once a full data set has been collected saint and SADABS07 are employed to integrate and scale the reflections. A quick integration and scale is performed to indicate the quality of data and any datasets with exceptionally high Rint values can be discarded from the integration process. After all the poor datasets have been removed XPREP is called to process the data by applying suitable cut-off values usually cutting data as close to 0.5 Å whilst merging friedel pairs and outputting the data in shelx format. The structure is solved and refined as described previously using SHELXS and SHELXL²⁹ software with non-hydrogen atoms refined anisotropically and hydrogen atoms added geometrically. After a suitable R factor is achieved the instruction (.ins) and the reflection file (hkl) are renamed shelx.ins and shelx.hkl for the benefit of the XD2006 software. The program XDINI is run on these two files to produce a series of files

including an xd instruction file (xd.mas) where the multipole models and topological analysis can be applied. The X-H distances are set to that of neutron data using SHADE³⁰ and the hydrogen atom coordinates are fixed. The non-hydrogen atoms are refined using the multipole least squares model gradually incrementing the multipole from monopole up to hexadecapole until no visible improvement is achieved. The multipole model is allowed to expand and contract as described by Hansen-Coppens²⁷ and as such a kappa parameter is assigned to each independent atomic environment for refinement.

A good model should result in a lower R factor than that given from the independent atom model (iam) as more variables are being refined. The structures examined with this technique throughout this thesis have varied in atomic mass. However, all of the systems have consisted of relatively heavy elements resulting in lower than expected improvements in R factors. This is primarily due to the heavier the element the smaller the scattering by the valence electrons relative to the core contribution.

5.1.6 Analysis

Once a full least squares refinement has been achieved it is necessary to check the quality of the data and this is achieved by looking at the residual electron density and the deformation density which should show whether a good model has been obtained. A residual map is calculated by subtracting the multipole structure factor from the observed structure factor (equation 3.2), which could not be modelled. Ideally this is flat

and featureless. However, this is not always the case as there is still sometimes electron density which cannot be modelled.

$$\delta\rho^{res}(\mathbf{r}) = \frac{1}{V} \sum_{\mathbf{h}} [|F_o(\mathbf{h})| - |F_{mul}(\mathbf{h})|] e^{i\phi_{sph}} e^{-2\pi i \mathbf{h} \cdot \mathbf{r}} \quad (3.2)$$

Deformation density maps are another way of checking the quality of the data as it will highlight any anomalies. In such a map the areas of high electron density at the atomic core are removed to locate the areas of interest from the valence electrons. These maps can be used to highlight lone pairs and the electron density present in the bonds. The atomic positions have the largest area of electron density in the model, which makes it difficult to locate other areas of interest, as such we can remove these areas of high electron density to reveal the interesting chemistry of the model (equation 3.3).

$$\delta\rho^{exp}(\mathbf{r}) = \frac{1}{V} \sum_{\mathbf{h}} [|F_o(\mathbf{h})| e^{i\phi_{mul}} - |F_{sph}(\mathbf{h})| e^{i\phi_{sph}}] e^{-2\pi i \mathbf{h} \cdot \mathbf{r}} \quad (3.3)$$

Figure 5.4 shows some of the features that we can obtain from these maps such as the bond regions and lone pair regions.

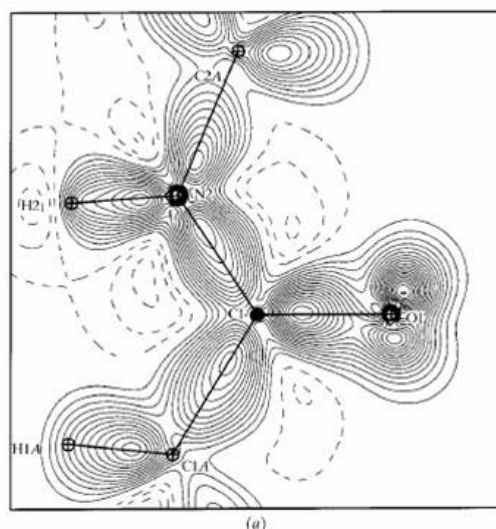


Figure 5.4: Deformation density map of DL-alanyl-methionine³¹ with lone pair on the oxygen clearly visible.

5.1.7 Atoms in molecules

Once a structure has been successfully modelled various chemical and physical properties can be derived. XDPROP²⁸ can be called upon to perform topological analysis on the structure and provides a quantitative link between the total electron density and the important physical properties of a molecule.

One of the most important features in the topology of charge density is the occurrence of local maxima at the position of the nuclei as a consequence of the interaction of the electronic density and the nuclei. These maxima are known as critical points and occur at the point when the first derivatives of the density are equal to zero (equation 3.4) and the curvatures of the density in all directions are negative. The gradient vector of the density in the Cartesian coordinate system is $\hat{i}, \hat{j}, \hat{k}$ defined as

$$\nabla\rho(\mathbf{r}_c) = \hat{i} \frac{\delta p}{\delta x} + \hat{j} \frac{\delta p}{\delta y} + \hat{k} \frac{\delta p}{\delta z} = 0 \quad (3.4)$$

The Hessian matrix (the 3x3 ordered array of the second derivative of ρ (equation 3.5))³² is defined as a symmetric matrix of the nine second derivatives with the eigenvectors of the matrix obtained by diagonalization of the matrix to give a new coordinate axes called the principal axes of the curvature. The corresponding eigenvalues ($\lambda_1, \lambda_2, \lambda_3$) are the curvature along the principle axes and are used to define the Laplacian $\nabla^2\rho = \lambda_1 + \lambda_2 + \lambda_3$. The ratio of the eigenvalues ($\epsilon = (\lambda_2/\lambda_1) - 1$) measures the degree of conjugation.

$$\nabla\nabla\rho = \begin{pmatrix} \frac{\delta^2 p}{\delta x^2} & \frac{\delta^2 p}{\delta x \delta y} & \frac{\delta^2 p}{\delta x \delta z} \\ \frac{\delta^2 p}{\delta y \delta x} & \frac{\delta^2 p}{\delta y^2} & \frac{\delta^2 p}{\delta y \delta z} \\ \frac{\delta^2 p}{\delta z \delta x} & \frac{\delta^2 p}{\delta z \delta y} & \frac{\delta^2 p}{\delta z^2} \end{pmatrix} \quad (3.5)$$

The rank (ω) of the curvature at a critical point is equal to the number of nonzero eigenvalues whilst the signature (σ) is the sum of the signs of principal curvatures of ρ . A critical point is labelled by the pair of values (ω, σ) of which there are four possible points (*Table 5.3*) which can be used to describe bonding in a molecule.

Table 5.3: The four possible critical points

(3,+3)	Cage Critical point	All curvatures are positive and ρ is a local minimum at \mathbf{r}_c
(3,+1)	Ring Critical point	Two curvatures are positive and ρ is a minimum at \mathbf{r}_c in the plane defined by their corresponding axes ρ is a maximum at \mathbf{r}_c along the third axis, perpendicular to this plane
(3,-1)	Bond Critical point	Two curvatures are negative and ρ is a maximum at \mathbf{r}_c in the plane defined by their corresponding axes ρ is a minimum at \mathbf{r}_c along the third axis, perpendicular to this plane
(3,-3)	(Non) nuclear attractor	All curvatures are negative and ρ is a local maximum at \mathbf{r}_c

5.1.8 Gradient vector

The gradient vector is useful in the tracing of the trajectories of the vector $(\nabla\rho)$ and points in the direction of the greatest increase in ρ with these trajectories pointing perpendicular to the contour lines of ρ , they terminate or originate at critical points in ρ . The critical point (3,-1) is known as the bond critical point and arises from the gradient paths which originate at each (3,-1) critical point and terminate at the nuclei, they define a line through the charge distribution linking the neighbouring nuclei showing there is an accumulation of charge between bonded nuclei. This is the topological definition of a chemical bond.

5.1.9 The Laplacian of Charge density

The Laplacian determines the regions of space wherein electronic charge is concentrated and depleted and can be used to locate electrophilic and nucleophilic nature of atoms. It is a scalar derivative of the gradient vector field of the electron density as is denoted as $\nabla^2\rho$ and it is used to determine where electronic charge is concentrated $\nabla^2\rho < 0$ or depleted $\nabla^2\rho > 0$ and works complementarily to the information obtained from the electron density. It is useful in the study of nucleophilic and electrophilic attack and helps to predict preferred sites of protonation.

5.1.10 References

- ¹ T. Koritsanszky, R. Flaig, D. Zobel, H. Krane, W. Morgenroth, and P. Luger, *Science.*, 1998, **279**, 356-358
- ² J.M. Zuo, M.Kim, M.O’Keeffe and J.C.H Spence, *Nature*, 1999, **40**, 49-52
- ³ P.R. Mallinson, G. Barr, S.J. Coles, T.N. Guru Row D. D. MacNicol, S.J. Teat and K. Woźniak, *J. Synchrotron Rad.*, 2000, **7**, 160-166.
- ⁴ F.S. Nielsen, P. Lee and P. Coppens. *Acta Cryst B.*, 1986, **42**, 359-364
- ⁵ R. Bolotovskiy, A. Darovsky, V. Kezerashvili and P.Coppens, *J. Synchrotron Rad.*, 1995, **2**, 181-184
- ⁶ H. Graafsma, S.O Svensson and Å. Kvik, *J. Appl. Cryst.*, 1997. **30**, 957-962
- ⁷ L.J. Farrugia, P.R. Mallinson, and B. Stewart, *Acta Cryst B.*, 2003, **59**, 234-247
- ⁸ B.B. Inversen, F.K. Larsen, A.A. Pinkerton, A. Martin, A. Darovsky and P.A Reynolds, *Acta Cryst B.*, 1999, **5**, 363-374.
- ⁹ R.Destro, L. Loconte, L.L. Presti, P. Roversi, and R. Soave, *Acta Cryst A.*, 2004, **60**, 365-370
- ¹⁰ B. Dittrich, P. Munshi, and M.A. Spackman, *Acta Cryst B.*, 2007, **63**, 505-509
- ¹¹ B. Dittrich, C.B. Hübschle, P. Luger and M.A. Spackman, *Acta Cryst D.*, 2006, **62**, 1325-1335.
- ¹² V. Pichon-Pesme, C. Lecomte and H. Lachekar, *J. Phys. Chem.*, 1995, **99**, 6242-6250
- ¹³ R. Kalinowski, B. Dittrich, C.B. Hübschle, C. Paulmann and P. Luger, *Acta Cryst B.*, 2007, **63**, 753-767

- ¹⁴ D. Housset, F. Benabicha, V. Pichon-Pseme, C. Jelsch, A. Maierhofer, S. David, J.C. Fontecilla-Camps and C. Lecomte, *Acta Cryst D.*, 2000, **56**, 151-160.
- ¹⁵ T. Loiseau, C. Serre, C. Huguenard, G. Fink, F. Taulelle, M. Henry, T. Bataille and G. Férey, *Chem.Eur.J.*, 2004, **10**, 1373-1382
- ¹⁶ R.D. Poulsen, A. Bentien, T. Graber, and B.B Iversen, *Acta Cryst A.*, 2004, **60**, 382-389
- ¹⁷ R.D. Poulsen, A. Bentien, M. Chevalier and B.B Iversen, *J. Am. Chem. Soc.*, 2005,**127**, 9156-9166
- ¹⁸ H.F. Clausen, J.Overgaard, Y.S. Chen and B.B. Iversen, *J. Am. Chem. Soc.*, 2008, **130**, 7988-7996
- ¹⁹ E. Aubert, F. Porcher, M. Souchassou, and C Lecomte. *Acta Cryst B.*, 2003, **59**, 687-700
- ²⁰ E. Aubert, F. Porcher, M. Souchassou, and C Lecomte. *J. Phys. Chem. Solids.*, 2004, **65**, 1943.
- ²¹ E.D. Stevens and P.Coppens, *Acta Cryst A.*, 1976, **32**, 915
- ²² B.Schiøtt, J. Overgaard, F. K. Larsen and B.B Iversen, *Int. J. Quantum Chemistry.*, 2004, **96**, 23-31
- ²³ W. P. Burmeister, *Acta Crystallogr. Sect. D.*, **56**, 2000, 328
- ²⁴ A.E. Goeta and J.A.K. Howard, *Chem.Soc.Rev.*, 2004, **33**,490-500
- ²⁵ R.J. Cernik, W. Clegg, C.R.A Catlow, G. Bushnell-Wye, J.V. Flaherty, G.N. Greaves, I. Burrows, D.J. Taylor, S.J. Teat and M. Hamichi, *J. Synchrotron Rad.*, 1997, **4**, 279.

- ²⁶ W. Clegg, M.R.J. Elsegood, S.J. Teat, C. Redshaw and V.C. Gibson, *J.Chem.Soc., Dalton Trans.*, 1998, 3037.
- ²⁷ N. K Hansen and P. Coppens, *Acta Cryst A.*, 1978 **34**, 909
- ²⁸ XD2006 - a computer program for multipole refinement, topological analysis of charge densities and evaluation of intermolecular energies from experimental or theoretical structure factors. A. Volkov, P. Macchi, L. J. Farrugia, C. Gatti, P. Mallinson, T. Richter, T. Koritsanszky, 2006
- ²⁹ G.M. Sheldrick, *Acta Cryst A.*, 2008, **64**,112-122
- ³⁰ A. Ø. Madsen, *J.Appl. Cryst.*, 2006, **39**, 757-758
- ³¹ R. Guillot, N. Muzet, S. Dahaoui, C. Lecomte and C. Jelsch, *Acta Cryst B.*, 2001, **57**,567-578
- ³² P. Popelier, 'Atoms in Molecules', Pearson Education, 2000, 73

5.2 High Resolution X-ray Diffraction Studies of a Crystallised Ionic Liquid and a Metal Organic Framework.

5.2.1 Introduction

Ionic liquids (ILs) are compounds that in general have melting points near room temperature (below 100°C is a typical definition), and contain an asymmetric, often large bulky cation in combination with one of many different anions. The particular properties of ILs, including negligible vapour pressure, good thermal stability, safe toxicology and good solvating power, has led to a great deal of interest as “green” alternatives to organic solvents in homogenous catalyst etc. Recently ILs have also been of interest as both solvent and structure directing agent in the synthesis of crystalline solids – so called ionothermal synthesis¹. A typical ionothermal synthesis involves reactants being mixed with a solvent/template (ionic liquid) and heated to varying temperatures in a Teflon lined autoclave for a given period of time. The autoclave is then removed from the oven and cooled to room temperature, the product filtered, washed with water and dried.

Many of the unusual properties of ionic liquids are intimately connected with their molecular and intermolecular structures. There have therefore been many experimental and theoretical studies of IL structures and these reveal many interesting thermodynamic and structural features.^{2,3,4}

When an IL or indeed any template is acting to template an inorganic material one important characteristic is the charge density distribution in the molecule. This feature controls the specific electrostatic interaction between the IL templating cation and the growing framework material as it forms around the template. Charge density matching is important for the successful synthesis of interesting materials.^{5,6,7,8} Synthetic preparations where the charge density of the template and the target framework are mismatched tend to produce very little in the way of interesting materials, unless a supplementary template with an improved charge density match is subsequently added⁹. A good knowledge of how electrons are distributed in the ILs is therefore an important piece of information that may help to improve our knowledge of the templating process that occurs during the ionothermal synthetic process. Another key interaction in framework synthesis is that of hydrogen bonding which is an important organising force due to its directional and selective bond formation.¹⁰ Lin and co-workers¹¹ show how hydrogen bonding is important in aligning and controlling the formation of 3D networks that are derived from ionic liquids.

Many earlier force field calculations² failed to predict that hydrogen bonding existed between the anion and the cation of many ionic liquids. However as the models improved it has been possible to show that monoatomic anions (halides) form one hydrogen bond with the cation, whilst the molecular anions (hexafluorophosphate) form multiple hydrogen bonds.³ The existence of hydrogen bonds in 1-Ethyl-3-methylimidazolium hexafluoro-phosphate was confirmed by Fuller *et al.*²⁸ However, only the acidic hydrogen could be located (H5A) similar to other studies on EMIm

structures,^{3,12} with the other potential hydrogen bond distances considered too close to the van der Waals radii to be true (2.7Å). Which are based on the criteria that hydrogen bond (Y-H...X) distances must be less than the sum of the H and X van der Waals radii, and the angle (Y-H...X) must be greater than 90°. Taking the van der Waals radii to be 1.20 and 1.50 Å for hydrogen and fluorine, respectively, the C-H...F distances less than 2.70 Å are indicative of hydrogen bonding.

The development of ionic liquids in the production of MOFs^{13,14,15,16} is providing an exciting route not only due to its dual role of solvent and template but also in the fact that they are known as “designer solvents” due to their flexibility and tailorability making them suitable for charge matching.

As already discussed in chapter 1 metal organic frameworks (MOFs) are extremely interesting materials thanks to their flexibility and adaptability making them suitable for a wide range of applications such as catalysis and gas storage.^{17,18,19,20,21} With so many applications it is important to understand the synthesis process so that they can be tailored for specific roles. Charge matching between template and framework has a great influence on the framework synthesis and as such we need to understand how subtle differences can result in different frameworks, if we can understand the interactions the template has on the framework it may be possible to control the templates in a specific way to obtain desired frameworks.

Metal organic frameworks are extremely complicated structures to examine using standard single crystal X-ray diffraction techniques and therefore are not the best to examine at high resolution. This is due to their extended nature but also because they contain heavy metals which are difficult to model with the current software available. However, work by Poulsen^{22,23} and Claussen²⁴ have shown that it is possible to get accurate charge density models from these types of materials with a view to understanding their properties such as magnetic susceptibility.

5.3.1 High Resolution X-ray diffraction study of 1-Ethyl-3-methylimidazolium hexafluorophosphate, a crystallised ionic liquid

The aim of this section is to examine the ionic liquid 1-Ethyl-3-methylimidazolium hexafluorophosphate experimentally to get a greater insight into these types of materials in the solid phase instead of relying on computer simulations, which work in the gas phase.

The ionic liquid most used in our synthesis process has been that of 1-ethyl-3-methylimidazolium bromide. However, this is a very hygroscopic material and can lose its crystallinity very quickly when exposed to air. It was therefore necessary to ion exchange the Br anion with hexafluorophosphate to produce good quality crystals which are stable in the atmosphere enabling easy handling.

5.3.2 Experimental

The ionic liquid 1-ethyl 3-methyl imidazolium bromide (EMIm) was prepared as described previously,²⁵ degassed ethylbromide (88.25g, 0.81mol) was added to ice cooled 1- methylimidazole (46.979g, 0.57mol) with constant stirring, the mixture was then heated under reflux for 3 hours at 40°C and allowed to cool to room temperature. Ethyl acetate was added to enable the product to crash out, which was then filtered quickly and washed with ethyl acetate and dried under vacuum to give a white solid (1-ethyl-3-methylimidazolium bromide). The salt was prepared by dissolving EMIm (6.8g) in H₂O (12mL) and hexafluorophosphate (8mL) the solution was allowed to cool to room temperature for 3 hours and the resulting solid filtered. The salt was recrystallised from methanol and the crystals filtered, and then dried in a desiccator.

5.3.3 The structure of 1 -Ethyl-3-methylimidazolium hexafluorophosphate.

A standard data collection was performed on the high flux station 9.8^{26,27} at the Synchrotron Radiation Source (SRS), Daresbury laboratory to ascertain the quality of the crystal and compared with the previously reported structure by Fuller *et al*²⁸ to confirm the phase. Once a suitable crystal had been located the temperature was lowered to 30K using an Oxford Cryosystems n-Helix as this helped to reduce the thermal motion of the atoms in the crystal. The X-ray wavelength was fixed to 0.475Å.

The structure of EMIm PF₆ consists of an imidazolium cation with a methyl attached to one of the nitrogen groups (N4) and an ethyl group attached to the other (N3). There is an acidic hydrogen (H5A) which is stabilised by the carbene, the counter anion is a hexafluorophosphate. *Figure 5.1* shows the molecular structure of the ionic liquid

which can be collected from the standard data set and the packing diagram of the material is depicted in *Figure 5.2* from which it is possible to see the double bilayer nature of the material as described by Bradley *et al.*²⁹

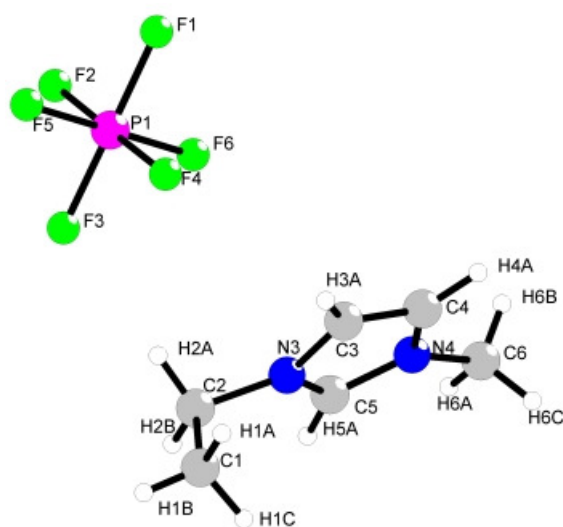


Figure 5.1: Molecular Structure of 1-Ethyl-3-methylimidazolium hexafluorophosphate

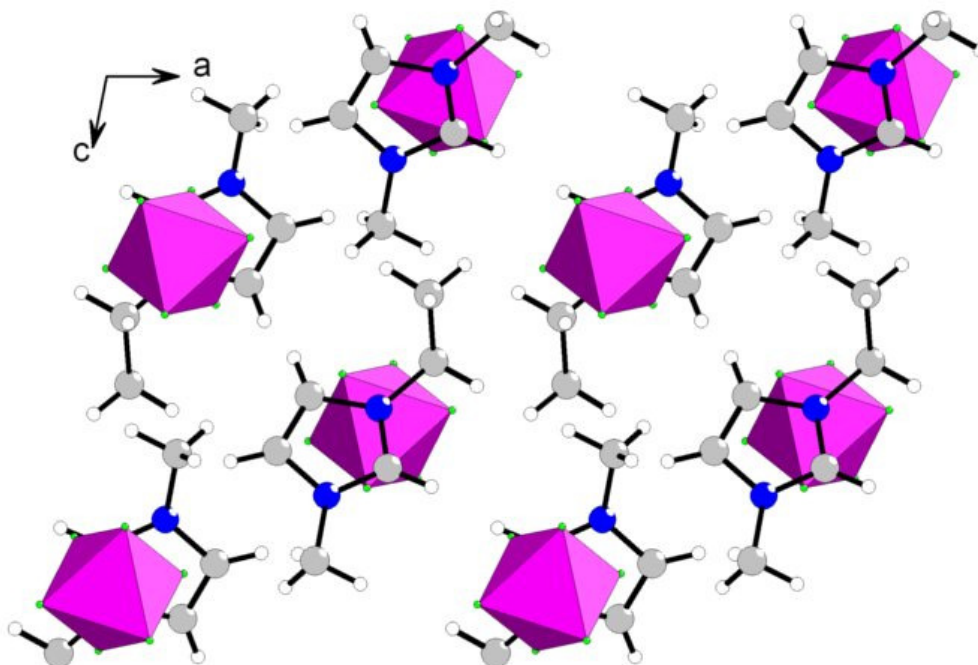


Figure 5.2: Packed structure of 1-Ethyl-3-methylimidazolium hexafluorophosphate with the PF_6^- anion drawn as a polyhedron for clarity.

5.3.4 Data Collection and Processing Strategy

One of the most important steps in obtaining a good multipolar model is a thorough data strategy which ensures high redundancy and lots of good quality high angle data. *Table 5.1* shows the data strategy used for this data collection, which took approx half a day to complete. The data collection utilises an omega scan which starts at -55° and collects data during a 190° and 180° sweep for the high angle and low angle data respectively, distance is a measure of the detector to the sample and is set to 55mm for the entire experiment. A value of $2\theta=60^\circ$ was chosen as above this angle ice crystals began to form on the front of detector which affected the data collection.

Table 5.1: Data strategy for use with synchrotron radiation set at Ag edge (0.4765Å)

Operation	Active	Distance (mm)	2Theta (deg)	Omega (deg)	Phi (deg)	Chi (deg)	Time (sec)	Width (deg)	Sweep (deg)
Omega Scan	Yes	55	-60	-55	0	54.74	2	default	190
Omega Scan	Yes	55	-60	-55	120	54.74	2	default	190
Omega Scan	Yes	55	-60	-55	240	54.74	2	default	190
Omega Scan	Yes	55	-60	-55	60	54.74	2	default	190
Omega Scan	Yes	55	-60	-55	180	54.74	2	default	190
Omega Scan	Yes	55	-60	-55	300	54.74	2	default	190
Omega Scan	Yes	55	-30	-30	0	54.74	1	default	180
Omega Scan	Yes	55	-30	-30	120	54.74	1	default	180
Omega Scan	Yes	55	-30	-30	240	54.74	1	default	180
Omega Scan	Yes	55	-30	-30	60	54.74	1	default	180
Omega Scan	Yes	55	-30	-30	180	54.74	1	default	180
Omega Scan	Yes	55	-30	-30	300	54.74	1	default	180
Omega Scan	Yes	55	0	0	0	54.74	1	default	180
Omega Scan	Yes	55	0	0	120	54.74	1	default	180
Omega Scan	Yes	55	0	0	240	54.74	1	default	180

Once a full data set had been collected SAINT⁺³⁰ and SADABS07³¹ were employed to integrate and scale the reflections. A quick integration and scale was performed to indicate the quality of the data and shells of data with exceptionally high Rint values were discarded from the integration process. After all the poor shells had been removed Xprep was used to process the data, the data was subsequently cut at 0.48Å merging Friedel pairs and outputting the data in SHELX format. The structure was solved and refined as described previously using SHELXS and SHELXL,³² non-hydrogen atoms were anisotropically refined and hydrogen atoms added geometrically. After a suitable R factor was achieved the instruction (.ins) and the reflection (hkl) files were renamed shelx.ins and shelx.hkl for the benefit of the XD2006 software.³³ The program XDINI was run on these two files to produce a series of files including an xd instruction file (xd.mas) where the multipole models and topological analysis could be applied. The hydrogen atoms were placed using the SHADE³⁴ server which derives the atomic

positions from known neutron data experiments. The non-hydrogen atoms were then refined using the multipole least squares model gradually incrementing the multipole from monopole up to hexadecapole until no visible improvement is achieved. Expansion- contraction coefficients (k , k') were then assigned to each independent atomic environment for refinement with only k refined as refinement of k' caused divergence in the model. Hydrogen atoms were refined to only to bond-directed dipoles.

5.3.5 Residual electron density

A residual map is a good indicator that the model is of a reasonable fit and highlights the areas of electron density which have not been modelled. Figure 5.3 **a** is a residual map of the imidazolium ring before a full multipolar refinement had been carried out, from which it is clear to see the residual electron density cannot be modelled from a standard SHELXL refinement i.e. the electrons within the bonds are clearly visible. *Figure 5.3 b* depicts the imidazolium ring after the Hansen-Coppens model³⁵ has been applied and it is clear to see that the once visible electron bond density has now been modelled completely. There is still some electron density in the map and if this was an ideal case it would be flat. However, the map is featureless indicating a good model has been achieved. *Figure 5.4* is the residual map for the PF_6^- cation, again it is possible to see how residual electron density has been removed with the use of the Hansen-Coppens model³⁵. There is, however, a small amount of residue which can be attributed to the effect of the heavy phosphorus.

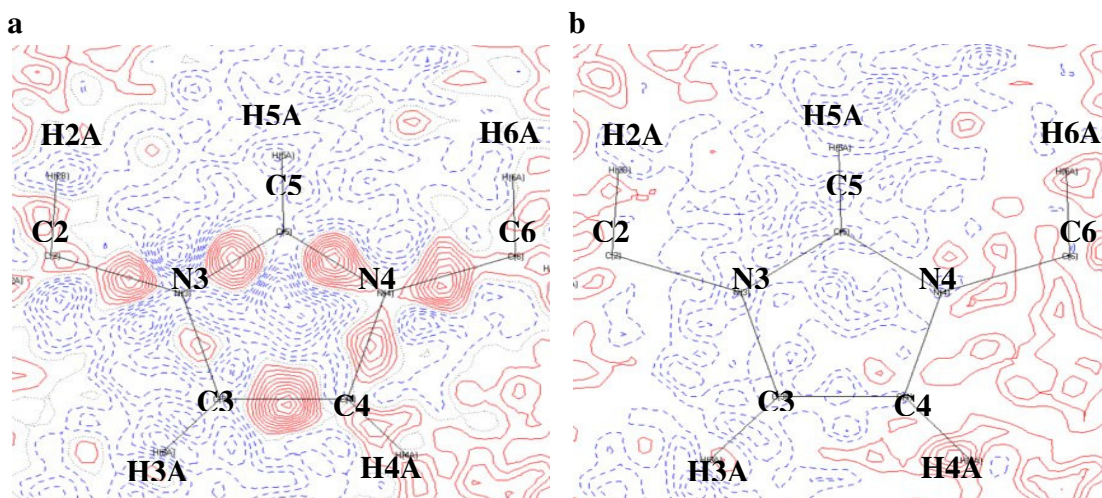


Figure 5.3: A residual map of imidazolium ring **a** before refinement with **b** being after the multipole model. The contour is at $0.05 \text{ e}\text{\AA}^{-3}$ with red indicating positive electron density and the blue indicating negative electron density.

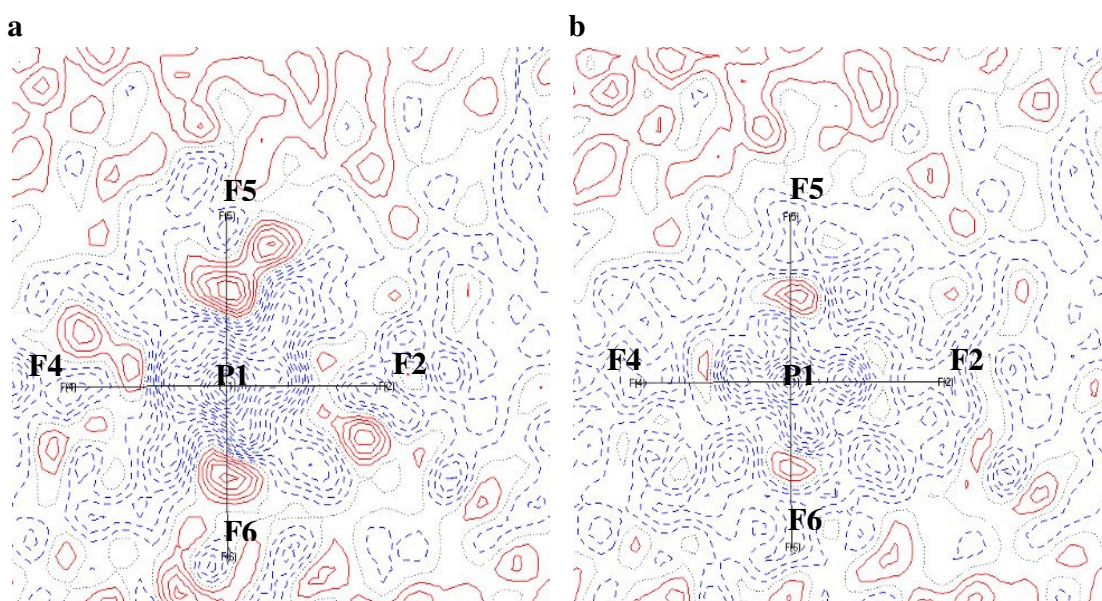


Figure 5.4: A residual map of PF_6^- **a** is before refinement with **b** after the multipole model. The contour level is set at $0.05 \text{ e}\text{\AA}^{-3}$ with red indicating positive electron density and the blue indicating negative electron density.

5.3.6 Deformation Density

Deformation density maps are another way of checking the quality of the data as it will highlight any anomalies. In such a map the areas of high electron density at the atomic core are removed to locate the areas of interest from the valence electrons. These maps can be used to highlight lone pairs and the electron density present in the bonds. *Figure 5.5* is the deformation density map for the imidazolium ring (**a**) and the PF_6^- anion (**b**). On inspection a good model has been achieved as the areas of electron density are as expected in the bonds, and there are no other areas of significant electron density.

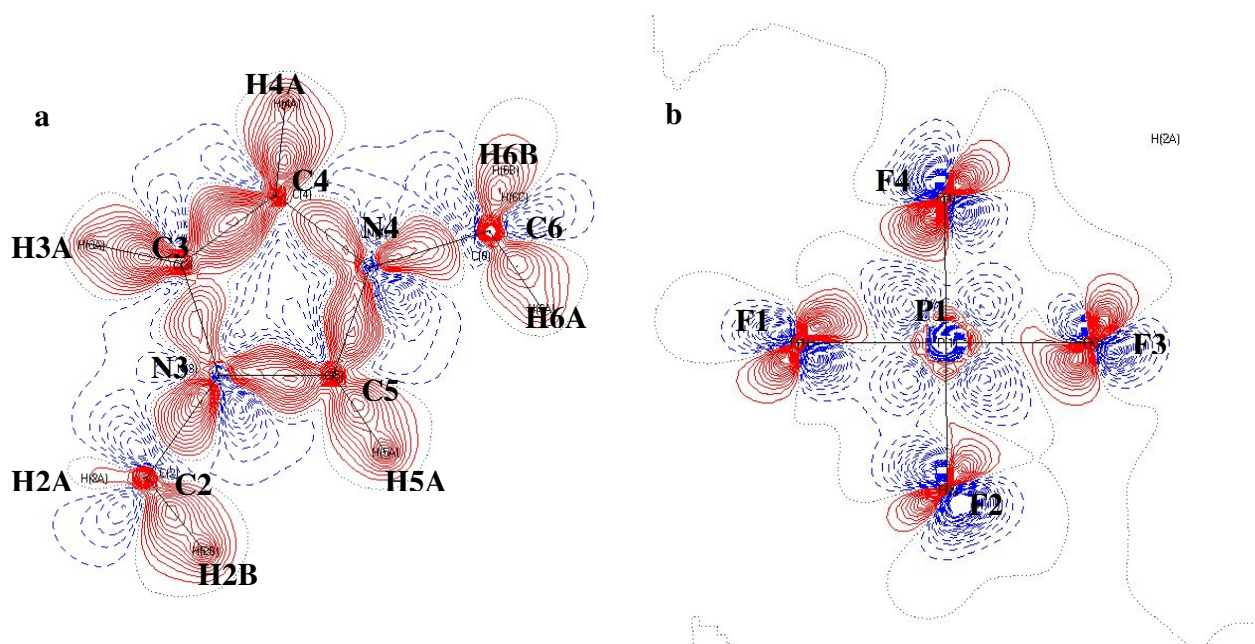


Figure 5.5: Deformation density map of the imidazolium ring (a), and the PF_6^- anion (b)

5.3.7 Topological features

Bader's theory of "atoms in molecules" (AIM)³⁶ provides a way to quantitatively examine the results from charge density experiments, by obtaining topological information about the system such as bond critical points. All the bond critical points (3,-1) and ellipticity values were calculated and are reported in Table 5.2. The bond critical point is the point of minimum overlap between two atoms and ellipticity (ϵ) is a measure of the amount of π bonding present in the structure, with a large ϵ indicating a large amount of π bonding and a value of $\epsilon=0$ indicating no π bonding. The critical points can be graphically located using trajectories (*Figure 5.7*) from which it is possible to see how close the bonding point sits relative to individual atoms.

Table 5.2: Information regarding all bond critical points (3,-1) for the ionic liquid 1-Ethyl-3-methylimidazolium hexafluorophosphate. ϵ is the ellipticity and is defined by $\epsilon = (\lambda_1 - \lambda_2) / \lambda_3$, d_{1+2} is the length of the bond path between the atoms, d_1 and d_2 are distances along bond paths from the BCP to the first and atom respectively.

Bond	ρ	$\nabla^2 \rho$	d_{1+2}	d_1	d_2	λ_1	λ_2	λ_3	ϵ
C(6)-N(4)	1.762	-16.275	1.4622	0.618	0.8442	-13.31	-12.99	10.03	0.02
C(5)-N(4)	2.439	-31.141	1.3333	0.5692	0.7641	-24.08	-18.19	11.13	0.32
C(4)-N(4)	1.99	-17.393	1.3841	0.5738	0.8102	-16.98	-12.2	11.79	0.39
C(5)-N(3)	2.427	-25.007	1.3335	0.5781	0.7554	-22.84	-15.99	13.82	0.43
C(3)-N(3)	1.994	-18.629	1.383	0.5804	0.8027	-16.37	-12.33	10.07	0.33
C(4)-C(3)	2.311	-24.693	1.3635	0.7183	0.6451	-19.13	-14.31	8.74	0.34
C(2)-N(3)	1.716	-16.88	1.4722	0.5848	0.8874	-13.09	-11.99	8.2	0.09
C(2)-C(1)	1.721	-15.224	1.5211	0.791	0.7301	-12.84	-10.95	8.57	0.17
P(1)-F(1)	0.998	5.201	1.6189	0.6606	0.9583	-9.92	-7.14	22.26	0.39
P(1)-F(2)	1.054	2.299	1.6173	0.6648	0.9525	-10.89	-7.04	20.23	0.55
P(1)-F(3)	1.02	5.92	1.6158	0.6569	0.9589	-9.93	-7.84	23.7	0.27
P(1)-F(4)	1.026	6.384	1.6043	0.6568	0.9474	-10.74	-6.77	23.89	0.59
P(1)-F(5)	1.118	4.841	1.6112	0.6566	0.9546	-10.42	-8.19	23.45	0.27
P(1)-F(6)	1.175	3.104	1.6111	0.6598	0.9513	-10.29	-8.2	21.6	0.25

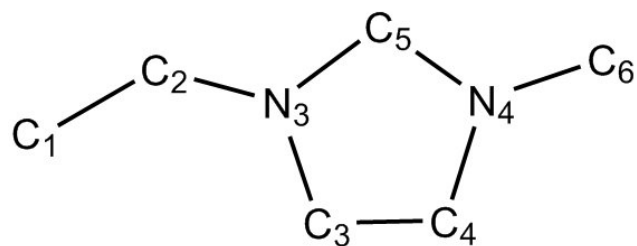


Figure 5.6: Numbering scheme of the imidazolium ring

Ellipticity results show that the atoms in the imidazolium ring have a higher value indicating there is π bonding which is consistent with the delocalisation in the ring. C1-C2, C2-N3 and C6-N4 bonds have much lower ellipticity values indicating there is no π bonding involved. The ellipticity for C1-C2 implies a small amount of conjugation. The high ellipticity values for the P-F bonds in the PF_6^- anion indicates that there is a possibility of some π bonding in the anion.

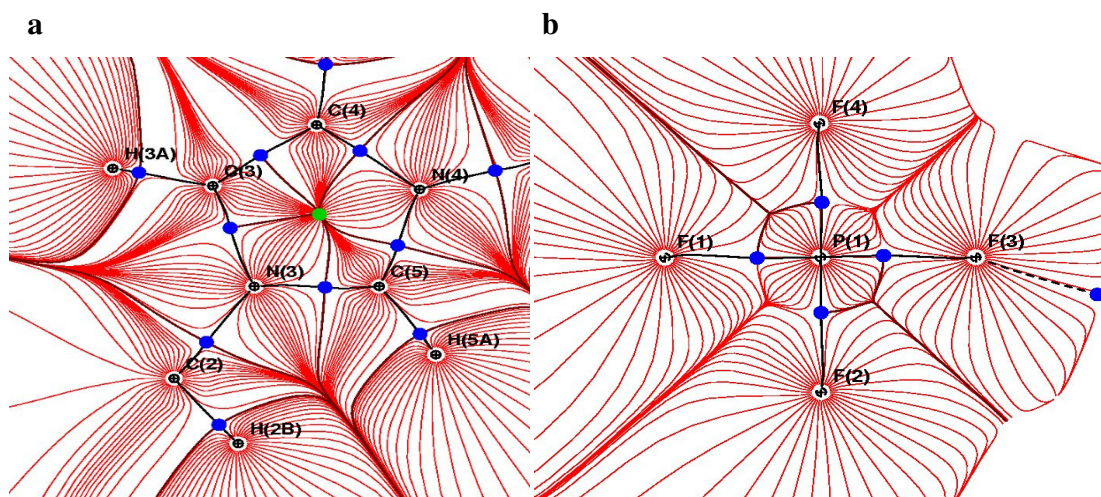


Figure 5.7: Experimental gradient lines obtained from the critical point search on the imidazolium ring (a), and the PF_6^- anion (b), the blue dots indicate the bonding critical point i.e. the point at which one atom starts and the other finishes, the green dot represent the ring critical point.

Table 5.3 shows the charges on the ionic liquid, the charge on a given atom is the difference between the monopole population for this atom observed from the charge density study and the number of valence electrons present classically in the atom. The sum of the charges confirms the PF₆⁻ anion is negatively charged with the imidazolium ring positively charged, which is consistent with that expected from the chemistry of ionic liquids.

Table 5.3: Charges for 1-Ethyl-3-methylimidazolium hexafluorophosphate

Atom	Charge	Atom	Charge
P(1)	0.213	C(3)	-0.523
F(1)	-0.113	C(1)	-0.861
F(3)	-0.144	H(1A)	0.236
F(4)	-0.135	H(6C)	0.343
F(6)	-0.116	H(1B)	0.332
F(2)	-0.07	H(2A)	0.337
F(5)	-0.064	H(6A)	0.277
N(3)	0.345	H(2B)	0.253
N(4)	0.359	H(1C)	0.303
C(5)	-0.44	H(5A)	0.234
C(2)	-0.509	H(6B)	0.304
C(4)	-0.336	H(3A)	0.335
C(6)	-0.856	H(4A)	0.296

5.3.8 Bonding nature

Table 5.4 gives the bond distances and angles of close bond contacts after the multipolar refinement has been applied. Figure 5.8 is a graphical representation of the close intermolecular contacts (red bonds). These bonds have been selected as they are shorter than the van der Waals radii (2.7 Å) used by Fuller *et al*²⁸ which were used to indicate a

hydrogen bond, however it has not been possible to deduce whether these bonds have hydrogen character and as such have been labelled as short bond contacts ($<2.5 \text{ \AA}$).

Table 5.4: Selected close contacts distances after refinement

Bond distances	\AA	Bond angles	(degrees)
F(1)-H(3A)	2.3522(5)	C3-F1...H3A	161
F(3)-H(6A)	2.4051(5)	C6-F3...H6A	150
F(3)-H(5A)	2.3952(5)	C5-F3...H5A	130
F(6)-H(4A)	2.3517(6)	C4-F6...H4A	159
F(3)-H(2A)	2.4765(6)	C2-F3...H2A	143
F(4)-H(6B)	2.4884(5)	C6-F4...H6B	110
F(2)-H(1B)	2.4662(6)	C1-F2...H1B	170

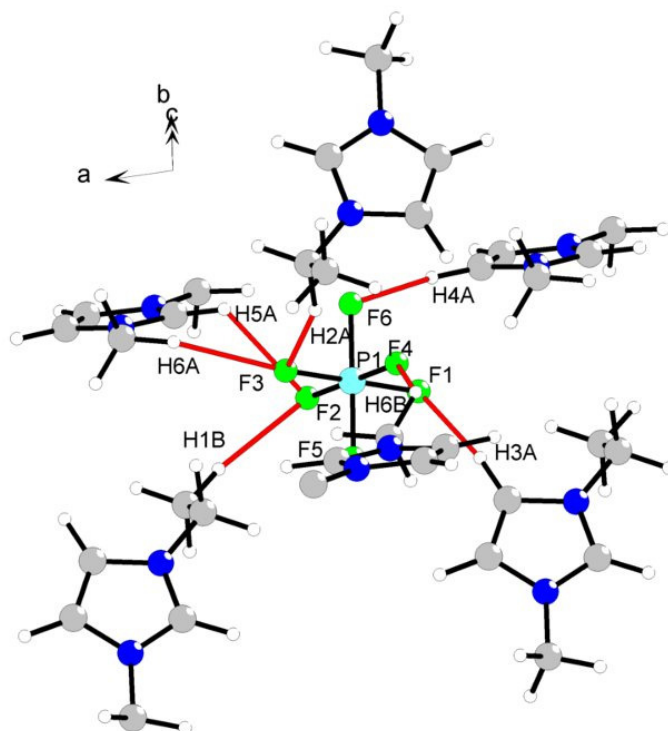


Figure 5.8: The shortest C-H...F bonds present in the structure with other imidazolium rings removed for clarity.

5.4.1 High resolution data of the Metal organic framework SIMOF-1

Ionic liquids have a great affect in metal organic synthesis in dictating the properties of the resulting framework. The aim of this section is to investigate the ionic liquid 1-butyl 3-methylimidazolium *in-situ* within the metal organic framework SIMOF-1 to try and get a greater understanding of the ILs influence in framework synthesis and compare it to the ionic liquid 1-ethyl-3-methylimidazolium hexafluorophosphate already collected in chapter 5.2.

5.4.2 Experimental

SIMOF-1 was provided by Lin *et al*¹⁵ and was synthesised as follows, an autoclave was charged with Ni(OAc)₂·4H₂O (380mg, 1.5mmol, Fisons), trimesic acid (210mg, 1mmol, Avocado) and ~1.5g 1-butyl-3-methyl-imidazolium L-aspartate (BMiM-L-asp) heated at 110°C for 3 weeks. The autoclave was then removed from the oven, cooled, filtered and dried.

5.4.3 Structure

The structure of SIMOF-1 consists of an octahedrally coordinated nickel atom which is coordinated by two water molecules and four trimesate which bind to the next nickel atom to form a three dimensional network. The ionic liquid is encapsulated within the pores of the framework. *Figure 5.10* shows the packed structure of the framework where the orientation of the ionic liquid can be seen clearly.

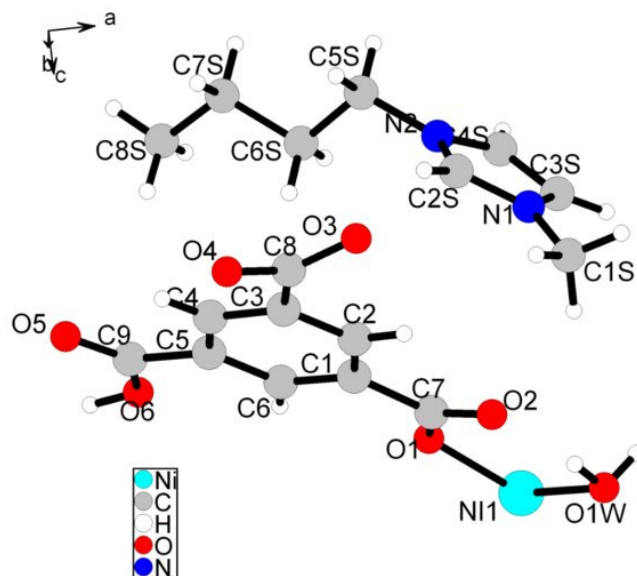


Figure 5.9: The asymmetric unit of SIMOF-1 which will be examined using the multipolar model.

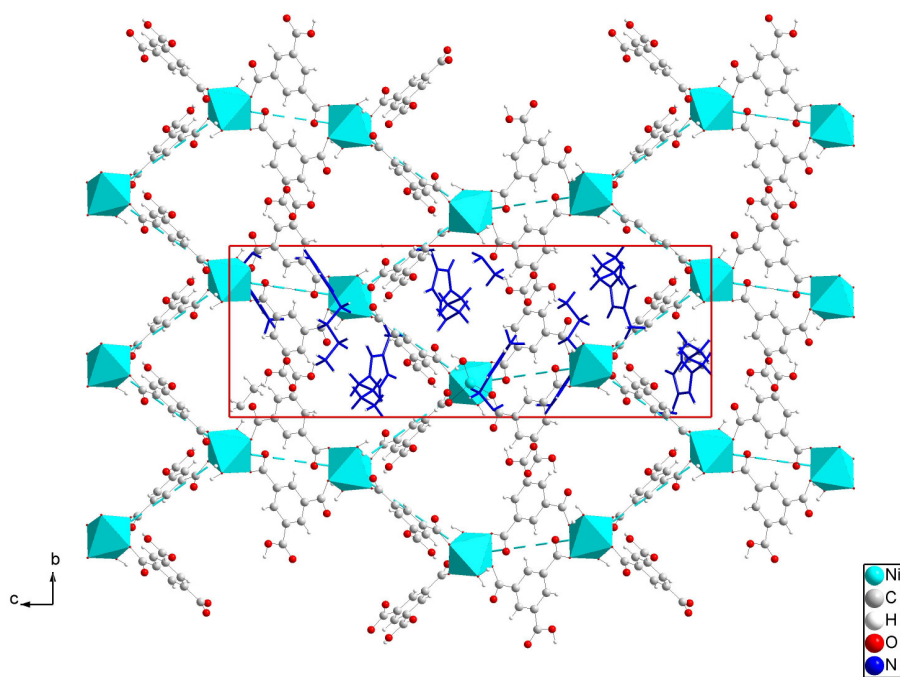


Figure 5.10: Crystal structure of SIMOF-1 from which it is possible to see 1-butyl 3-methylimidazolium from the ionic liquid which is encapsulated within the pore of the framework

5.4.4 Data collection

A high-resolution X-ray data set was collected in-house with Mo (0.73\AA) radiation on a Rigaku rotating anode. The data was cut at 0.46\AA and the Friedel pairs were merged using XPREP, the structure was solved and refined as described previously using SHELXS and SHELXL,³² non-hydrogen atoms were anisotropically refined and hydrogen atoms added geometrically. After a suitable R factor was achieved the instruction (.ins) and the reflection (hkl) files were renamed shelx.ins and shelx.hkl for the benefit of the XD2006 software.³³ The program XDINI was run on these two files to produce a series of files including an xd instruction file (xd.mas) where the multipole models and topological analysis could be applied. The hydrogen atoms were set to that of known neutron distances. The non-hydrogen atoms were then refined using the multipole least squares model gradually incrementing the multipole from monopole up to hexadecapole until no visible improvement is achieved.

5.4.5 Results

A residual map highlights the area of electron density which has not been accounted for *Figure 5.11* highlights the residual electron density from the ionic liquid ring whilst *Figure 5.12* highlights the electron density from the ring of the trimesate. On inspection it is clear that there is still some residual electron density however the maps appears to be quite featureless indicating that the model is almost complete, or that the data quality is not quite good enough to extract all the information required.

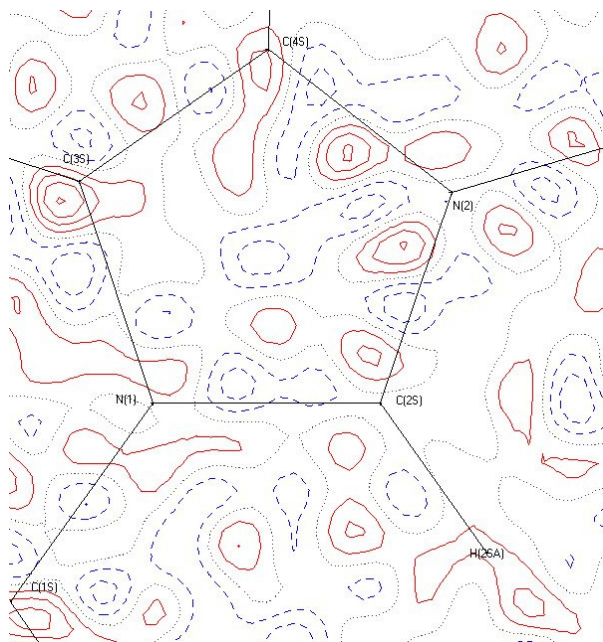


Figure 5.11: Residual map of the imizolium ring at $0.1e\text{\AA}^{-3}$, red lines indicate positive electron density, blue dashes indicate negative electron density.

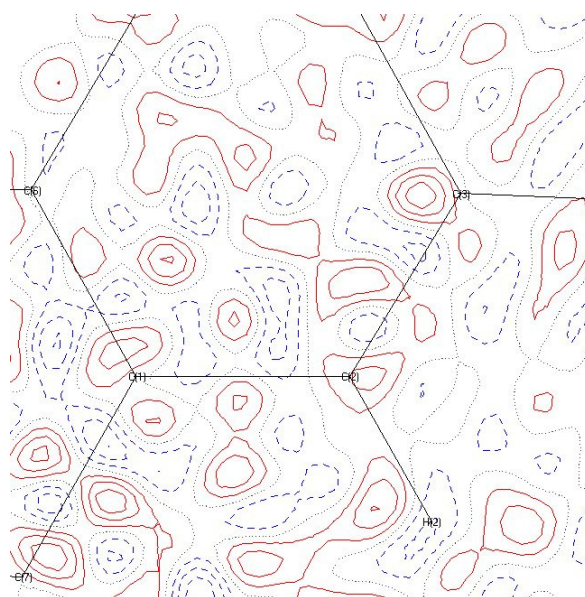


Figure 5.12: Residual map for the trimesate ring in the MOF at $0.1e\text{\AA}^{-3}$, red lines indicate positive electron density, blue dash indicates negative electron density.

Deformation density maps are another way of checking the quality of the data as they can be used to highlight any anomalies. In such a map the areas of high electron density at the atomic core are removed to locate the areas of interest from the valence electrons. These maps can be used to highlight lone pairs and the electron density present in the bonds. *Figure 5.13* is the deformation density map for the framework part of the metal organic framework, looking at the map it appears that the ring from the trimesate is well modelled. *Figure 5.14* shows the deformation density map for the ring of the 1-butyl 3-methylimidazolium and on inspection some of the electron density appears to be successfully modeled however between C4 and N2 the model does not seem very accurate and as such would indicate that the model requires further work.

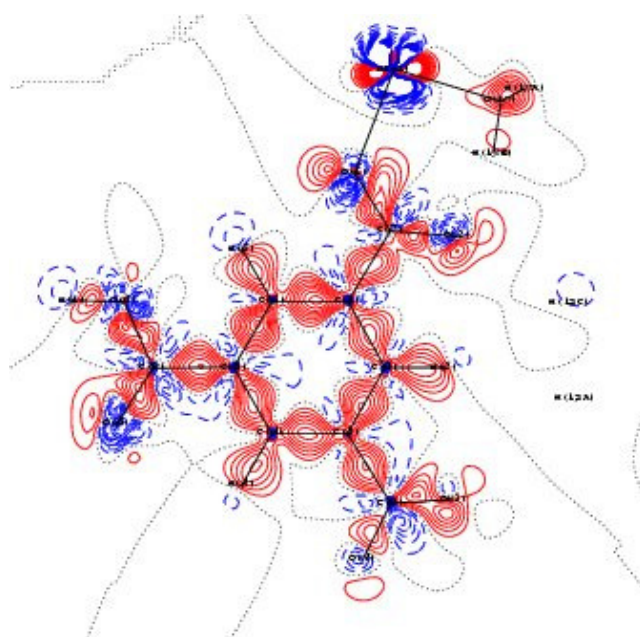


Figure 5.13: Deformation density map of the framework atoms, red lines indicate positive electron density, blue dash indicates negative electron density.

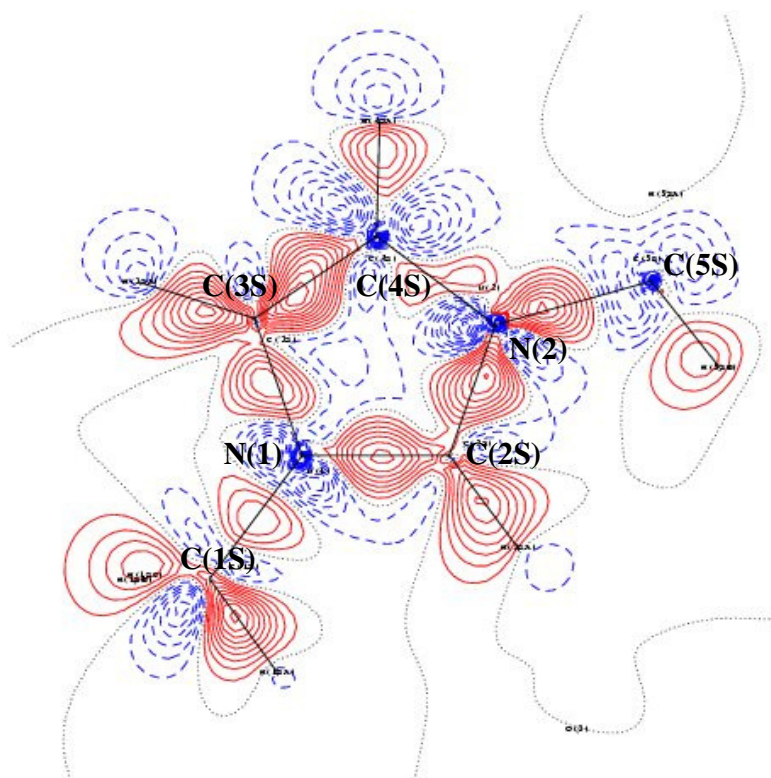


Figure 5.14: Deformation density map of 1-butyl 3-methylimidazolium. framework red lines indicate positive electron density, blue dash indicates negative electron density.

5.4.6 Topological features

Bader's theory of "atoms in molecules" (AIM)³⁶ provides a way to quantitatively examine the results from charge density experiments, by obtaining topological information about the system such as bond critical points. All the bond critical points (3,-1) and ellipticity values were located for the methylimidazolium and the trimesate rings and are reported in Table 5.1 and Table 5.2 respectively. The bond critical point is the point of minimum overlap between two atoms and ellipticity (ϵ) is a measure of the amount of π bonding present in the structure, with a large ϵ indicating a large amount of π bonding and a value of =0 indicating no π bonding.

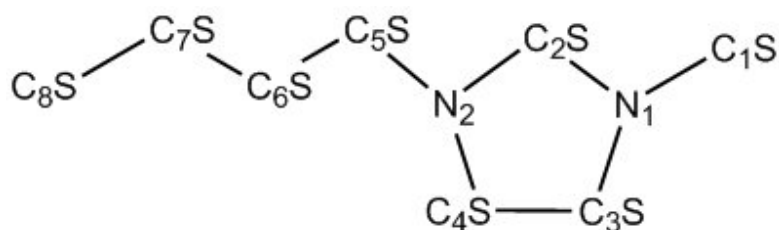


Figure 5.15: Schematic of the 1-butyl 3-methylimidazolium ring

Table 5.5: Information regarding all bond critical points (3,-1) for the ionic liquid 1-butyl 3-methylimidazolium contained within the pore of SIMOF-1. ϵ is the ellipticity and is defined by $\epsilon = (\lambda_1 - \lambda_2) / \lambda_3$, d_{1+2} is the length of the bond path between the atoms, d_1 and d_2 are distances along bond paths from the BCP to the first and atom respectively.

Bond	ρ	$\nabla^2 \rho$	d_{1+2}	d_1	d_2	λ_1	λ_2	λ_3	ϵ
C(1S)-N(1)	1.881	-26.459	1.4532	0.5985	0.8546	-17.27	-14.18	4.99	0.22
C(2S)-N(1)	2.528	-38.41	1.3424	0.533	0.8094	-24.56	-19.17	5.32	0.28
C(3S)-N(1)	2.251	-35.834	1.387	0.5709	0.8161	-21.86	-19.46	5.49	0.12
C(2S)-N(2)	2.362	-16.43	1.3176	0.415	0.9026	-27.13	-19.7	30.41	0.38
N(2)-C(2S)	2.362	-16.43	1.3176	0.9026	0.415	-27.13	-19.7	30.41	0.38
N(2)-C(4S)	1.999	-13.061	1.3913	0.7487	0.6427	-16.54	-11.6	15.07	0.43
N(2)-C(5S)	1.59	-14.397	1.5055	0.9829	0.5226	-12.48	-9.68	7.77	0.29
C(4S)-C(3S)	2.316	-35.696	1.368	0.5427	0.8253	-25.21	-12.92	2.44	0.95
C(5S)-C(6S)	1.837	-14.885	1.5143	0.6653	0.8491	-12.86	-11.88	9.85	0.08
C(6S)-C(7S)	1.654	-11.931	1.5512	0.6319	0.9193	-12.19	-8.31	8.58	0.47
C(7S)-C(8S)	1.493	-14.974	1.5671	0.5832	0.9839	-12.45	-11.15	8.63	0.12

The ellipticity results from the ionic liquid encapsulated within the MOF are not as clear cut as the ionic liquid by itself, the atoms in the ring agree with the existence of π bonding which can be attributed to delocalisation of the electrons however the ellipticity between C(4S) and C(3S) is rather large in comparison to the study from the previous section (5.2.7) whereby the same position resulted in an ellipticity of 0.34 (between C3-

C4). The ellipticity between C(6S) and C(7S) is an area for concern as this is rather large suggesting π bonding which is unlikely to be correct.

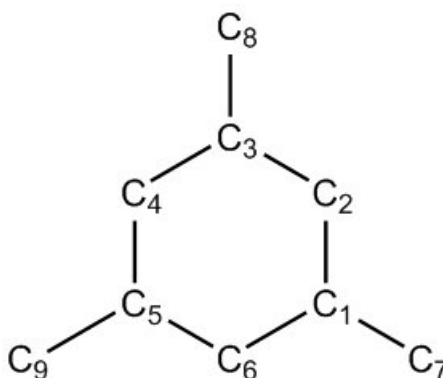


Figure 5.16: Schematic of the ring from the trimesate

Table 5.6: Information regarding all bond critical points (3,-1) for the trimesate ring. ε is the ellipticity and is defined by $\varepsilon = (\lambda_1 - \lambda_2) / \lambda_2$, d_{1+2} is the length of the bond path between the atoms, d_1 and d_2 are distances along bond paths from the BCP to the first and atom respectively.

Bond	ρ	$\nabla^2 \rho$	d_{1+2}	d_1	d_2	λ_1	λ_2	λ_3	ε
C(1)-C(2)	2.044	-18.221	1.3942	0.679	0.7152	-15.24	-11.59	8.61	0.31
C(2)-C(3)	2.119	-25.385	1.3961	0.5901	0.806	-16.24	-14.14	5	0.15
C(3)-C(4)	2.149	-22.575	1.4022	0.6863	0.716	-17.65	-13.3	8.38	0.33
C(4)-C(5)	2.152	-23.662	1.4003	0.7017	0.6985	-18.17	-13.97	8.47	0.3
C(5)-C(6)	1.977	-14.275	1.4018	0.4623	0.9395	-17.96	-5.05	8.73	2.56
C(6)-C(1)	2.258	-33.09	1.3978	0.5644	0.8335	-18.61	-17.18	2.71	0.08
C(3)-C(8)	1.844	-18.374	1.5051	0.7787	0.7264	-15.65	-11.23	8.5	0.39
C(5)-C(9)	1.923	-22.863	1.4916	0.819	0.6726	-17.47	-12.82	7.42	0.36
C(1)-C(7)	1.808	-18.846	1.5102	0.7468	0.7635	-15.44	-12.2	8.79	0.27

A critical point search was also performed on the ring from the trimesate to establish whether the overall model was correct, bonding critical points were located for all the

atoms in the ring, results of which are in *Table 5.2*. Looking at the table many of the ellipticity results are consistent with our understanding of the framework. However, the atoms bonded to C6 differ greatly especially between C(5)-C(6) ($\epsilon = 2.56$) which is nonsensical. This would therefore imply that although this is a good preliminary model further work is needed to ensure the results correspond to our knowledge of the systems.

5.5 Conclusion

High resolution X-ray diffraction is providing a way to examine materials in greater detail than previously possible aiding in the understanding and development of systems. This study has shown that it is possible to use high resolution X-ray diffraction to examine the ionic liquid 1-ethyl-3-methylimidazolium hexafluorophosphate using a multipolar model from which it was possible to model the electron density not usually modelled, *Figure 5.3* highlights how the bonding electron density can be successfully modelled using this multipole method. As this technique is still relatively in its infancy due to the difficulty in obtaining crystals of sufficient quality, it is important to ensure the model agrees with our understanding of the systems, from the multipole model it was possible to locate the charges on the respective cation and anion which agree with our knowledge of ionic liquids. The positive charge density seems to be on the nitrogen and hydrogen atoms, indicating that it is likely that their positions will dominate the interactions with frameworks. The deformation density maps also help to ensure our model has been assigned appropriately; *Figure 5.5* highlights the deformation map for the ionic liquid and highlights the bonding in the structure. The multipolar model has

been able to give an insight into the bonding nature of the imidazolium ring by confirming the delocalisation of the electrons in the imidazolium ring, and highlight the possible π bonding in the anion between the phosphorus and fluorine atoms.

Using the high angle datasets it is possible to get more information on the bonds and also a higher resolution for bond distances from which it has been possible to find close contact distances between the imidazolium ring and the anion. It has been postulated by Fuller *et al*²⁸ that these could be possible hydrogen bonds however more work is needed to be able to class these as hydrogen bonds. The information obtained from this study helps in our understanding of these systems which can then be used to develop and improve the computer models used to examine these kinds of structures.

This chapter has also shown that it is possible to get a high resolution data set of an extremely complicated metal organic framework (SIMOF-1), although the data quality we have so far is not good enough to make definitive statements. Looking at the deformation density and residual maps it is reasonable to say that the structure has been modelled relatively accurately. However, there are some discrepancies in the deformation map of the ionic liquid, also some of the results obtained from the critical point searches do not seem as accurate as the modelled EMIm PF₆⁻ ionic liquid.

The aim of this section was not to demonstrate the great results which can be obtained from high resolution X-ray diffraction on metal organic frameworks, it was to show how

difficult it is to get reliable data from such complicated systems and to try and push the boundaries of what this technique can offer the materials chemist.

A lot of these errors can be attributed to the presence of heavy elements in the structure but especially due to the contribution of the nickel metal within the structure, as mentioned in chapter 5.1, much of the work performed using high resolution data sets concentrates on small organic systems and do not tend to have any metals associated with them. These kinds of experiments are relatively few and as such it is difficult to differentiate between poor data and poor modelling, work by Farrugia *et al*³⁷ demonstrated that coding errors in the software resulted in the unusual features highlighted in a paper by Smith *et al*³⁸ to be incorrect, such as the evidence for the existence of metal-oxygen π bonding, whilst the new updated software highlights a previously unrecognised intramolecular H...H interaction in the macrocyclic ligand.

This work has shown that it is possible to get a high resolution dataset of a metal organic framework and an excellent dataset of an ionic liquid. However, much more work is required, on the algorithms of the software to enable the examination of heavier elements but also in improving the quality of crystals being produced so more data sets can be collected to help improve models.

5.6 References

- ¹ E.R. Cooper, C.D. Andrews, P. S. Wheatly, P. B. Webb, P. Wormald and R. E. Morris, *Nature*, 2004, **430**, 1012
- ² B.L. Bhargava, S. Balasubramanian and M. L. Klein, *Chem. Commun.*, 2008, 3339-3351
- ³ K. Dong, S. Zhang, D. Wang and X. Yao, *J.Phys.Chem. A.*, 2006, **110**, 9775-9782
- ⁴ E. A. Turner, C. C. Pye, and R. D. Singer, *J. Phys. Chem. A.*, 2003, **107**, 2277-2288
- ⁵ P. Feng, X. Bu and G. D. Stucky, *Nature.*, 1997, **388**, 736
- ⁶ J. Li, L. Li, J. Liang, P. Chen, J. Yu, Y. Xu and R. Xu, *Crystal Growth and Design.*, 2008, **8**, 2318-2323
- ⁷ J. Li, J. Yu, and R. Xu, *Microporous and Mesoporous Materials*, 2007, **101**, 406-412
- ⁸ P. Feng, X. Bu, T. E. Gier and G. D. Stucky, *Microporous and Mesoporous Materials*, 1998, **23**, 221-229
- ⁹ P. Feng, X. Bu and G. D. Stucky, *Angew. Chem. Int. Ed. Engl.*, 1995, **34**, 1745
- ¹⁰ T. Steiner, *Angew. Chem. Int. Ed.*, 2000, **41**, 48-76
- ¹¹ Z. Lin, Y. Li, A. M. Z. Slawin and R. E. Morris, *Dalton Trans.*, 2008, 3989-3994
- ¹² K. M. Dieter, C. J. Dymek, N. E. Heimer, J. W. Rovang and J. S. Wilkes, *J. Am. Chem. Soc.*, 1988, **110**, 2722-2726
- ¹³ D.N. Dybtsev, H. Chun and K. Kim, *Chem. Commun.*, 2004, 1594-1595
- ¹⁴ K. Jin, X. Huang, L. Pang, J. Li A. Appel and S. Wherland, *Chem. Commun.*, 2002, 2872-2873
- ¹⁵ Z. Lin, A.M.Z. Slawin and R.E. Morris, *J.Am.Chem.Soc.*, 2007, **129**, 4880-4881

- ¹⁶ S. Chen, J. Zhang and X. Bu, *Inorg. Chem.*, 2008, **47**, 5567-5569
- ¹⁷ B. Xiao, P. S. Wheatley, X. Zhao, A. J. Fleycher, S. Fox, A. G. Rossi, I.L. Megason, S. Bordiga, L. Regli, K. M. Thomas, and R.E. Morris, *J. Am. Chem. Soc.*, 2007, **129**, 1203-1209
- ¹⁸ D.J. Collins and H. Zhou, *J. Mater. Chem.*, 2007, **17**, 3154-3160
- ¹⁹ L. Alaerts, C.E. A. Kirschhock, M. Maes, M. A. van der Veen, V. Finsy, A. Delpa, J. A. Martens, G.V. Baron, P.A. Jacobs, J.F.M. Denayer and D.E. De Vos, *Angew. Chem. Int. Ed.*, 2007, **46**, 4293-4297
- ²⁰ M.R. Miller and I.L. Megson, *Br.J.Pharmacol.*, 2007, **31**, 624-631
- ²¹ L. Alaerts, C.E.A. Kirschhock, M. Maes, M. A. van der Veen, V. Finsy, A. Delpa, J.A. Martens, G.V. Baron, P.A. Jacobs, J.F.M. Denayer and D.E. De Vos, *Angew. Chem. Int. Ed.*, 2007, **46**, 4293-4297
- ²² R.D. Poulsen, A. Bentien, T. Graber, and B.B Iversen, *Acta Cryst A.*, 2004, **60**, 382-389
- ²³ R.D. Poulsen, A. Bentien, M. Chevalier and B.B Iversen, *J. Am. Chem. Soc.*, 2005, **127**, 9156-9166
- ²⁴ H.F. Clausen, J.Overgaard, Y.S. Chen and B.B. Iversen, *J. Am. Chem. Soc.*, 2008, **130**, 7988-7996
- ²⁵ P. Wasserscheid, and T. Welton, *Ionic Liquids in Synthesis Ch. 2.1.2*, 9–12 Wiley-VCH, Weinheim, Germany, 2003

- ²⁶ R.J. Cernik, W. Clegg, C.R.A Catlow, G. Bushnell-Wye, J.V. Flaherty, G.N. Greaves, I. Burrows, D.J. Taylor, S.J. Teat, M. Hamichi, *J. Synchrotron Radiat.*, 1997, **4**, 279.
- ²⁷ W. Clegg, M.R.J. Elsegood, S.J. Teat, C. Redshaw, and V.C. Gibson, *J. Chem. Soc., Dalton Trans.*, 1998 3037.
- ²⁸ J. Fuller, R. T. Carlin, H.C. De Long, and D. Haworth, *J. Chem. Soc., Chem. Commun.*, 1994, 299-300
- ²⁹ A. E. Bradley, C. Hardacre, J. D. Holbrey, S. Johnston, S. E. J. McMath, and M. Nieuwenhuyzen, *Chem. Mater.*, 2002, **14**, 629-635
- ³⁰ SAINT-Plus (version 7.24A). Bruker AXS Inc., Madison, Wisconsin, USA.
- ³¹ SADABS (version 2007/4), Bruker AXS Inc., Madison, Wisconsin, USA.
- ³² G.M. Sheldrick, *Acta Cryst A.*, 2008, **64**, 112-122
- ³³ XD2006 - a computer program for multipole refinement, topological analysis of charge densities and evaluation of intermolecular energies from experimental or theoretical structure factors. A. Volkov, P. Macchi, L.J. Farrugia, C. Gatti, P. Mallinson, T. Richter, T. Koritsanszky, 2006
- ³⁴ A. Ø. Madsen, *J. Appl. Cryst.*, 2006, **39**, 757-758
- ³⁵ N. K Hansen and P. Coppens, *Acta Cryst A.*, 1978 **34**, 909
- ³⁶ R. F. W. Bader, *Atoms in Molecules – a quantum theory*, 1990, Clarendon Press, Oxford
- ³⁷ L.J. Farrugia, C.S. Frampton, J.A.K. Howard, P.R. Mallinson, R.D. Peacock, G.T. Smith and B. Stewart, *Acta Cryst B.*, **62**, 236-244

³⁸ G.T. Smith, P.R. Mallinson, C.S. Frampton, L.J. Farrugia, R.D. Peacock and J.A.K. Howard, *J. Am. Chem. Soc.*, 1997, **119**, 5028

6 Structure and NMR assignment in AlPO₄-15: a combined study by diffraction, MAS NMR and first-principles calculations

6.1 Introduction

The applications of porous materials such as AlPOs are intimately connected with their structural architecture. Obtaining high quality structural data is, therefore, extremely important for determining how these materials function. As AlPOs are generally highly crystalline solids, X-ray diffraction is the main technique by which such information is obtained. Such structure determinations can be broadly split into two types; high resolution studies that focus on atomic position and charge density evaluation, and ‘normal’ resolution structures that are commonly utilised to obtain the atomic positions. Whilst it is expected that the high resolution structures will be the most accurate, these are rare for complex materials such as zeolites and other porous solids. However, recent work by Poulsen,^{1,2} and Claussen³ has shown that it is possible to obtain accurate charge density information for porous solids such as metal organic frameworks, which has some exciting implications given their important applications in gas storage and catalysis.^{11,12} One of the first, if not the only, aluminophosphate material for which a high resolution structure has been obtained is AlPO₄-15,⁴ an aluminophosphate material which contains only Al(VI) octahedral units along with PO₄ tetrahedra in the framework, with the NH₄⁺ SDA cation found in the relatively small pores.

Along with diffraction, solid-state nuclear magnetic resonance (NMR) spectroscopy is also an important tool for studying structure and ordering in zeotype frameworks. The

basic constituents of many frameworks are NMR-active nuclei (e.g., ^{29}Si , ^{27}Al , and ^{17}O for zeolites and ^{31}P , ^{27}Al , and ^{17}O for aluminophosphates). In addition, mineralisers, charge-balancing cations and many structure directing agents also contain NMR-active species. NMR has been used to both determine and confirm structure and space groups in frameworks, to study disorder, to identify through-bond connectivities, to detect Brønsted acid sites and to investigate exchange kinetics and dehydration.^{5,6,7,8,9,10} Furthermore, NMR is an excellent probe of dynamics in microporous frameworks, through either wideline experiments¹¹ or, more recently, through high-resolution MAS NMR¹². In addition to experimental approaches, there has been growing interest in the calculation of NMR parameters in the solid state owing, at least in part, to the recent introduction of first-principles approaches which exploit the inherent periodicity of many solids. In particular, the gauge including projector augmented wave (GIPAW)¹³ formalism, implemented within CASTEP,^{14,15} a planewave, pseudopotential code, has been shown to provide accurate shielding and quadrupolar tensors for a variety of nuclei in a range of materials, including porous frameworks,^{16,17} aiding spectral assignment and interpretation. This is of particular importance for quadrupolar ($I > 1/2$) nuclei, such as ^{27}Al ($I = 5/2$), where the second-order quadrupolar broadening observed under MAS hinders the extraction of information. Typically, more complex high-resolution experiments need to be performed (e.g., multiple-quantum (MQ) MAS¹⁸ or satellite-transition (ST) MAS)^{19,20} which, although an aid to resolution, do result in diminished sensitivity. Calculations also enable the relationship of NMR parameters to the local structural environment (e.g., their dependence on bond lengths or angles) to be investigated in an easy and flexible manner.

A crucial pre-requisite for first-principles calculations is an accurate initial crystal structure. The quality of structures obtained from diffraction vary depending upon the type of approach (e.g., X-ray or neutron) and the type of sample (e.g., powder or single crystal) utilized. In particular, the positions of lighter atoms, such as hydrogen, can be difficult to determine accurately using X-ray techniques but errors in these positions often have very large effects on calculated NMR parameters. Furthermore, the recent observation of microsecond timescale dynamics (associated with the template and water molecules in the pores of as-synthesized framework materials) using ^{27}Al STMAS NMR is a further complicating factor.¹² Indeed, recent work has demonstrated that there was very poor agreement between calculated and experimental ^{27}Al and ^{31}P NMR parameters in $\text{AlPO}_4\text{-14}$ (in both calcined and templated forms), unless some optimization of the X-ray derived atomic positions was performed prior to the NMR calculation.¹⁵ Although the modifications to the structure were reasonably small, and only minor differences observed between simulated diffraction patterns and those reported from experiment, the differences observed in the NMR parameters were considerable, demonstrating the sensitivity of NMR to small changes in the local environment.

6.2 Aim

In this work we utilise a multi-technique approach to study the microporous framework $\text{AlPO}_4\text{-15}$, synthesized using the NH_4^+ cation as a structure directing agent. Previous ^{27}Al MAS NMR spectra³¹ (78.2 MHz) appear confusing, containing a broad composite resonance around -10 ppm (a shift typical of six-coordinate Al), and no resolution of the two distinct Al (VI) species expected. An unexplained signal with an unusual shift (\sim

100 ppm) was also observed. The present work, therefore, has a number of aims; (i) to employ high-resolution ^{27}Al NMR experiments to attempt to resolve and identify the distinct Al species in $\text{AlPO}_4\text{-15}$, (ii) to unambiguously assign the resonances in both ^{27}Al and ^{31}P NMR spectra with the aid of first-principles calculations, (iii) to test the quality of different X-ray diffraction structures as starting points for first-principles calculations by comparing a model obtained using a high resolution charge density X-ray approach with synchrotron X-ray data obtained from a very small crystal.

6.3 Experimental

6.3.1 Synthesis

Aluminium sulfate hexadecahydrate (4 g, Aldrich) was dissolved in deionised water (50 ml) and ammonia (12.5 ml, Fisher). The solution was filtered and the resulting slurry dispersed in water (30 ml) and stirred. Once the solid had dissolved, ethanol (10 g BDH), phosphoric acid (1.4 g, 85% in H_2O , Aldrich) and tripropylamine (1.5 g, Aldrich) were added dropwise and mixed thoroughly. The solution was decanted to a Teflon lined autoclave and placed in a preheated oven for 4 days at 180 °C. After the crystallization period the autoclave was allowed to cool to room temperature overnight. The product was filtered, washed with water and dried. This material was used (as synthesized) for both synchrotron diffraction and solid-state NMR experiments.

6.3.2 Single Crystal X-ray Diffraction

The crystals prepared as described above were too small for data to be collected using an in-house X-ray source and so were studied using the high flux station 9.8^{21,22} at the Synchrotron Radiation Source (SRS), Daresbury, UK at low temperature (150 K) using an Oxford Cryosystems Cobra⁺. A Bruker-Nonius APEXII CCD area detector and D8 diffractometer using X-rays of wavelength 0.6709 Å. The structure was solved using direct methods (SHELXS-97)²³ and refined against F^2 using the least squares package (SHELXL-97).²³ The hydrogen atoms were added geometrically and refined as riding on the atom to which they were attached, and all the non hydrogen atoms were refined anisotropically.

6.3.3 NMR spectroscopy

Experiments were performed using either a Varian Infinity Plus 500 MHz or a Bruker Avance 400 spectrometer, equipped with widebore 11.7 and 9.4 T magnets, with Larmor frequencies of 130.3 and 104.3 MHz (²⁷Al), and 202.5 and 162.0 MHz (³¹P). Powdered samples were packed in conventional 4 mm or 2.5 mm ZrO₂ rotors and rotated at rates between 10 and 30 kHz. Typical recycle intervals were 500 ms (²⁷Al) and 60 s (³¹P). Chemical shifts are shown relative to 1 M Al(NO₃)₃ (aq) for ²⁷Al and 85 % H₃PO₄ for ³¹P. For ²⁷Al MAS spectra were recorded using a spin-echo pulse sequence selective for the central transition. Triple-quantum MAS experiments were performed using a split-t₁ shifted-echo pulse sequence,²⁴ with typical radiofrequency field strengths of 130 kHz for multiple-quantum excitation and conversion and 10 kHz for the central-transition

selective inversion pulse. The scale of the isotropic δ_1 axis is plotted according to the conventions described in Ref.25.

6.3.4 Calculations

Calculations were carried out using the CASTEP^{26,27} density functional theory (DFT) code, which employs the gauge including projector augmented wave (GIPAW)¹³ algorithm, to reconstruct the all-electron wave function in a magnetic field. The generalized gradient approximation (GGA) PBE²⁸ functional was used and the core-valence interactions were described by ultrasoft pseudopotentials.¹⁴ Valence orbitals were 3s, 3p (²⁷Al), 2s, 2p (¹⁷O), 3s, 3p (³¹P), with core radii of 2.0 Å, 1.3 Å and 1.81 Å, respectively. Integrals over the Brillouin zone were performed using a Monkhorst-Pack grid with a k-point spacing of 0.05 Å⁻¹. Wavefunctions were expanded in planewaves with a kinetic energy smaller than the cut-off energy, typically ~600-700 eV. Calculations were performed using the EaStCHEM Research Computing Facility, which consists of 136 AMD Opteron processing cores partly connected by Infinipath high speed interconnects. Typical NMR calculation times were 24 hours using 3 cores.

The absolute shielding tensor, σ , and electric field gradient (EFG) tensor, \mathbf{V} , in the crystal frame are generated by the program. From these, the isotropic chemical shift, δ_{iso} , is given by $-(\sigma_{\text{iso}} - \sigma_{\text{ref}})$, where σ_{iso} , the isotropic shielding, is $(1/3) \text{Tr}\{\sigma\}$. Reference shieldings, σ_{ref} , of 549.7 ppm and 278.3 ppm were used for ²⁷Al and ³¹P, respectively. These were obtained from previous work¹⁵. The magnitude, Δ_{CS} , and asymmetry, η_{CS} , of

the chemical shift anisotropy (CSA) are given by $\Delta_{\text{CS}} = \sigma_{\text{ZZ}} - \sigma_{\text{iso}}$ and $\eta_{\text{CS}} = (\sigma_{\text{YY}} - \sigma_{\text{XX}})/(\sigma_{\text{ZZ}} - \sigma_{\text{iso}})$. The magnitude (C_{Q}) and asymmetry (η_{Q}) of the quadrupolar interaction are given by $C_{\text{Q}} = eQV_{\text{ZZ}}/h$ and $\eta_{\text{Q}} = (V_{\text{XX}} - V_{\text{YY}})/V_{\text{ZZ}}$. A quadrupole moment, eQ , of 140.3 mB was used for ^{27}Al .

Structural parameters (the unit cell and all 100 atomic positions) were obtained either from experimental diffraction studies in the literature,²⁹ or from a good standard data set obtained from station 9.8 at the SRS, with corresponding references given where appropriate in the text. The crystal structure was reproduced from these parameters using periodic boundary conditions. Where used, geometry optimization was also performed within the CASTEP program, with either just the atomic coordinates or both the lattice parameters and atomic coordinates allowed to vary. An initial geometry optimization of only the ^1H positions was also performed.

6.4 Results and Discussion

The structure of $\text{AlPO}_4\text{-15}$ is shown in *Figure 6.1a*, where PO_4 tetrahedra and AlO_6 octahedra link to form channels parallel to the b axis, of approximately 6.4 Å in diameter^{29,30}. The asymmetric unit consists of two Al, two P, nine H, a single N and eleven O atoms. The channels are filled with ammonium cations and water molecules, both of which exhibit hydrogen bonds to the framework. There are two distinct P species, each coordinated by four O with P-O bond distances between 1.507(1) and 1.5546(1) Å (synchrotron structure). The two distinct Al species are coordinated by six

O, four of which are bonded to P. For Al(1), the coordination sphere is completed by two hydroxyl species, whilst for Al(2) a single hydroxyl (which bridges between Al(1) and Al(2)) and a water molecule are bonded, as shown in *Figure 6.1b*.

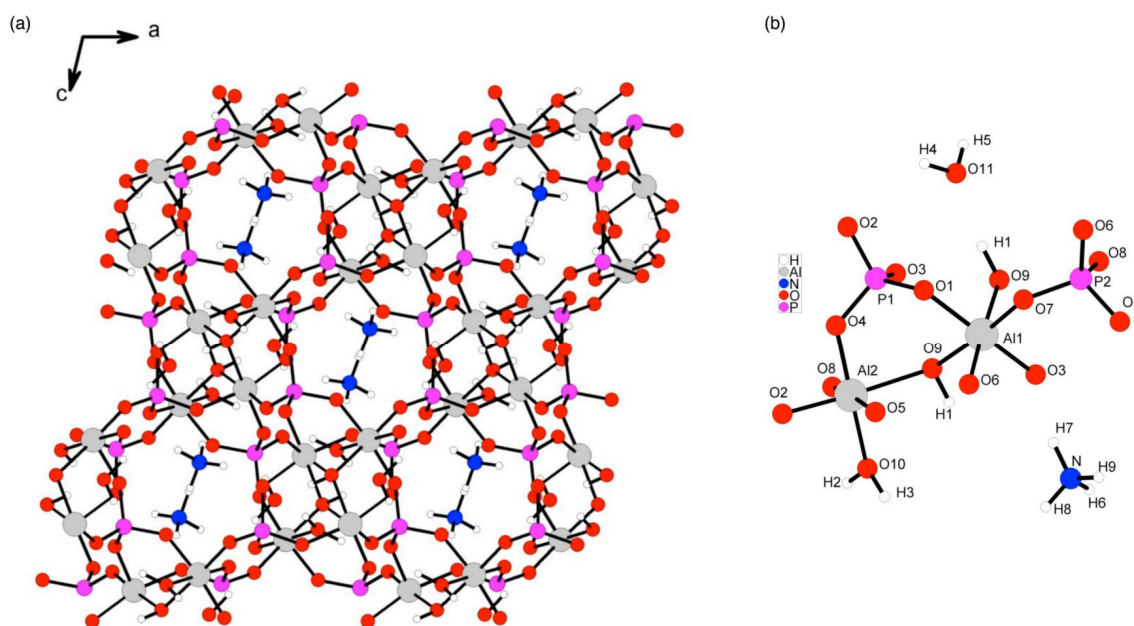


Figure 6.1:(a) Structure of as-synthesized AlPO₄-15 with ammonium template, showing the 6.4 Å channels parallel to the b axis. (b) Expansion showing the local coordination environments of the Al and P species. P atoms are denoted by pink spheres, Al by grey spheres, O by red spheres, N by blue spheres and H atoms by white spheres.

Figure 6.2 shows ²⁷Al and ³¹P MAS NMR spectra of AlPO₄-15. The ³¹P spectrum in Figure 6.2(a), contains two resonances separated by ~6 ppm, corresponding to the two distinct species expected. The ²⁷Al MAS spectrum (9.4 T) reveals a sharper component at ~0 ppm (a shift typical of six-coordinate Al), with a shape characteristic of quadrupolar broadening. In addition, a second component is observed, centred at -40

ppm. In contrast to previous work,³¹ this spectrum was recorded using a spin-echo pulse sequence, in order to reduce the distortions which can arise when broad lineshapes are present. It can be seen that the second lineshape is considerably broader than the first, reflecting a much larger quadrupolar interaction. This interaction will also shift the resonance (to lower ppm) from the true isotropic chemical shift. At 11.7 T, this second component is narrower (as the second-order quadrupolar interaction is proportional to $1/\omega_0$), and is centred closer to the first. This suggests that the signal observed at ~100 ppm in the early NMR work³¹ (acquired at lower field and without the aid of an echo) results from a second Al species with a much broader lineshape, severely distorted and shifted to significantly lower frequencies than expected for six-coordinated Al by a large second-order quadrupolar shift. This would indicate that the two distinct Al species are resolved in the MAS spectrum directly (and are not superimposed as suggested previously). This is supported by the ²⁷Al triple-quantum MAS (9.4 T) spectrum of AlPO₄-15, recorded with a split-t₁ shifted-echo sequence,²⁴ shown in *Figure 6.3*. The removal of the quadrupolar broadening reveals two distinct Al species (at δ_1 of 4 and 12.5 ppm) in the high-resolution spectrum. The difference in relative intensities (expected to be 1:1 from the crystal structure) is a consequence of the non-quantitative nature of MQMAS, with the triple-quantum filtration decreasing in efficiency as the quadrupolar interaction decreases. Cross-sections taken parallel to δ_2 along the ridges contain one sharp and one much broader lineshape. The NMR parameters, obtained from a combination of fitting the MAS lineshapes, fitting the MQMAS cross-sections and from the position of the centre-of-gravity (δ_1 , δ_2) of the resonances in the MQMAS

spectrum, are given in *Table 6.1*. A spectrum simulated using these parameters is also shown (in red) on *Figure 6.2b*.

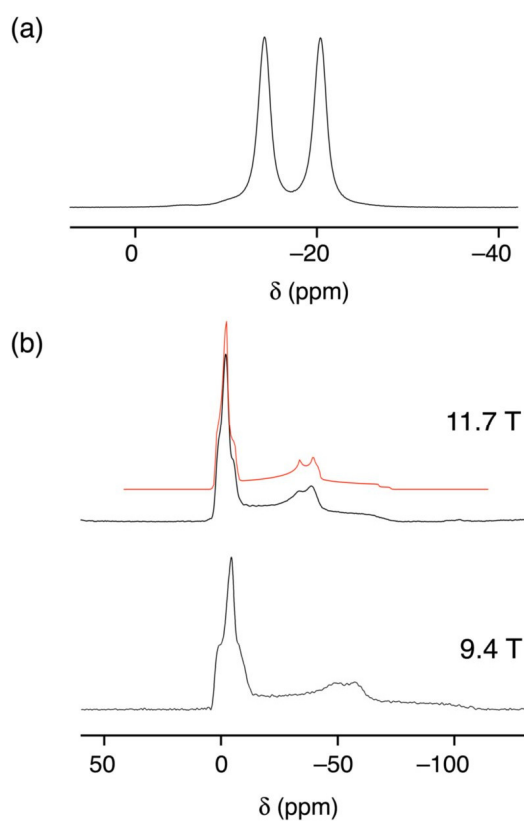


Figure 6.2: (a) ^{31}P (11.7 T) and (b) ^{27}Al (9.4 and 11.7 T) MAS NMR spectra of as-synthesized $\text{AlPO}_4\text{-15}$, along with a spectrum simulated using the values shown in *Table 6.1* (shown in red). In (b), spectra were recorded using a central-transition selective spin-echo pulse sequence ($\tau = 4$ ms) with a radiofrequency field strength, $\omega_1/2\pi$, of 10–20 kHz. Spectra are the result of averaging (a) 64 and (b) 2400 transients, with recycle intervals of (a) 60 s and (b) 500 ms. The MAS rates were (a) 10 and (b) 13 (11.7 T) and 30 (9.4 T) kHz.

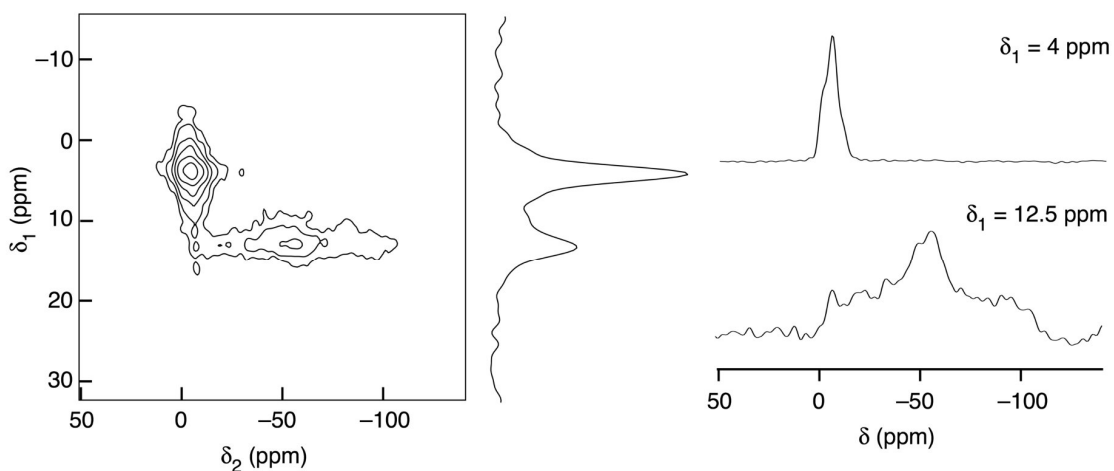


Figure 6.3: ^{27}Al (9.4 T) two-dimensional triple-quantum MAS spectrum, isotropic projection and cross-sections extracted parallel to δ_2 (with δ_1 of 4 and 12.5 ppm) of as-synthesized $\text{AlPO}_4\text{-15}$, recorded using a split- t_1 shifted-echo pulse sequence²⁴. The spectrum is the result of averaging 1440 transients, with a recycle interval of 500 ms for each of 64 t_1 increments of 66.6 μs . The MAS rate was 30 kHz.

Table 6.1: Experimental ^{31}P and ^{27}Al NMR parameters (quadrupolar coupling constant (C_Q), asymmetry (η_Q), quadrupolar product (P_Q), isotropic chemical shift (δ_{iso})) for as-synthesized $\text{AlPO}_4\text{-15}$.

	C_Q/MHz	η_Q	P_Q/MHz	$\delta_{\text{iso}}(\text{ppm})$
Al(1)	3.1(1)	0.80(5)	3.5(1)	2.5(10)
Al(2)	8.3(1)	0.80(5)	9.2(1)	-5.0(10)
P(1)				-14.3(5)
P(2)				-20.5(5)

Despite the acquisition of both high-resolution ^{27}Al and ^{31}P spectra for $\text{AlPO}_4\text{-15}$, spectral assignment remains a problem in both cases. For other similar materials, two-dimensional heteronuclear correlation experiments (where Al/P through-bond or through-space proximity is probed) can be utilised to aid with assignment.³¹ However, in $\text{AlPO}_4\text{-15}$, both Al species are connected to two P(1) and two P(2). In addition, the

similarity of the species make distinguishing either the two P or the two Al difficult. For P, the two species have very similar average P-O bond lengths (1.533 and 1.530 Å for P(1) and P(2), respectively). However, the average P-O-Al angle is larger for P(2) (138.9° and 133.8°), which has been shown empirically in the literature to result in a decreased chemical shift³². This would suggest an assignment of P(1) and P(2) for peaks at δ of -14.3 and 20.5 ppm, respectively. The two Al species also have very similar local geometries, despite very different C_Q values. Although the average Al-O bond lengths are similar, there is perhaps a greater variation/range in bond length for Al(2). However, if O-Al-O angles are considered, Al(1) appears to have a more distorted geometry.

One approach to help assignment and interpretation of NMR spectra is the use of first-principles calculations, with much recent interest in codes which achieve this for periodic systems. It has recently been demonstrated that such an approach can be successfully implemented to calculate ^{27}Al and ^{31}P NMR parameters in aluminophosphate framework solids,¹⁵ despite the problems which may be posed by the framework flexibility, the presence of templates and water within the pores and the possibility for dynamics. However, it was shown that in this case geometry optimization of both the atomic coordinates and the unit cell was required for best agreement with the experiment. *Table 6.2* shows ^{27}Al and ^{31}P NMR parameters calculated using CASTEP^{13,26} for $\text{AlPO}_4\text{-15}$, from crystal structures obtained using initial structures obtained using both charge density⁴ and synchrotron single-crystal diffraction approaches. In addition to results using the original structures (denoted column A in

Table 6.2), calculations were also performed after optimization of the ^1H positions (denoted B in *Table 6.2*), with subsequent optimization of all atomic positions (C), and finally, with additional optimization of the unit cell parameters (D). Unlike previous work on $\text{AlPO}_4\text{-14}$,²⁹ the agreement obtained between calculated and experimental values is good, even without any optimization. Interestingly, very similar results are obtained when using both the structure from charge density experiments and that from synchrotron single-crystal diffraction. This probably reflects the increased accuracy of both approaches in comparison to the structures obtained from powder X-ray diffraction for the various forms of $\text{AlPO}_4\text{-14}$. The calculations do provide insight into the assignment of both the ^{27}Al and ^{31}P spectra. In the latter case, the chemical shift of P(1) is 6 ppm higher (-12.0) than that of P(2), in agreement with the empirical predictions described earlier. For ^{27}Al , the large difference in quadrupolar coupling between the two species is well reproduced, with C_Q values of ~ -3.4 and 8.2 MHz for Al(1) and Al(2), respectively. (Note that the sign of C_Q , while reported here for calculated values, is not possible to determine simply by experiment). There is also good agreement in the values of η_Q and δ_{iso} for both approaches. There is little change in the calculated values upon optimization of the ^1H positions, although the forces upon the atoms have been reduced from 1.4 to 0.17 eV/Å. This step is common practice when calculating NMR parameters by DFT as ^1H positions are typically poorly described, particularly by X-ray diffraction.

Table 6.2: Calculated ^{31}P and ^{27}Al NMR parameters (quadrupolar coupling constant (C_Q), asymmetry (η_Q), isotropic chemical shift (δ_{iso})) for as-synthesized $\text{AlPO}_4\text{-15}$. Values are given for the calculations using the original diffraction structure (A), a structure with optimization of the 1H positions (B), a structure with optimization of all atomic positions (C) and a structure where in addition the unit cell size was also allowed to vary (D).

	A			B			C			D		
	C_Q / MHz	η_Q	δ_{iso} (ppm)									
Charge density structure												
Al(1)	-3.26	0.70	3.4	-3.20	0.73	3.5	-3.61	0.78	3.3	2.84	0.42	1.4
Al(2)	8.21	0.93	-4.4	8.33	0.87	-4.2	7.96	0.99	-4.3	8.43	0.85	-4.9
P(1)			-12.0			-12.6			-12.0			-10.9
P(2)			-18.5			-19.0			-17.9			-17.9
Single crystal diffraction structure												
Al(1)	-3.50	0.68	2.8	-2.90	0.83	3.3	-2.85	0.90	3.2	2.88	0.47	1.5
Al(2)	8.25	0.94	-4.6	8.47	0.82	-4.2	-7.70	0.97	-4.3	8.29	0.86	-4.9
P(1)			-12.4			-13.4			-12.1			-10.8
P(2)			-19.1			-19.5			-17.9			-17.8

As discussed above, the large difference in the values of the two ^{27}Al C_Q values is perhaps surprising, given the similarity in their local environments; both species are octahedrally coordinated with similar average bond lengths and average O-Al-O angles. Empirical correlations exist in the literature relating the ^{27}Al C_Q to the longitudinal and shear strain parameter (measures of the distortion from ideality of bond distances and bond angles, respectively). Previous work has shown that for tetrahedral Al species a linear dependence of C_Q with shear strain was observed, the correlation with longitudinal strain was poor. In contrast, for octahedral Al species, a much better correlation was found with the longitudinal strain.³³ This is supported by this work, where the largest C_Q is found for Al(2) which displays the greater variation of bond lengths, not Al(1) where the variation of bond angles is largest. It would be difficult

however, to predict this result on the basis of the structure alone, without the support of the calculations.

As shown in *Table 6.2*, only small differences in the NMR parameters are observed when all atomic positions (C) and additionally the unit cell (D) are allowed to vary. As the changes are not considerable it could be argued that all cases agree well with experiment (given the expected uncertainty on the experimental values), though the agreement in case C appears least good. As described previously, this probably reflects the increased accuracy of both initial structures. All calculations support the spectral assignment. The changes observed (from A to B, C and D) are similar no matter which structure is used initially. In particular, the decrease in η_Q in case D is present in both cases. The only significant difference between the two is in the sign of C_Q for Al(2) in case C. However, this apparently large change can be easily understood as the value of η_Q is close to 1, requiring only a very small change in the principal components of the quadrupole tensor to bring about the sign change. Although the geometry optimizations further reduce the forces on the atoms, this results in only very small changes in most atomic positions. *Figure 6.4* shows the changes in the Al-O and P-O bond distances for three structures (A, C and D) for both charge density (filled circles) and single-crystal diffraction (open circles) data. The changes are very small (typically less than 1%) with the exception of the Al(2)-OH bond distance which appears to vary by 3%. Given the known tendency of DFT (and GGA) to overestimate interatomic distances, these changes can be considered almost negligible. Again, this can be contrasted to the

behaviour observed for $\text{AlPO}_4\text{-14}^{15}$ where more significant changes in structure were observed upon optimization.

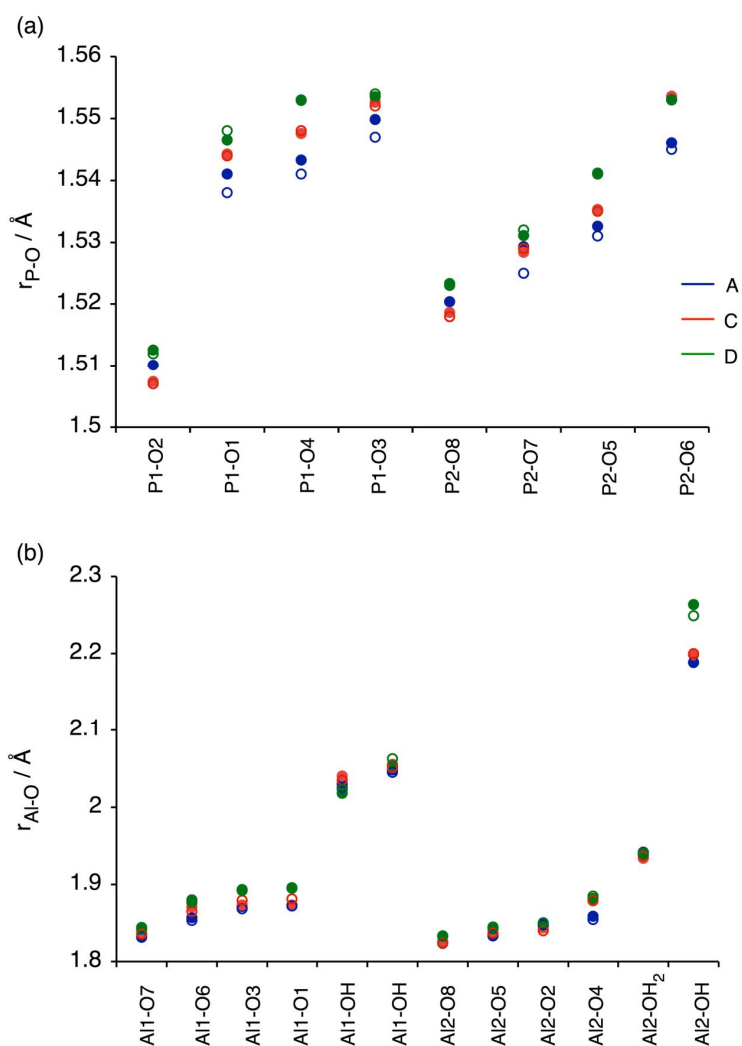


Figure 6.4: Plots of (a) P–O and (b) Al–O bond distances in $\text{AlPO}_4\text{-15}$ from DFT calculations for structures derived from charge density (filled circles) and single-crystal diffraction (open circles) measurements with no optimization (blue; structure A), optimization of all atomic coordinates (red; structure C), and additional optimization of unit cell parameters (green; structure D).

6.5 Conclusions

A combination of diffraction, high-resolution solid-state NMR and first-principles calculations have been employed to investigate the local structure in the aluminophosphate framework AlPO₄-15. In contrast to previous NMR work the two distinct Al species were resolved and identified using both MAS and high-resolution multiple-quantum (MQ) MAS experiments. One of the species (determined to be Al2) has a much larger quadrupolar interaction than perhaps expected and so appears significantly shifted to low frequency in the MAS spectrum. First-principles calculations were utilized to assign both the ²⁷Al resonances, and the two resonances in the ³¹P MAS spectrum. Good agreement with experiment was obtained, despite the potential problems associated with the possible flexibility of the framework itself, the presence of a template and water molecules within the pores and channels and the possibility of dynamics. Unlike previous work on AlPO₄-14, the calculations were in very good agreement with experiment when initial structures generated by diffraction experiments were used, and relatively little change was observed upon geometry optimization. Furthermore, calculations using a structure obtained using charge-density measurements and a structure from more conventional single-crystal diffraction produced very similar results. These results indicate that conventional single crystal X-ray diffraction experiments, even when performed on very small crystals at synchrotron sources, are of suitable accuracy to use as starting models for first-principles NMR calculations, which in turn are extremely useful in understanding experimental solid-state NMR data, leading to an improved understanding of the local structure in these materials.

6.6 References

- ¹ R.D. Poulsen, A. Bentien, T. Graber, and B.B Iversen, *Acta Cryst A.*, 2004, **60**, 382-389
- ² R.D. Poulsen, A. Bentien, M. Chevalier and B.B Iversen, *J. Am. Chem. Soc.*, 2005, **127**, 9156-9166
- ³ H.F. Clausen, J.Overgaard, Y.S. Chen and B.B. Iversen, *J.Am.Chem.Soc.*, 2008, **130**, 7988-7996
- ⁴ E. Aubert, F. Porcher, M. Souchassou , and C. Lecomte. *Acta Cryst B.*, 2003, **59**, 687-700
- ⁵ J. Klinowski, *Prog. Nucl. Magn. Reson. Spectrosc.*, 1984, **16**, 237.
- ⁶ D.H. Brouwer, R.J. Darton, R.E. Morris and M.H. Levitt, *J. Am. Chem. Soc.*, 2005, **127**, 10365.
- ⁷ C.A. Fyfe, H.M.Z. Altenschildesche, K.C. Wong–Moon, H. Grondey and J. M. Chezeau, *Solid State Nucl. Magn. Reson.*, 1997, **9**, 97.
- ⁸ J. W. Wiench and M. Pruski, *Solid State Nucl. Magn. Reson.*, 2004, **26**,51.
- ⁹ L.M. Peng, Y. Lui, N.J. Kim, J. E. Readman and C.P. Grey, *Nature Materials*, 2005, **4**, 216.
- ¹⁰ J.F. Stebbins, P.D. Zhao, S.K. Lee and X. Cheng, *Am. Mineral.*, 1999, **84**, 1680.
- ¹¹ J. Gonzalez, R.N. Devi, P.A. Wright, D.P. Tunstall and P.A. Cox, *J. Phys. Chem. B.*, 2005, **109**, 21700.
- ¹² S. Antonijevic, S.E. Ashbrook, S. Biedasek, R.I. Walton, S. Wimperis and H. Yang, *J. Am. Chem. Soc.*, 2006, **128**, 8054.

- ¹³ C. J. Pickard, F. Mauri, *Phys. Rev. B*, 2001,**63**, 245101
- ¹⁴ J. R. Yates, C. J. Pickard and F. Mauri, *Phys. Rev. B*, 2007, **76**, 024401.
- ¹⁵ S. E. Ashbrook, M. Cutajar, C.J. Pickard, R.I. Walton and S. Wimperis, *Phys. Chem. Chem. Phys.*, 2008, **10**, 5754
- ¹⁶ S.E. Ashbrook, A.J. Berry, D.J. Frost, A. Gregorovic, C.J. Pickard, J.E. Readman and S. Wimperis, *J. Am. Chem. Soc.*, 2007, **129**, 13213.
- ¹⁷ T. Charpentier, S. Ispas, M. Profeta, F. Mauri and C.J. Pickard, *J. Phys. Chem. B*, 2004, **108**, 4147.
- ¹⁸ L. Frydman and J.S. Harwood, *J. Am. Chem. Soc.*, 1995,**117**, 5367.
- ¹⁹ Z. Gan, *J. Am. Chem. Soc.*, 2000, **122**, 3242.
- ²⁰ S.E. Ashbrook and S. Wimperis, *Prog. Nucl. Magn. Reson. Spectrosc.*, 2004, **45**, 53.
- ²¹ W. Clegg, M.R.J. Elsegood, S.J. Teat, C. Redshaw and V.C. Gibson, *J. Chem. Soc. Dalton Trans.*, 1998, 3037.
- ²² R.J. Cernik, W. Clegg, C.R.A. Catlow, G. Bushnell-Wye, J.V. Flaherty, G.N. Greaves, I. Burrows, D.J. Taylor, S.J. Teat and M. Hamichi, *J. Synchrotron Radiat.*, 1997, **4**, 279.
- ²³ G. M. Sheldrick, *Acta. Cryst. A*, 2008, **64**,112.
- ²⁴ S. P. Brown and S. Wimperis, *J. Magn. Reson.*, 1997, **124**, 279.
- ²⁵ K.J. Pike, R.P. Malde, S.E. Ashbrook, J.McManus and S. Wimperis, *Solid State Nucl. Magn. Reson.* 2000, **16**, 203.
- ²⁶ M.D. Segall, P.J.D. Lindan, M. J. Probert, C.J. Pickard, P.J. Hasnip, S.J. Clark, and M.C. Payne, *J. Phys. Cond. Matt.*, 2002, **14**, 2717.
- ²⁷ J. R. Yates, C. J. Pickard and F. Mauri, *Phys. Rev. B*, 2007, **76**, 024401.

- ²⁸ J. P. Perdew, K. Burke and M. Ernzerhof, *Phys. Rev. Lett.*, 1996, **77**, 3865.
- ²⁹ E. Aubert, F. Porcher, M. Souchassou, C. Lecomte, *Acta. Cryst. B*, 2003, **59**, 687.
- ³⁰ J.J. Pluth, J.V. Smith, J.M. Bennett and J.P. Cohen, *Acta. Crystallog. C*, 1984, 2008.
- ³¹ N. Bilba, A. Azzouz, N. Naumn and D. Nibou, *Zeolites and Related Micro. Mater.*, 1994, **84**, 605.
- ³² D. Müller, E. Jahn, G. Ladwig and U. Haubenreisser, *Chem. Phys. Lett.*, 1984, **109**, 332.
- ³³ S. Ghose and T. Tsang , *Am. Mineral.*, 1973, **58**, 748.

7 Gas Storage in Porous Materials

7.1 Introduction

Gas storage is a hot topic at the moment with applications for environmental issues, medical devices and in energy storage. Gases can be stored in a tank however this means the tank is usually at a high pressure to ensure enough gas can be stored.

A solution to this problem is to physisorb or chemisorb the gas in a solid medium with a large surface area enabling more gas to be contained within a given volume than a conventional pressurised container, reducing the pressure needed to contain the gas in an attempt to mitigate the dangers of handling and transport.

Another requirement for gas storage is being able to control the rate at which the gas is released. Can small amounts of gas be administered as and when required? A material is only a good storage medium if it can store and release the desirable amount under the condition it is to be used. Raising the temperature, exposure to UV light or just by releasing the pressure are all different ways a gas can be released from the material.

There are many examples of gas storage in materials such as activated carbon^{1,2} and metal oxides.^{3,4} However, the most publicised are that of zeolites and metal organic frameworks, which have already been discussed earlier in this thesis. The main advantages these types of materials have over others is their large surface areas, with zeolites achieving several hundred m^2g^{-1} and some MOFs exceeding $5000\text{m}^2\text{g}^{-1}$.^{5,6} The metal sites in both zeolites and MOFs also provide an area for the gas to bind to

if it can be “activated”. During this process the material is heated to remove guests present from the synthesis process. Care must be taken during this process as incomplete removal of the guest molecules can result in lower than expected storage capacities.⁹ The removal of guest molecules can sometimes result in the breakdown of the framework whilst others produce interesting effects such as the structures of MIL (-53,-88)^{7,8} which have been found to “breathe” on the removal of the guest resulting in potential gas storage capabilities.

7.2 Applications

Research groups have already found many useful applications for the storage and release of gases from different materials such as the storage of hydrogen^{9,10} and methane¹¹ for energy applications. Environmental applications of gas storage media focus on the reduction of green house gases and “acid rain” gases such as the removal of carbon dioxide and sulfur dioxide from the flue exhaust of power plants.¹² Research into medical applications is also being applied to metal organic frameworks with the storage of nitric oxide for drug delivery.¹³

7.2.1 Hydrogen

Hydrogen is one of most widely publicised areas of interest for gas storage with the U.S. department of energy (DOE) setting a target for hydrogen storage to 6 wt% by 2010 and 9 wt% by 2015.¹⁴ This has led to a great deal of research to store and release hydrogen gas but not in conventional cylinders. Some fields of research suggest that hydrogen storage would be most viable in a metal organic framework as they have a large surface area with adsorption capacities of 7.5 wt% and 6.7 wt%

obtained by Wong-Foy *et al*¹⁵ for MOF-177, IRMOF-20 at 77K between 70 and 80 bar respectively well within the DOE's stringent requirements. Although it is also noted that organic polymeric or gel systems may be a better route as they would be lighter and potentially cheaper with the removal of the need to use metal centres. BASF¹⁶ have shown that the large surface areas of metal organic frameworks can contain a greater amount of H₂ in comparison to an empty container. *Figure 7.1* highlights how Cu-EMOF can store twice as much hydrogen within its framework than a conventional container at 30 bar. It is often forgotten that in today's society we use gas storage every time we start our cars or fly in a plane. Hydrogen locked into the crude oil based fuel oils is done in a non-reversible way but it is done so in a highly efficient and dense medium which currently out performs any other hydrogen storage system.

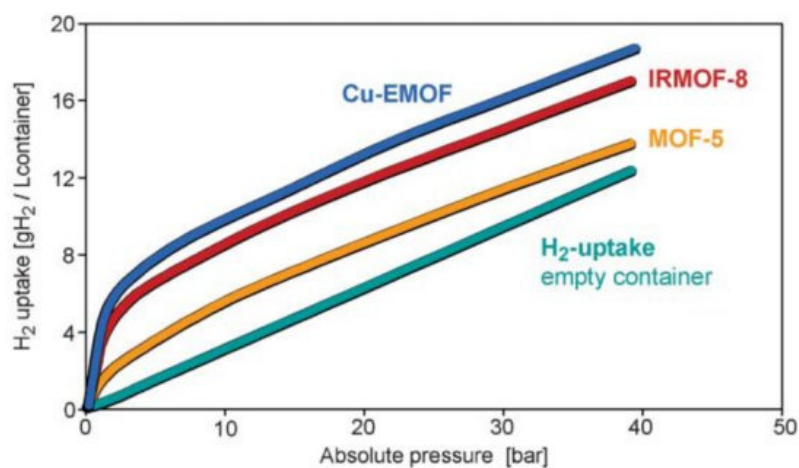


Figure 7.1: This graph highlights¹⁶ how the different MOFs (Cu-EMOF, IRMOF-8 and MOF-5) can contain more H₂ gas than a conventional gas bottle.

7.2.2 Carbon Dioxide

Carbon dioxide is a greenhouse gas and a significant contributor to global warming. There is a big push at the moment by companies to reduce their “carbon footprints”. This can be achieved in numerous ways the most obvious being in the reduction in gas omissions from factories, transport and power production. Another approach is to plant trees to offset the carbon dioxide produced by a company. With all these interesting and different ways of cutting down CO₂ emissions it is obvious to see why many research groups are investigating novel approaches to reducing the levels of this greenhouse gas.

Chemisorption is providing one way of capturing this unwanted gas such as with activated carbon¹ and within zeolites. However the best absorbers reported so far are from the metal organic frameworks MOF-177 and MIL-101 where 33.5 mmol g⁻¹ at 40 bar and 40 mmol g⁻¹ at 70 bar respectively.^{17,18} The aim of this approach would be to capture the gas and store it underground. Other proposals have included injection of the gas into deep saline aquifers and chemical fixation.^{19,20}

7.2.3 Sulfur Dioxide

Sulfur dioxide is a toxic gas and is usually given off as a by-product in many industrial processes which can have drastic effects on the environment, the release of sulfur dioxide can lead to the production of acid rain as the gas is free to oxidise forming sulfuric acid. There have been some studies of sulfur dioxide adsorption and desorption in zeolites²¹. Work by Cross *et al*²² have shown that it is possible to reversibly adsorb SO₂ in the molecular materials given the colloquial name of “Chinese” lantern complexes [XMn(μ-dppO₂)₄MnX]²⁺2X⁻.4MeOH.Me₂CO [X= Cl,

Br, I, SCN: dppO₂ = 1,3-bis(diphenylphosphinoyl)propane] with the gas proposed to be binding via the halide. Many different conformations of SO₂ binding have been reported²³ and as such there have been studies to investigate the most likely, such as work done by Nasluzov *et al*²⁴ where they tried to calculate likely sites for the sulphur dioxide to attach itself to zeolite HY however they were not able to locate the site exactly. Most of the work carried out for SO₂ storage has focused on converting the SO₂ into sulfates such as work by Dathe *et al*²⁵ where barium impregnated HKUST-1 was examined in an oxidative atmosphere whereby the SO₂ was adsorbed irreversibly as sulfates.

7.2.4 Nitric Oxide

Nitric oxide, once known as just a toxic gas, has been found to be an extremely important biological signalling molecule for vasodilatation, the prevention of platelet aggregation and wound repair.^{26,27} With such a wide range of uses it is important to be able to deliver the gas in a controlled way, as too much nitric oxide can lead to excess bleeding, septic shock, hypotension, eventually leading to death. Zeolites and MOFs have been looked at to be possible delivery systems to administer the gas in a controlled way with zeolites having a deliverable capacity of 1mmol NO per g of zeolite,²⁸ whilst those of MOFs having a capacity of ~7 mmol of NO/g of material.²⁹ With these interesting applications it is desirable to understand how the gas molecules bind inside a framework, so that we may be able to improve the storage of the material or release the gases at varying rates. McKinlay *et al*²⁹ showed that it is possible to use powder X-ray diffraction to examine a nitric oxide-loaded sample of CPO-27-Co (Co₂(dhtp)(H₂O)₂·8H₂O) an exceptionally good MOF at adsorbing,

storing and delivering nitric oxide. Other *in-situ* gas work has been carried out by Cruz *et al*³⁰ who were able to use single crystal data to locate nitric oxide in the cobalt exchanged zeolite-A.

7.2.5 Hydrogen Sulphide

Hydrogen sulphide is corrosive, toxic and has an unpleasant aroma it is as with NO useful in mammalian biology and is important for vasodilatation in smooth muscle cells.³¹ Blackstone *et al* found that in the right quantities H₂S can induce a suspended animation like state in mice.³² When exposed to 80ppm H₂S the mice dropped their consumption of oxygen by 50% and the CO₂ output dropped by 60%, a prolonged exposure time led to a drop in their metabolic rate by 90% which was followed by a drop in critical body temperature to just 2°C over ambient temperature, after the experiment it was then possible to return the mice to the regular air and they returned back to their normal state.

These findings have led to much research being carried out for potential applications to prevent brain damage where a lower core temperature is achieved it is possible to induce hypothermia without the induction of a homeostatic response which can help protect against brain injury from strokes.³³ This induced hibernation has other benefits such as it has been shown that organs from hibernating animals are protected from injury associated with storing and transporting,³⁴ this could help improve the success rate in the transport of human organs.

There is unfortunately an unpleasant stench associated with H₂S and therefore one of the challenges would be to contain the material and release it to only the area that

needs treatment, one way of achieving this goal would be to contain the gas in a framework such as a MOF which could then release the gas at the appropriate time.

7.3 Aim

For all these emerging applications it is important to truly understand how the frameworks interact with gas molecules. How are they kept inside the framework? How can we release the gas at a desired rate? With these unanswered questions we need to be able to examine the frameworks in greater detail to understand how they interact with the gas molecules with a view of being able to improve the materials and tailor them for specific roles.

The aim of this chapter is to examine the highly crystalline metal organic framework CPO-27-Co ($\text{Co}_2(\text{dhtp})(\text{H}_2\text{O})_2 \cdot 8\text{H}_2\text{O}$) using a specially designed environmental cell to experimentally locate gas molecules of sulfur dioxide and nitric oxide by single crystal X-ray diffraction which have been physisorbed or chemisorbed into the framework and also to monitor how the levels of gas adsorption change under various gas mixtures. These two gases, although toxic, have the benefit of being reasonable practical to handle and have low liquifaction temperatures and pressures. Combine this with the increase X-ray scattering ability of sulfur over carbon then it allows SO_2 to be an ideal screening gas in X-ray work.

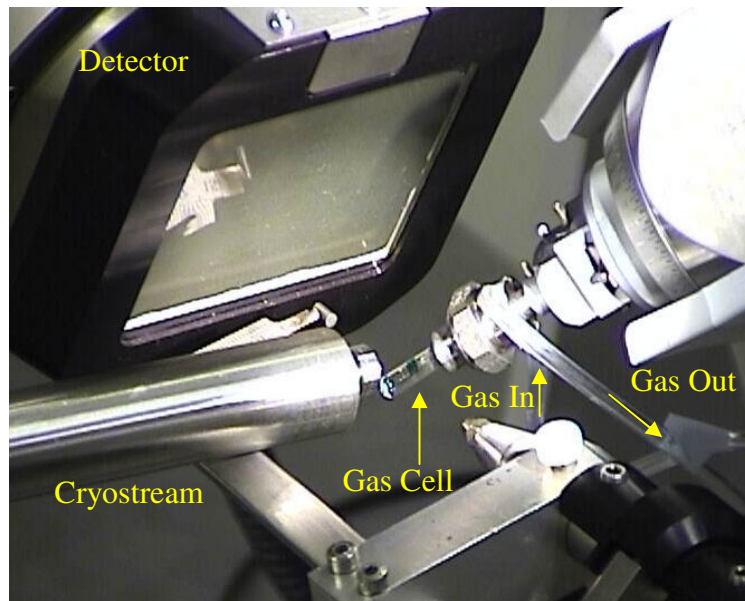


Figure 7.4: The environmental gas setup on the diffractometer at station 9.8 showing the gas entering and leaving the cell.

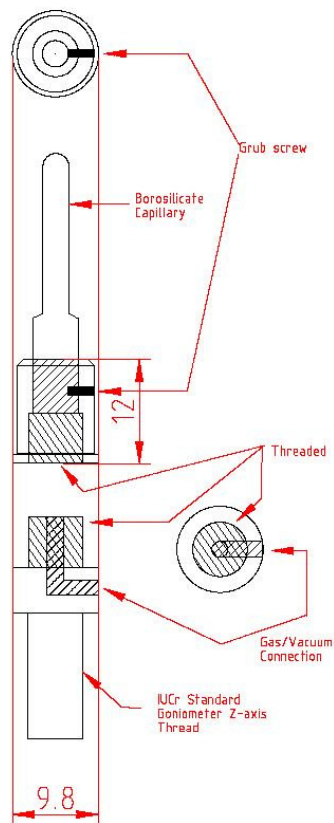


Figure 7.5: Schematic of the gas cell.

7.5 CPO-27-Co

The metal organic framework CPO-27-Co was first synthesised by Dietzel *et al* ³⁷ and has an average pore diameter of 11.08\AA^2 measured from the coordinated H_2O to H_2O . The cobalt is octahedrally coordinated by 6 oxygen atoms, 5 of the oxygen atoms are from the organic linker whilst the remainder is from water which is directed into the pore (*Figure 7.7*).

7.6 In-situ study of Sulfur dioxide

Sulfur dioxide was examined using the gas cell to investigate if it was possible to locate the gas within the CPO-27-Co framework for possible application in sulfur dioxide removal from industrial processes.

7.6.1 Experimental

The sample was “activated” by heating to 100°C under a dynamic vacuum until sufficient dehydration, monitored in real time by single crystal X-ray diffraction, had been achieved. Only partial dehydration was possible due to the fragility of the single crystal. The occupancy from the water oxygen was reduced to approx 60%, a longer dehydration was not possible due to time restrictions on the experiment. Once the water had been removed from the framework the sample was cooled to 10°C and the sulphur dioxide gas administered into the environmental cell alongside an inert carrier gas (N_2). Many datasets were collected with varying concentrations of SO_2 and N_2 (*Table 7.1*). When the SO_2 had been adsorbed into the framework there was a

colour change in the crystal from orange to black. Once it was established that the SO₂ was clearly visible in the framework the sample was purged with N₂ gas and heated under vacuum to assess the reversibility of the SO₂ adsorption.



Figure 7.6: There is a colour change after the crystal is exposed to SO₂ from orange to black

Table 7.1: showing the conditions applied to the crystal, the water content increases upon cooling due to residual water in the pores binding to the Co metal. The percentage gas are readings from the mass flow controller, with the maximum flow rates set to 90ml/min for N₂ and 124ml/min for SO₂.

Data Set	Conditions	Temp (°C)	R (%)	Water Oxygen Occupancy (%)	Chemisorption SO ₂ (%)	Physisorption SO ₂ (%)
1		100	5.59	14 (2)	0	0
2	25%SO ₂ 100% N ₂	10	8.44	81 (3)	26 (1)	72 (2)
3	25%SO ₂ 100% N ₂	10	9.21	73 (4)	33 (2)	73 (2)
4	25%SO ₂ 75%N ₂	10	8.25	73 (3)	32 (1)	70 (2)
5	45%SO ₂ 50%N ₂	10	9.04	68 (4)	37 (2)	76 (2)
6	25%SO ₂ 10%N ₂	10	9.18	66 (4)	36 (2)	74 (2)
7	25%SO ₂ 0%N ₂	10	9.19	75 (4)	30 (2)	73 (2)
8	25%SO ₂ 0%N ₂	10	9.42	69 (4)	32 (2)	73 (2)
9	100%N ₂	10	8.83	82 (3)	25 (1)	68 (2)
10	50%N ₂ and argon purge	10	9.06	74 (4)	30 (2)	69 (2)
11	Vacuum	10	9.58	80 (3)	24 (1)	65 (2)
12	Vacuum	10	7.99	80 (3)	24 (1)	66 (2)
13	Vacuum	10	8.56	87 (3)	18 (1)	63 (2)
14	Vacuum	100	8.34	36 (4)	18 (2)	59(1)
15	Vacuum	100	6.06	31 (2)	0	0

7.6.2 Results

Two sulphur dioxide sites have been located within the framework one physisorbed and one chemisorbed (*Figure 7.7*). The physisorbed site is clearly visible in the pore and the chemisorbed sulphur dioxide is attached to the cobalt metal via the oxygen from the SO₂.

A standard model was created for the refinement and the oxygen pointing into the pore was split between that of water and the oxygen atom from the SO₂. Free variables were applied to the 2 sulphur dioxide sites and the occupancies refined with the varying gas concentrations. All the framework atoms were refined anisotropically whilst the disordered SO₂ and water oxygen were kept isotropic, this was done as there was still considerable movement of the gas molecule within the framework due to the high temperature of 10°C to prevent SO₂ liquifaction within the cell.

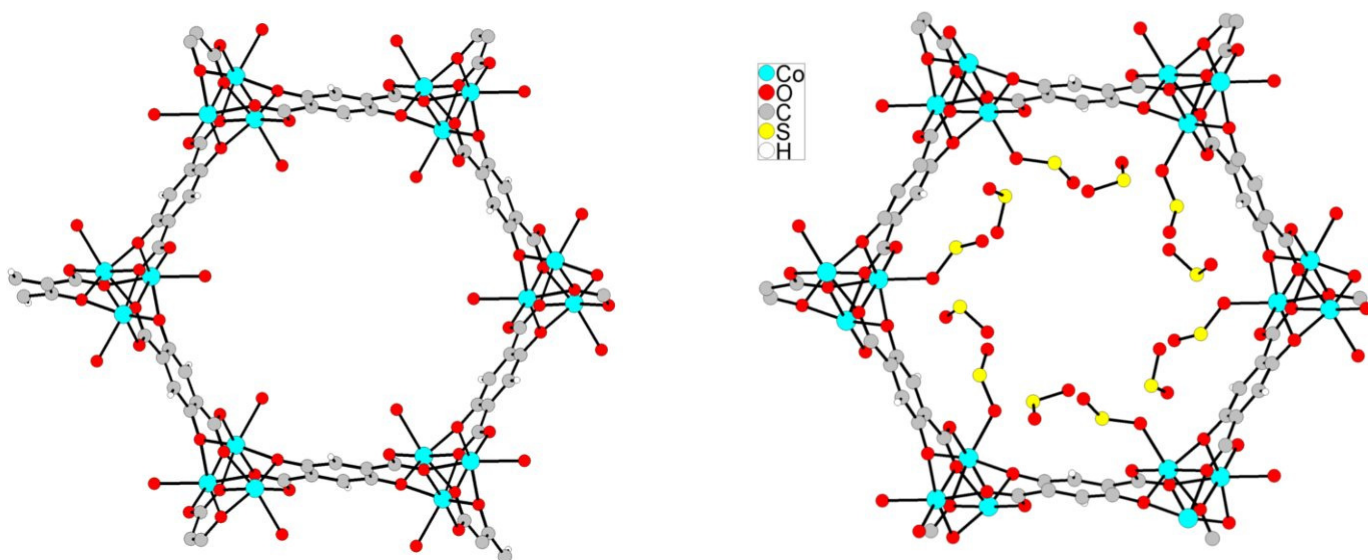


Figure 7.7 : The left hand channel is the partially dehydrated form of the Co MOF whilst the right hand is the MOF after being exposed to sulphur dioxide

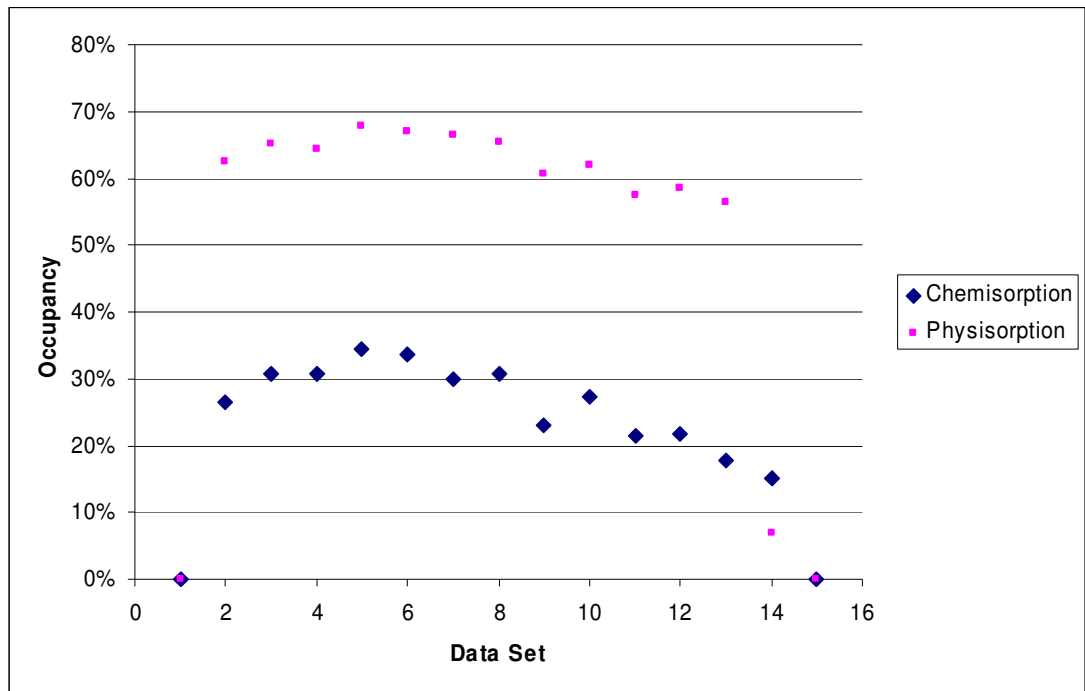


Figure 7.8: This graph shows the two sites which the SO_2 occupies, at point 14 it is clear to see the physisorbed SO_2 is lost much more rapidly than that of the chemisorbed site.

Figure 7.8 highlights that there is an increase in the levels of SO_2 which are chemisorbed onto the cobalt metal. The graph reaches a maximum at run 5. This corresponds with the highest concentration (45%) of SO_2 administered into the framework. As the pressure is lowered there is a slight decrease in occupancy.

Alongside the chemisorption on the cobalt metal, physisorption occurs within the pores of the framework of which a high concentration is achieved quickly. Once the framework appeared to be saturated the SO_2 was removed by purging with N_2 and heating the sample to 100°C . Figure 7.8 shows that the physisorbed and chemisorbed occupancies have a similar gradient however once the sample is heated to 100°C the physisorbed site loses the sulphur dioxide more readily than that of the chemisorbed site indicating that the chemisorbed SO_2 is more stable.

7.7 In-situ study of Nitric Oxide

Nitric oxide was examined using the gas cell to investigate if it was possible to locate the gas within the CPO-27-Co framework for possible use in medical applications.

7.7.1 Experimental

The sample was “activated” by heating to 90°C *in vacuo* until sufficient dehydration had been achieved. Only partial dehydration was possible due to time restrictions, the fragility of the single crystal in comparison to the large powdered sample and also the strength of the metal bonded water, a feature noted by Dietzel *et al*³⁸. After sufficient dehydration had occurred (approx 35% residual water) a mixture of nitric oxide and an inert gas (N₂) were administered into the cell until it was possible to locate the gas attached to the framework (*Figure 7.9*). The gas was then purged from the crystal under vacuum at 50°C to investigate the desorption process.

After initial solution and refinement of the NO loaded structure using the SHELX suite of programs,³⁹ a standard model was applied to all the datasets, framework atoms were refined anisotropically, with free variables applied to the occupancies of N and O bound to the Co site. Refined free variables were used to monitor the amount of NO adsorbing into the framework. One chemisorbed nitric oxide site was located. However, it was not possible to locate any physisorbed sites which is consistent with the expectation that NO will not strongly physisorb at this temperature. A residual oxygen atom was located within the pore and this has been labelled O1W and is probably due to residual water left within the environmental cell, now observable at the lower data collection temperature compared to the

dehydration experiment. The oxygen of the NO molecule is disordered over two positions in the model (O11A and O11B) and it was necessary to restrain the N-O distance to 1.47 Å obtained by the average of N-O bond lengths from the Cambridge structural database⁴⁰ (CSD) and that found in the NO loaded LTA structure.³⁰ The Co-O and Co-N distances were fixed with DFIX to 2.1 Å and 2.23 Å respectively (based on the hydrated CPO-27-Co MOF and the Cruz model³⁰). *Figure 7.10* shows the asymmetric unit from which it is clear to see the residual water attached to the metal site and the two O sites (O11A, O11B) of the nitric oxide. A residual Oxygen atom was located within the pore and this has been labelled O1W and is probably due to residual water left within the environmental framework.

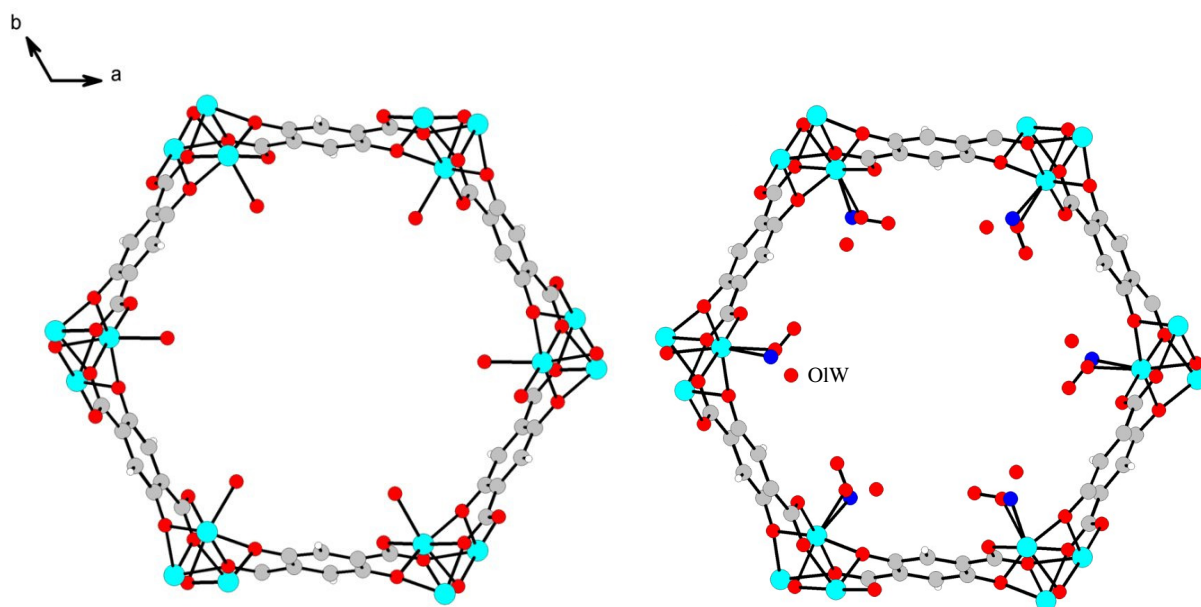


Figure 7.9: The left hand figure shows the pore at 50°C after the crystal had been dehydrated (35%), it was not possible to remove all the water from the framework. The right hand figure shows the pore after it had been exposed to nitric oxide, O11B has been removed for clarity.

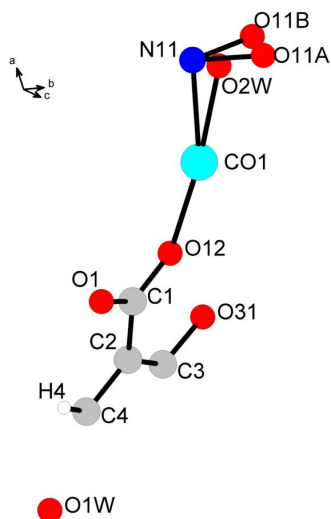


Figure 7.10: Asymmetric unit of CPO-27-Co with Nitric oxide attached

7.7.2 Results

Table 7.2: Conditions used for the experiment. The percentage gas are readings from the mass flow controller, with the maximum flow rates set to 90ml/min for N_2 and 133ml/min for NO

Data Set	Conditions	Temp (°C)	R (%)	Water occupancy (%)	Chemisorption NO Occupancy (%)	Free O Occupancy (%)
1	Vacuum	50	5.67	35 (1)	0	0
2	15% NO	50	4.92	39 (3)	11 (3)	0
3	15% NO	50	4.53	41 (4)	12 (4)	0
4	50%NO 50%N2	10	6.9	77 (4)	31 (3)	39 (3)
5	NO25% 25%N2	10	8.16	81 (4)	33 (4)	46 (3)
6	0%NO 100%N2	10	13.80	79 (6)	43 (5)	46 (4)
7	Vacuum	-50	13.01	74 (6)	35 (5)	58 (5)
8	Vacuum	25	10.44	80 (4)	39 (5)	51 (4)
9	Vacuum	25	6.58	86 (3)	17 (2)	59 (2)

Table 7.2 gives the conditions used during the experiment, from which it is clear that the increase of chemisorbed NO is related to the increase of NO administered into the gas cell. There is also an increase in water content which can be attributed to the fact that not all the water had been removed from the framework and once the crystal is cooled the water binds readily to the activated metal site.

The free O has been tentatively assigned as an oxygen atom of water as it was not possible to locate a diatomic NO molecule and it is extremely difficult to distinguish nitrogen (atomic number 7) from oxygen (atomic number 8) on the basis of their scattering factors at this wavelength. It is possible that this site is in fact mainly nitric oxide with a highly disordered oxygen atom attached to the central nitrogen, but we cannot be sure in this experiment.

Figure 7.11 shows the increase in nitric oxide content with run number and reaches a maximum at approx 43% occupancy, once the crystal is heated and a vacuum applied it is possible to see the NO content decreasing indicating the NO can be reversibly removed from the framework.

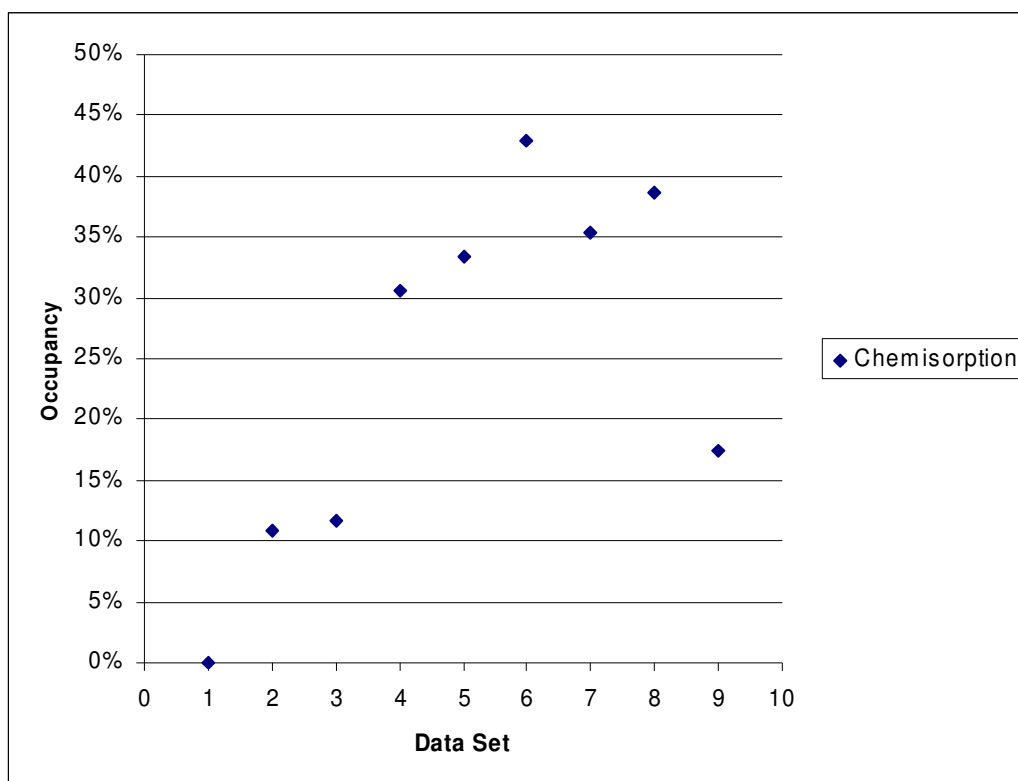


Figure 7.11: This graph indicates that there is an increase in chemisorbed NO as the concentration increases, when a vacuum is applied the occupancy is greatly reduced demonstrating the reversibility of the material.

7.8 Conclusions

This section has shown that it is possible to locate stored nitric oxide and sulfur dioxide within the metal organic framework CPO-27-Co using single crystal X-ray diffraction. It was possible to utilise the environmental gas cell to locate both the chemisorbed and physisorbed sites of sulfur dioxide, the sample was then heated which resulted in the loss of both these sites with the physisorbed site being lost more readily indicating that the chemisorbed SO₂ is more stable.

It was also possible to locate the chemisorbed site from the nitric oxide using the gas cell, unfortunately it was not possible to locate the physisorbed sites due to disorder in the pore from the relatively high temperature used to collect the data but also from the lower scattering factor from the nitrogen and oxygen atoms in comparison to the sulfur provided in SO₂. This model does however help to support and improve the model proposed by McKinlay *et al*²⁹ which was based on powder X-ray diffraction data.

There was a problem with both framework systems in activating the structure, as once the MOF was dehydrated and the temperature lowered the water site occupancy increased. This can be attributed to the residual water molecules remaining within the pores and as the crystal was fixed to the glass fibre with epoxy resin one side of the crystal could not allow any residual components to leave the framework preventing the complete loss of the water. A longer dehydration period may solve this problem. However, as already discussed we were restricted by the time available on the synchrotron station.

The environmental cell is a great addition to a SMX laboratory as it provides a way to examine reactions *in-situ*, similar to those shown by Bradshaw *et al*⁴¹ who managed to examine the MOF [Co₂(bipy)₃(SO₄)₂(H₂O)](bipy)(CH₃OH) at various temperatures to witness a reversible substitution reaction between the guests in the pores and the Co metal site.

It should also be noted that any gas could be selected in the environmental cell. In the future it would be really exciting to try and use the cell to examine deuterium storage using a neutron source to model hydrogen storage systems, expanding on the work by Yildirim and Hartman.⁴² Who examined MOF-5 using a neutron source and first-principles calculations to locate five types of Deuterium sites and demonstrated that it could contain up to 11 wt% storage at low temperature.

7.9 References

- ¹ F. Rodríguez-Reinoso, Y. Nakagawa, J. Silverstre-Albero, J.M. Juárez-Galán and M. Molina- Sabio, *Microporous and Mesoporous Materials*, 2008, **115**, 603-608
- ² M. J. Prauchner and F. Rodríguez-Reinoso, *Microporous and Mesoporous Materials*, 2008, **109**, 581-584
- ³ J. Ma, Z. Liu, Q. Liu, S. Guo, Z. Huang and Y. Xiao, *Fuel Processing Technology.*, 2008, **89**, 242-248
- ⁴ J. Pasel, P. Käßner, B. Montanari, M. Gazzano, A. Vaccari, W. Makowski, T. Lijewski, R. Dziembaj and H. Papp, *Applied Catalysis B: Environmental.*, 1998, **18**, 199-213
- ⁵ G. Férey, C. Mellot-Draznieks, C. Serre, F. Millange, J. Dutour, S. Surble, and I. Margiolaki, *Science.*, 2005, **309**, 2040-2042
- ⁶ H.K. Chae, D.Y. Siberio-Prez, J. Kim, Y. Go, M. Eddaoudi, A.J. Matzger, M. O'Keeffe, and O.M. Yaghi, *Nature*, 2004, **427**, 523-527
- ⁷ C. Serre, C. Mellot-Draznieks, S. Surblé, N. Audebrand, Y. Filinchuk and G. Férey, *Science*, 2007, **315**, 18281-1831
- ⁸ T. Loiseau, C. Serre, C. Huguenard, G. Fink, F. Taulelle, M. Henry, T. Bataille and G. Férey, *Chem. Eur. J.*, 2004, **10**, 1373-1382
- ⁹ B. Xiao, P. S. Wheatley, X. Zhao, A. J. Fleycher, S. Fox, A. G. Rossi, I.L. Megason, S. Bordiga, L. Regli, K. M. Thomas, and R.E. Morris, *J. Am. Chem. Soc.*, 2007, **129**, 1203-1209
- ¹⁰ D. J. Collins and H. Zhou, *J. Mater. Chem.*, 2007, **17**, 3154-3160
- ¹¹ M. Eddaoudi, J. Kim, N. Rosi, D. Vodak, J. Watcher, M. O'Keefe, and O.M. Yaghi, *Science.*, 2002 **295**, 469.

- ¹² A. R. Millward and O.M. Yaghi, *J. Am. Chem. Soc.*, 2005, **127**, 17998-17999
- ¹³ P.S. Wheatley, A.R. Butler, M.S. Crane, A.G. Rossi, I.L. Megson and R.E. Morris, *Molecular sieves: from basic research to industrial applications, pts a and b studies in surface science and catalysis*, 2005, **158**, 2033-2040
- ¹⁴ <http://www1.eere.energy.gov/hydrogenandfuelcells/mypp/pdfs/storage.pdf>
- ¹⁵ A. G. Wong-Foy, A.J. Matzger and O. M. Yaghi, *J. Am. Chem. Soc.*, 2006, **128**, 3494-3495
- ¹⁶ U. Mueller, M. Schubert, F. Teich, H. Puetter, K. Schierle-Arndt and J. Pastré, *J. Mater. Chem.*, 2006, **16**, 626-636
- ¹⁷ A. R. Millward and O. M. Yaghi, *J. Am. Chem. Soc.*, 2005, **127**, 17998-17999
- ¹⁸ P. L. Llewellyn, S. Bourrelly, C. Serre, A. Vimont, M. Daturi, L. Hammon, G. D. Weireld, J. Chang, D. Hong, Y. K. Hwang, S. H. Jung and G. Férey, *Langmuir.*, 2008, **24**, 7245-7250
- ¹⁹ J.M. Nordbotten, M.A. Celia and S. Bachu, *Transport in Porous Media*, 2005, **58**, 339-360
- ²⁰ F.S. Pereira, E. R. deAzevedo, E F. da Silva, T. José Bonagamba, D. L. da Silva Agostíni, A. Magalhães, A. E. Job and E. R. P. González, *Tetrahedron.*, 2008, **64**, 10097-10106
- ²¹ Y. Sakurai, Y. Takahashi, and T Makino, *Journal of Geochemical Exploration.*, 1998, **64**, 315-319
- ²² W.I. Cross, S.M. Godfrey, C. A. McAuliffe and R. G. Pritchard, *Chem. Commun.*, 2001, 1764-1765
- ²³ R.R. Ryan, G.J. Kubas, D.C. Moody, and P.G. Eller, *Struct. Bonding (Berlin)*, 46, (1981), 47

- ²⁴ V. A. Nasluzov, A.M. Shir, F. Nörtemann, M. Staufer, I V. Yudanov, N. Rösch, *Journal of Molecular Structure (theochem)*., 1999, **466**, 235-244
- ²⁵ H. Dathe, E. Peringer, V. Roberts, A. Jentys and J.A. Lercher, *C.R. Chimie.*, 2005, **8**, 753-763
- ²⁶ P.S. Wheatley, A.R. Butler, M.S. Crane, S. Fox, B. Xiao, A.G. Rossi, I.L. Megson, and R.E. Morris, *J. Am. Chem. Soc.*, 2006, **128**, 502-509
- ²⁷ M.R. Miller and I.L. Megson, *Br. J. Pharmacol.*, 2007, **31**, 624-631
- ²⁸ R.E. Morris and P.S. Wheatley, *Angew.Chem.Int.Ed.*, 2008, **47**, 4966-4981.
- ²⁹ A.C. Mckinlay, B. Xiao, D.S. Wragg, P.S. Wheatley, I.L. Megson and R. E. Morris, *J. Am. Chem. Soc.*, 2008, **130**, 10440-10444
- ³⁰ W.V Cruz, P.C.W. Leung and K. Seff, *Inorg. Chem.*, 1979, **18**, 1692-1696
- ³¹ C. Szabó, *Nature Review Drug Discovery.*, 2007, **6**, 917
- ³² E. Blackstone, M. Morrison and M. B. Roth, *Science*, 2005, **308**, 519
- ³³ H. Zhao, T. Shimohata, J. Wang, G. Sun, D. Schaal, R. Sapolsky and G. Steinberg, *J. Neurosci.*, 2005, **25**, 9794-9806
- ³⁴ S.L. Lindell, *Am. J. Physiol. Gastrointest. Liver. Physiol.*, 2005, 288, G473-G480
- ³⁵ R.J. Cernik, W. Clegg, C.R.A Catlow, G. Bushnell-Wye, J.V. Flaherty, G.N. Greaves, I. Burrows, D.J. Taylor, S.J. Teat, M. Hamichi, *J. Synchrotron Radiat.*, 1997, **4** 279.
- ³⁶ W. Clegg, M.R.J. Elsegood, S.J. Teat, C. Redshaw, V.C. Gibson, *J.Chem.Soc., Dalton Trans.* 1998, 3037.
- ³⁷ P.D.C. Dietzel, Y. Morita, R. Blom and H. Fjellvåg, *Angew. Chem. Int. Ed.*, 2005,**44**, 6354-6358

- ³⁸ P.D.C. Dietzel, R.E. Johnsen, R. Blom, and H. Fjellvåg, *Chem.Eur.J.*, 2008, **14**, 2389-2397
- ³⁹ G.M. Sheldrick, *Acta Cryst A.*, 2008, **64**,112-122
- ⁴⁰ <http://www.ccdc.cam.ac.uk>
- ⁴¹ D. Bradshaw, J.E. Warren, and M.J. Rosseinsky, *Science*, 2007, **315**, 977-980
- ⁴² T. Yildirim and M.R. Hartman, *Physi. Rev. Letters.*, 2005, **95**, 215504

8 *In-situ* comparison of ionothermal prepared zeolite under microwave and conventional heating

8.1 Introduction

This PhD has focused on probing porous materials further than is usual with X-ray diffraction, this is important to understand the fundamentals of the structure so that they could be tailored for specific tasks, however an important aspect that is sometimes overlooked is to understand the basic mechanism of zeolite synthesis.

As described previously in this thesis the ionothermally method is providing a great deal of interest in zeolites synthesis due to its low vapour pressure and reduction in the number of reagents. The reduction in vapour pressure is of particular interest as this opens up the possibility of microwave heating as there is no danger of the glass vials exploding.

Microwave heating is already providing some clear advantages over conventional methods, principally resulting in decreased synthesis¹ times. The ionic liquid (IL) solvent used in ionothermal synthesis is extremely susceptible to microwaves and Xu *et al* reported that the synthesis of aluminium phosphate molecular sieves by this method can be vastly accelerated by the use of microwave heating.² Lin *et al*³ have also shown that the metal organic frameworks of (EMIm)₂[Ni₃(TMA)₂(OAc)₂] and (EMIm)₂[Ni₃(TMA)₂(OAc)₂] can be synthesised with the use of microwave heating in 50 minutes compared to 3 days for conventional heating to result in purer phases and higher crystallinity. Not only does microwave heating result in faster crystallisation times it also helps to produce samples not readily made via

conventional methods. Jung *et al*⁴ showed that the structure $[\text{Ni}_{22}(\text{C}_5\text{H}_6\text{O}_4)_{20}(\text{OH})_4(\text{H}_2\text{O})_{10}].38\text{H}_2\text{O}$ was produced instead of the expected MIL-77 ($[\text{Ni}_{20}(\text{C}_5\text{H}_6\text{O}_4)_{20}(\text{H}_2\text{O})_8].40\text{H}_2\text{O}$) structure during microwave heating. This clearly shows how microwave assisted reactions can help to develop the materials on offer. The reduction in reagents is also a key benefit of ionothermal synthesis as this reduces the number of variables within the reaction which provides an ideal example to examine in-situ using Energy Dispersive X-ray diffraction (EDXRD) to get an understanding of the mechanism involved in the synthesis process.

EDXRD, consists of a “white beam” which contains all the X-ray wavelengths and is used to produce diffraction patterns, whereby reflection positions are differentiated by energy, they have been used in several studies of conventionally heated framework crystallisation to study the kinetics and pathway of reactions.^{5,6,7}

This technique ensures a large batch can be examined at high resolution, which means it is possible to observe the reaction and see any changes that occur. It has been shown that framework crystallisation rate is highly dependent on the size of the reaction vessel meaning that the kinetics determined from angle dispersive studies in capillaries will not be equivalent to those in normal autoclaves.^{8,9}

In some cases the high time resolution of EDXRD has allowed the discovery of intermediates in reactions which were subsequently isolated and fully characterised.^{10,11} Currently there are two examples of *in-situ* studies of zeolite crystallisation under microwave heating.^{12,13} Panzarella *et al* used a combined

SAXS/WAXS setup at NSL, Brookhaven with a custom waveguide capable of accepting 5 and 10mm NMR tubes as reaction vessels to study the hydrothermal crystallisation of several well known zeolite phases and compare the microwave kinetics with those of conventionally heated reactions.

8.2 Aim

The aim of this chapter is to investigate how microwave heating is different from conventional heating in the synthesis of the microporous aluminium phosphate SIZ-4¹⁴ *in-situ* using the energy dispersive X-ray diffraction (EDXRD) beamline at the SRS Daresbury (station 16.4).

8.3 Experimental

EDXRD data were collected on station 16.4 of the Synchrotron Radiation Source, Daresbury, UK. The basic experimental setup consists of an unmonochromated X-ray beam focussed into the sample with the diffracted beam collected by a three element detector¹⁵ (*Figure 8. 1 (a)*) which are positioned in order to maximise the intensity of the main Bragg peaks in the diffraction pattern (in this case the 2θ position of the bottom detector was 1.435°). The conventional heating experiment utilised a heating block which was controlled by a standard Eurotherm unit. The general setup has been fully described elsewhere.¹⁶ Diffraction patterns were collected with an accumulation time of two minutes.

The microwave setup utilised a commercial microwave source (ASTEX AX2110, output power 20-1000W) to generate microwave radiation at 2.45 GHz. During data collection, the temperature is continuously monitored using a fibre-optic probe (Neoptix T1, resolution of 0.1 K) in intimate contact with the sample mixture. A PC is used to control the temperature by varying the microwave power sent to the sample based on the output of the fibre-optic probe. The microwave radiation is driven to the sample through a WR284 (WG10) waveguide operating in the fundamental TE_{10} mode. The waveguide also makes up the microwave cavity with a sliding short termination driven over a 12cm range by a remotely controlled linear actuator. The sample holder consists of a thick wall silica tube (transparent to both microwave and X-ray radiation) of 0.6 cm internal diameter held vertically in the centre of the waveguide. On either side of the sample two windows are cut out from the cavity walls; a small hole is located on the incident X-ray beam side and on the opposite wall, a larger aperture covered with thin aluminium foil (~10 microns), designed for the detector geometry, allows the passage on the scattered X-rays.

In early experimental runs with the microwave setup it was discovered that the microwave leakage from the cavity caused interference with the sensitive 3-element detector, to minimise the interaction extra microwave shielding (aluminium foil) was added around the cavity and detector assembly (*Figure 8. 1 (b)*). The X-ray beam of station 16.4 was powerful enough to penetrate the aluminium shielding with minimal loss of intensity.

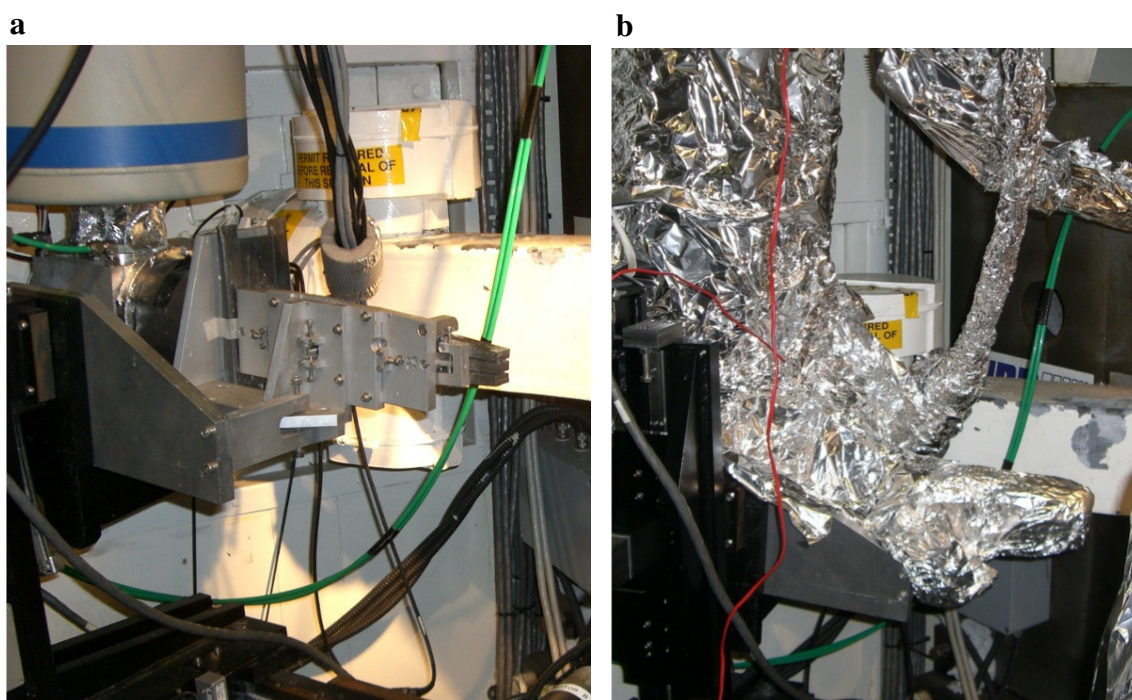


Figure 8. 1: The detector with out (a) and with microwave shielding (b).

Ionothermal synthesis seems ideal for *in-situ* studies as the ILs used develop almost zero pressure under reaction conditions enabling the reactions to be carried out in open vessels without sealing and with their dual role as structure directing agent and solvent less variables will affect the crystallisation process. In order to observe diffraction from the crystallising product it was necessary to increase the concentration of reactants above that normally used in ionothermal synthesis whilst remaining in the limits of the ionothermal regime (molar ratio of less than 1:1 water to IL) which resulted in some variation in peak intensity due to convection currents lifting crystalline material in and out of the beam (similar results were observed by Geselbracht and co workers¹⁷ when studying unstirred flux reactions using station 16.4). This is an experimental issue that will need to be solved in future work.

Microwave reactions were carried out in 8mm diameter glass test tubes with a fibre optic temperature probe lowered into the reaction mixture and the top sealed with a Teflon plug and tape. Conventionally heated reactions were contained in sealed 2-5ml size Biotage glass reaction vials. Aluminium isopropoxide (Aldrich) was mixed with phosphoric acid (85% weight solution in water, Aldrich) in the chosen reaction vessel and hydrofluoric acid (48% weight solution in water, Fischer) was dropped onto the mixture with a plastic pipette. 1-ethyl-3-methylimidazolium bromide (EMImBr) synthesised as described by Cooper *et al*¹⁴ was added, the container sealed and transferred either to the microwave cavity or the heater carousel and heated to 180°C. A ramp rate of 60°C per minute was used for the microwave heating and for the conventional experiments the heater block was set to that of 180°C before the reaction tube was inserted. The amounts of reagents used for microwave and conventional reactions are given in *Table 8.1* below.

Table 8.1: Reagents used for conventional and microwave heating experiments.

	Aluminium iso (g)	phosphoric acid (ml)	HF (ml)	EMImBr (g)
Conventional heating	0.4	0.68	0.06	9.5
Microwave heating	0.1	0.17	0.015	5.7

During the experiment small but significant X-ray burns were visible in the IL solvents after the reaction. The burns were visible as dark brown streaks (*Figure 8.2*) through the solidified IL on cooling of the reaction mixtures suggesting both that some of the solvent may have decomposed in the X-ray beam and that local heating may occur associated with the beam.



Figure 8.2: The reaction vessel used for both the conventional and microwave assisted heating experiments after the reaction has taken place, the dark brown spot is where the highly intense white beam entered the vessel causing localised heating.

8.4 Results and Discussion

8.4.1 Conventional Synthesis of SIZ-4

The *in-situ* EDXRD patterns for synthesis of SIZ-4 with conventional heating show strong peaks in the high d-spacing region covered by the bottom element of the 3 element detector (*Figure 8.3*). Some reflections are also visible later in the reaction on the middle element which can be unambiguously assigned to SIZ-4. The main features observed on the bottom detector begin to appear after about 80 minutes with a peak at 53.4 keV (d-spacing = 9.26Å) which can be attributed to the (0 2 0) reflection of SIZ-3. After approximately 3 hours a new peak at 54.6 keV (d-spacing 9.06Å) appears and begins growing in intensity. This peak corresponds to the (1 0 0) peak of SIZ-4. By the end of the experiment only the SIZ-4 (1 0 0) peak is present.

As the peak begins to grow in intensity there is an appearance of an extremely intense peak at an energy of 51.2 keV ($d = 9.66\text{\AA}$) which is present in three or four consecutive patterns (6 to 8 minutes of reaction time) then fades away again, reappearing from time to time in a similar short-lived manner. The d spacing of this peak corresponds to the most intense peak in the powder pattern of AlPO-CJ8¹⁸ a ladder like chain phase which is built from four ring units similar to those seen in SIZ-3 and 4.

The conversion of SIZ-3 to SIZ-4 has not previously been observed although transformation from AlPO₄₋₅ to SIZ-3 and subsequently to AlPO-25 has been observed by Wang and co workers in ionothermal synthesis with 1-butyl-3-methylimidazolium bromide and amine templates.¹⁹ The existence of this transformation explains some of the difficulties encountered in our attempts to influence production of either SIZ-3 or SIZ-4 from this system by manipulating the water content. Further *ex-situ* investigations of the reaction by quench cooling of reactions at various stages of heating has led to the isolation of a mixture of SIZ-3 and 4 at intermediate reaction times showing that the change from one phase to the other is quite slow. It has not been possible to isolate the intermediate phase and so therefore it cannot be unequivocally identified, however the template found in the structure of AlPO-CJ8 also directs the formation of the layered material AlPO-CJ12 when used in solvothermal synthesis without hydrofluoric acid and as a result it is reasonable to suggest that AlPO-CJ8 is the intermediate phase (there are no other materials with this d -spacing in the AlPO database²⁰).

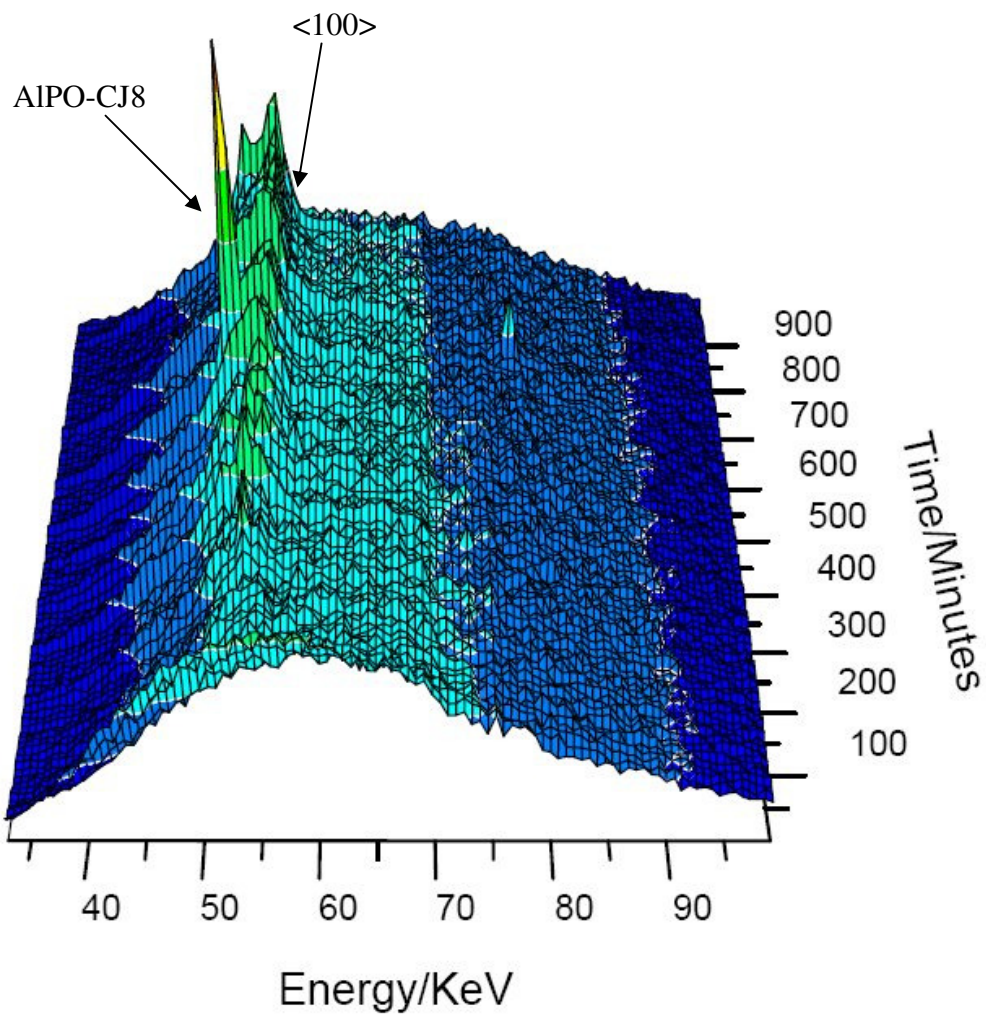


Figure 8.3: Graph showing the synthesis process from the bottom detector under conventional heating

8.4.2 Microwave Synthesis of SIZ-4

EDXRD shows that the microwave synthesis of SIZ-4 follows a significantly different route to that found with conventional heating. Even with a relatively slow heating ramp (compared to our lab microwave synthesis system) the induction time for crystallisation is reduced to only 30 Minutes. The main peaks are observed in the range of the bottom detector (*Figure 8.4*). The first feature to appear is the SIZ-4 (1 0 0) peak which remains the strongest feature until its intensity is constant and the reaction is complete. This result is similar to the results of Panazarella *et al* who have

shown that the selectivity of the synthesis of a mixture of sodium templated aluminosilicate zeolites A, X and sodalite is pushed towards the NaA and NaX under microwave heating. The change seems to be related to a more rapid onset of crystallisation.²¹

In the microwave data the weaker (1 1 0) peak is also observed in the EDXRD data suggesting superior crystallinity to the conventionally heated reaction. The intensity of the (1 0 0) peak is rather variable with several extremely intense peak levels occurring during the experiment, this can be attributed to convection currents moving crystalline material in and out of the beam as described in the experimental section above.

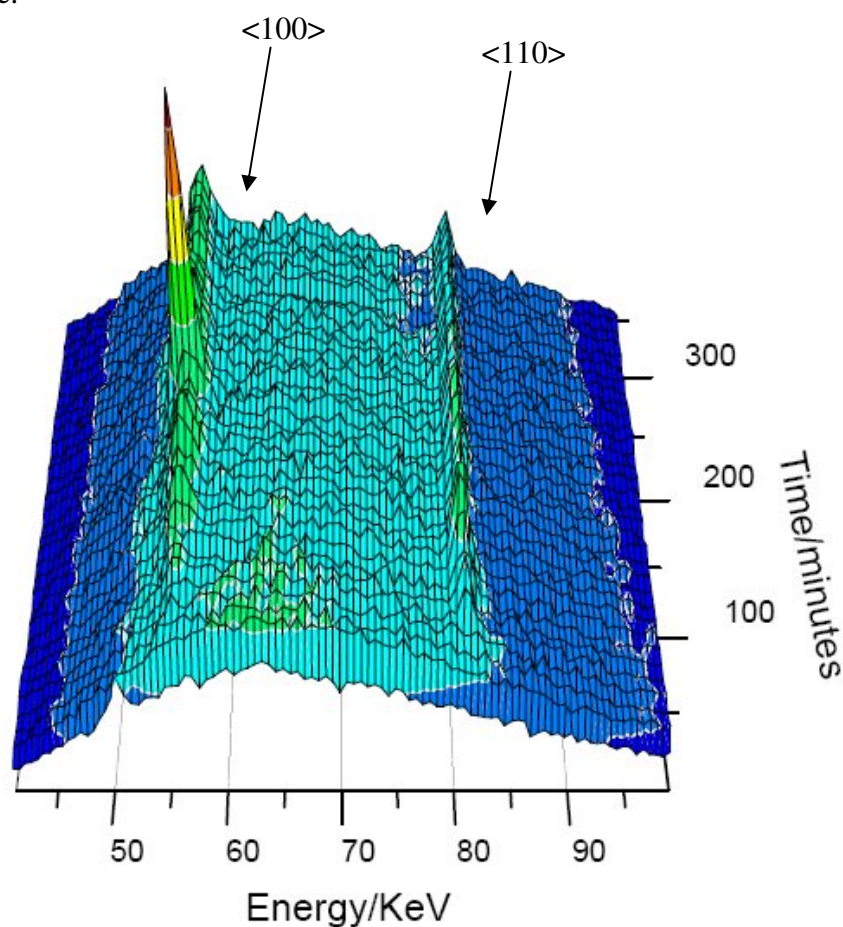


Figure 8.4: Graph showing the synthesis process from the bottom detector under microwave heating

8.5 Conclusions

This section has shown that it is possible to study ionothermally prepared materials *in-situ* using conventional and microwave assisted heating. The two processes have revealed significant differences between the mechanisms with conventional and microwave heating. The unexpected discovery that SIZ-3 can be converted to SIZ-4 during the synthesis of the latter helps to explain the prevalence of SIZ-4 in our study of the influence of water on the synthesis of the two phases.²² The discovery of the highly crystalline and short lived intermediate phase which appears as SIZ-3 is replaced by SIZ-4 as the dominant phase shows that the processes which take place in ionothermal synthesis can be extremely complex although SIZ-4 can be prepared in a single step with microwave heating. This may be due to the speed and consistency of microwave heating. The use of the microwave in this study has helped to confirm its importance in synthesis, as large quantities of material can be produced in a fraction of the time with greater crystallinity. The use of an ionic liquid has ensured that glass reaction vessels can be used throughout the experiment resulting in better resolution compared to a steel autoclave. With the huge growth of this type synthesis it is possible to produce many new structures suitable for this kind of study which will undoubtedly reveal more interesting features of this type of synthesis.

8.6 References

- ¹ G. A. Tompsett, W. C. Conner, and K. S. Yngvesson, *Chem Phys Chem*, 2006, **7**, 296-319.
- ² Y. Xu, Z. Tian, S. Wang, Y. Hu, L. Wang, B. Wang, Y. Ma, L. Hou, J. Yu, and L. Lin, *Angewandte Chemie*, 2006, **118**, 4069-4074.
- ³ Z. Lin, D. S. Wragg and R. E. Morris, *Chem. Commun.*, 2006, 2021-2023
- ⁴ S.H. Jung, J. Lee, P. M. Forster, G. Férey, A.K. Cheetham, and J. Chang, *Chem.Eur.J.*, 2006, **12**, 7899-7905
- ⁵ R. J. Francis and D. O'Hare, *J. Chem. Soc., Dalton Trans.*, 1998, 3133-3148;
- ⁶ R. I. Walton and D. O'Hare, *Chem. Commun.*, 2000, 2283-2291
- ⁷ D. O'Hare, J. S. Evans, R. J. Francis, P. Shiv Halasyamani, P. Norby, and J. Hanson, *Microporous and Mesoporous Materials*, 1998, **21**, 253-262.
- ⁸ P. Norby, *Current Opinion in Colloid & Interface Science*, 2006, **11**, 118-125
- ⁹ R. Grizzetti and G. Artioli, *Microporous and Mesoporous Materials*, 2002, **54**, 105-112.
- ¹⁰ R. Walton, T. Loiseau, D. O'Hare, and G. Férey, *Chem. Mater.*, 1999, **11**, 3201-3209
- ¹¹ F. Millange, R. Walton, N. Guillou, T. Loiseau, D. O'Hare, and G. Férey, *Chem. Mater.*, 2002, **14**, 4448-4459.
- ¹² B. Panzarella, G. Tompsett, W. C. Conner, and K. Jones, *ChemPhysChem*, 2007, **8**, 357-369.

- ¹³ G. A. Tompsett, B. A. Panzarella, W. C. Conner, S. Bennett, and K. W. Jones, *Nuclear Instruments and Methods in Physics Research Section B: Beam Interactions with Materials and Atoms*, 2007, **261**, 863-866.
- ¹⁴ E.R. Cooper, C.D. Andrews, P.S. Wheatley, P.B. Webb, P. Wormald, and R.E. Morris, *Nature*, 2004, **430**, 1012
- ¹⁵ G. Muncaster, A. T. Davies, G. Sankar, C. R. A. Catlow, J. M. Thomas, S. L. Colston, P. Barnes, R. I. Walton, and D. O'Hare, *Phys. Chem. Chem. Phys.*, 2000, **2**, 3523-3527.
- ¹⁶ S.M. Clark, R.J. Cernik, A. Grant, S. York, P.A. Atkinson, A. Gallagher, D.G. Stokes, S.R. Gregory, N. Harris, W. Smith, M. Hancock, M.C. Miller, K. Ackroyd, R. Farrow, R. Francis and D. O'Hare *Mater. Sci. Forum*, 1996, **228-231**, 213.
- ¹⁷ M. Geselbracht, L. Noailles, L. Ngo, J. Pikul, R. Walton, E. Cowell, F. Millange, and D. O'Hare, *Chem. Mater.*, 2004, **16**, 1153-1159.
- ¹⁸ W. Yan, J. Yu, Z. Shi, and R. Xu, *Inorg. Chem.*, 2001, **40**, 379-383.
- ¹⁹ L. Wang, Y. Xu, Y. Wei, J. Duan, A. Chen, B. Wang, H. Ma, Z. Tian, and L. Lin, *J. Am. Chem. Soc.*, 2006, **128**, 7432-7433.
- ²⁰ <http://mezeopor.jlu.edu.cn/alpo/>
- ²¹ G. A. Tompsett, B. A. Panzarella, W. C. Conner, S. Bennett, and K. W. Jones, *Nuclear Instruments and Methods in Physics Research Section B: Beam Interactions with Materials and Atoms*, 2007, **261**, 863-866.
- ²² D.S. Wragg, A.M.Z. Slawin and R.E. Morris, *Solid State Sci*, 2009, **11**, 411-416

9 Conclusions and Further Work

9.1 Conclusion

The main aims of this project were to get a better understanding of ionothermally prepared materials by investigating the materials which could be synthesised and also to probe materials further using different techniques such as an energy dispersive beamline, high resolution NMR techniques and a gas cell to investigate the storage capabilities of frameworks. The use of high resolution X-ray diffraction was also an important aspect to this work to look at the charge density of these systems in order to get a better understanding of their interactions within synthesis.

The collection of high resolution X-ray data from a synchrotron has shown that it is possible to get a high resolution data set from an ionic liquid and a metal organic framework, this was done in order to get a better understanding of these systems in the solid state. The NMR study in chapter 6 showed that conventional single crystal X-ray diffraction experiments, performed on a synchrotron source, provided suitable information for an improved understanding of the local structure in $\text{AlPO}_4\text{-15}$ whilst the high resolution data which had been refined with the multipole model from a lab source did not result in any more accurate data. Highlighting the fact that data obtained from a synchrotron provides highly accurate data in a fraction of the time compared to a standard lab source, thus providing a good starting model for NMR calculations and an excellent way to collect high resolution X-ray data.

The use of a synchrotron has been hotly debated as to its role in high resolution data collection, with Farrugia *et al*¹ suggesting that bad quality always results whilst work by Iversen *et al*² have shown that synchrotrons can be as good as conventional X-ray sources. This debate is difficult to resolve as there are so many variables that can affect the data. Only two systems have been discussed in this thesis, however many more data sets and systems had been analysed throughout this work and it was usually not until the data processing that the crystal was discovered to be of insufficient quality to continue with and as such had to be discarded, which highlights the difficulty in this technique. Unlike standard in-house X-ray sources which are pretty much uniform within departments that are performing high resolution data analysis, synchrotrons differ greatly, such as different diffractometers, varying intensities and different generation of light sources. Iversen and co-workers utilised a Huber four circle diffractometer and his data collections relied on phi scans whilst the work done on the SRS utilises a three circle diffractometer and has focused on omega runs as this was the only way to ensure plenty of redundancy to provide as accurate a model as possible. Beam decay is another variable which affects the quality of data achieved, if a high resolution data set was collected on the third generation synchrotron in Berkley (ALS) it experiences a loss in current of 310mA over a 6 hour period whilst at the SRS there is a drop of just 70mA over an 11 hour period as the data collections take along time to collect this beam decay will have a major effect on the data.

Chapter 5.1.3 highlighted some of the other problems which can arise from high resolution data sets which are mainly due to the very low temperatures at which data

was collected showing that it can be difficult to collect high angle data under normal conditions, however one of the advantages of Station 9.8 is the fact that different wavelengths can be selected whereby a smaller wavelength is chosen preventing the need for a 2θ collection close to 90° . It should also be noted that the n-Helix used for achieving such cool temperature consists of a beryllium nose cone which shrouds the crystal, although transparent to X-rays this shroud can still have a slight effect on the data. Even with the many problems which can be associated with this kind of study the results presented in this thesis are very encouraging and agree with Iversen *et al* in that it is possible to get good datasets from synchrotrons. This work has shown that it is possible to model a good high resolution dataset on an ionic liquid and also a good preliminary model of a metal organic framework. As the NMR study showed, a synchrotron can provide very accurate datasets and therefore have an important role to play in high resolution data collections in obtaining the best quality data.

This thesis has involved synthesising ionothermally prepared materials as described by Cooper *et al*³ with a view to examining at high resolution but also to develop the technique further to produce many novel structures in the form of metal phosphonates some of which have been published⁴. The ionothermal method has led to the synthesis of modular, chained and layered materials however it has also resulted in some interesting findings such as the discovery that the ionic liquid can break down under certain conditions and be incorporated into the structure $(\text{Al}_5\text{F}((\text{C}_4\text{H}_9)\text{PO}_3)_6(\text{OH})_2(\text{C}_8\text{N}_4\text{H}_6)_2$ and $\text{Ga}_6(\text{C}_4\text{N}_2\text{H}_6)_4\text{F}_2(\text{O}_3\text{PCH}_3)_8(\text{H}_2\text{O})_{0.4}$, providing another avenue for delivering functionality to materials. This work clearly shows that the ionothermal method can be adapted for many different kinds of

synthetic processes which we know today and as such could provide many more exciting structures.

One of the key features of ionothermal synthesis is that there is a negligible vapour pressure which has enabled the use of glass vessels to investigate the crystallisation process of SIZ-4 using a high energy dispersive beamline. The findings showed that SIZ-3 can be converted to SIZ-4 during the synthesis process, a feature not previously known and also confirmed that microwave heating can produce better quality crystals in a fraction of the time which is consistent with work done by Lin *et al*.⁵ Not only does this work give us an insight in to the crystallisation of SIZ-4 it also demonstrates how ionothermal synthesis provides an important role in understanding why these types of materials form the way they do, so that hopefully we can be able to tailor them for specific tasks.

Gas storage is a very interesting topic at the moment and the environmental gas cell is a great addition to a small molecule crystallography laboratory to examine the storage capabilities of structures *in-situ*. During this work it was possible to use the gas cell to examine the adsorption and desorption of sulfur dioxide and nitric oxide within the metal organic framework CPO-27-Co ($\text{Co}_2(\text{dhtp})(\text{H}_2\text{O})_2 \cdot 8\text{H}_2\text{O}$) as synthesised by Dietzel *et al*.⁶ The work demonstrated that it was possible to not only see the gas attached to the metal site (chemisorbed) but also to see the gas physisorbed into the pore, this was most evident with the sulfur dioxide as it was possible to locate the heavy sulfur, however with the nitric oxide it was only possible to locate the chemisorbed site due to disorder with the physisorbed site. This

highlights how the cell can be used for a wide range of gases and process such as comparing competing gases for specific sites.

9.2 Further Work

The collection of charge density data sets as shown in this thesis are still very much in the early stages of development and further work should be carried out to push this technique as it will only really develop if more groups embrace the technique and share the knowledge between peers. The experiment does not have to be particularly time intensive, as it was possible to collect a data set of the ionic liquid (EMImBr) in just over 2 hours with the wavelength set to 0.3740\AA , admittedly this was done on the very last day of beam time as it is not a typical wavelength used on the station but it shows that soon it could become a routine experiment. Even with great data collections the results are only as good as the software used and as such collaborations with Birger and co-workers is being sort for development of their invariom model⁷ which helps to refine data of a poor or complicated nature.

These are all potential future developments however the best development would involve the synthesis of better quality of crystals and a more reliable screening process as many of the systems examined diffracted well but were not of sufficient quality for high resolution X-ray diffraction.

Other notable improvements could be in the future development of the gas cell, as one of the problems associated with the cell were time restriction on the apparatus and as the cell had to be used on the beamline no other experiments could be performed. A gas cell which could be used offline to dehydrate the sample would be

the next model as this would ensure the beamline could be used for other experiments but also ensure the materials could be dehydrated fully before they were subjected to gases.

As shown in chapter 8 ionothermally prepared materials can be synthesised quicker and more efficiency using microwave heating and with the development of lab microwaves especially with microwave such as the “Biotage Sixty”⁸ which is capable of loading up to 60 different samples under full automation will enable the synthetic chemist to improve the throughput and to understand the methodology further so that it can become more systematic. Further developments can involve the use of various phosphonates and also to investigate other systems using the high energy dispersive beamline for other systems such as the metal organic frameworks which are being produced using this methodology.^{9,10}

9.3 References

- ¹ L.J. Farrugia, P.R. Mallinson, and B. Stewart, *Acta Cryst B.*, 2003, **59**, 234-247
- ² B.B. Iversen, F.K. Larsen, A.A. Pinkerton, A. Martin, A. Darovsky and P.A Reynolds, *Acta Cryst B.*, 1999, **5**, 363-374.
- ³ E.R. Cooper, C.D. Andrews, P.S. Wheatley, P.B. Webb, P. Wormald and R.E. Morris, *Nature*, 2004, **430**, 1012
- ⁴ P.J. Byrne, D.S. Wragg, J.E. Warren and R. E. Morris, *Dalton Trans.*, 2009, DOI: 10.1039/b813731e
- ⁵ Z. Lin, D.S. Wragg and R.E. Morris, *Chem. Commun.*, 2006, 2021-2023
- ⁶ P.D.C. Dietzel, Y. Morita, R. Blom and H. Fjellvåg, *Angew. Chem. Int. Ed.* 2005,**44**, 6354-6358
- ⁷ B. Dittrich ,C.B. Hubschle, M. Messerschmidt, R. Kalinowski, D. Girnt and P. Luger, *Acta Cryst A.*, 2005, **61**, 314-320
- ⁸ <http://www.biotage.com/DynPage.aspx?id=22002>
- ⁹ L. Xu, E. Choi and Y. Kwon, *Inorg. Chem. Commun.*, 2008, **11**, 150-154
- ¹⁰ Z. Lin, Y. Li, A.M.Z. Slawin and R.E. Morris, *Dalton Trans.*, 2008, 3989-3994